Universidad del País Vasco
Euskal Herriko Unibertsitatea

Modeling linear and non-linear light-matter interactions: From classical to atomistic nanoplasmonics

by

Alejandro Varas

Supervisors:
Prof. Dr. Angel Rubio
Prof. Dr. Pablo García-González

A thesis submitted to the University of the Basque Country UPV/EHU
in partial fulfilment of the requirement for the degree of
Doctor of Philosophy
in
Physics of Nanostructures and Advanced Materials

Donostia - San Sebastián, Spain

June, 2017

Abstract

In the last years, nanoplasmonics has become an important research field in the realm of light-matter interactions due to the wide range of applications. Driven by the interaction of electromagnetic radiation on nanostructures, resonant excitations of the so-called surface plasmons at the frequencies of electronic excitations in matter, leads to an enhanced of the local electric field.

Motivated by this phenomenon, in this thesis, we have modeled different linear and nonlinear interaction processes between electromagnetic radiation and low-dimensional nanostructures to simulate particular physical phenomena based on nanoplasmonics. Depending on the length scale of the system to be modeled, we have used different techniques, ranging from classical to atomistic ab-initio methods.

Specifically, we have performed: (i) DDA and finite element method calculations to analyze the plasmonic behaviour of recently synthesized (by a collaborative research group) non-stoichiometric heavily-doped semiconductor nanocrystals (Cu2-xS, and WO3-x); (ii) fully atomistic ab-initio simulations on metal cluster dimers to analyze the anisotropy effects of the plasmonic response of this nanostructures, including the electric field enhancement and the photoinduced current, as well as the influence of a one-atom junction between the two atomic conformations; (iii) and finally, motivated by a collaboration with another experimental research group we have modeled laser ablation processes in low-dimensional nanostructures, driven by intense and ultrashort laser pulses (in the plasmon resonance regime). Through these simulations, we have analyzed if Coulomb Explosion or electrostatic ablation is the mechanism of material removal in the early stage of the gentle ablation regime.

Acknowledgements

First, I would like to express my special appreciation and thanks to my supervisor Angel Rubio. Angel, I am really indebted to you for the incredible opportunity you gave me receiving me in your research group to work with you. Thank you very much for all your encouragement, guidance, advice, support, and confidence, giving me always the freedom to choose the projects to work on, and making my work both productive, as well as very enjoyable.

I would also like to thank to my co-supervisor Pablo García González from the Universidad Autónoma de Madrid (UAM). Pablo, thank you for your endless patience teaching me as much as possible, for the hospitality at the UAM, and for all your visits to Donostia - San Sebastián in order to help me to get through each step of this work.

Angel and Pablo, none of the projects I have been working on during my PhD, including the writing of the thesis, would have been possible without your help.

Special thank goes to Cecilia Benguria. Cecilia, thank you for your all your help with the paper work, for the great working atmosphere, and for your friendship beyond the working hours.

I want to thank all my collegues of the Nano-Bio Spectroscopy Group for the amazing scientific environment.

Finally, I acknowledge funding from the European Projects "DYNamo (ERC-2010-AdG-267374)", and "Grupos Consolidados UPV/EHU del Gobierno Vasco (IT-578-13)".

Contents

List of Figures

List of Tables

List of Publications

Published:

[1] Xavier Andrade, David Strubbe, Umberto De Giovannini, Ask Hjorth Larsen, Micael J. T. Oliveira, Joseba Alberdi-Rodríguez, Alejandro Varas, Iris Theophilou, Nicole Helbig, Matthieu J. Verstraete, Lorenzo Stella, Fernando Nogueira, Alán Aspuru-Guzik, Alberto Castro, Miguel A. L. Marques, and Angel Rubio. "Real-space grids and the Octopus code as tools for the development of new simulation approaches for electronic systems" *Phys. Chem. Chem. Phys.* **2015**, *17*, 31371–31396.

[2] Alejandro Varas, Pablo García-González, F. J. García-Vidal, and Angel Rubio. "Anisotropy Effects on the Plasmonic Response of Nanoparticle Dimers" *J. Phys. Chem. Lett.* **2015**, *6*(10), 1891–1898.

[3] Alejandro Varas, Pablo García-González, Johannes Feist, F. J. García-Vidal, and Angel Rubio. "Quantum plasmonics: from jellium models to ab initio calculations" *Nanophotonics* **2016**, *5*(3), 409–426.

To be submitted:

[4] Alejandro Varas, Pablo García-González, Angel Rubio, and Pavel Polynkin. "TDDFT study on femtosecond laser ablation on finite 2D/3D systems"

[5] Alejandro Varas, Pablo García-González, Angel Rubio, and Davide Cozzoli. "Theoretical analysis of the optical properties of mixed samples of $Cu_{2-x}S$ nanocrystals"

[6] Alejandro Varas, Pablo García-González, Angel Rubio, and Davide Cozzoli. "Theoretical analysis of the optical properties of $WO_{3-\delta}$ hemitubes"

[7] Alejandro Varas, Pablo García-González, F. J. García-Vidal, and Angel Rubio. "Single atom induced effects on the plasmonic response of nanoparticle dimers"

Chapter 1

Introduction

Everything we know as ordinary matter is made up of atoms. Hence the capability to manipulate matter at the atomic and molecular level, to create nanodevices with new or improved properties and functions due to their small sizes is highly desirable. This is precisely the goal of the nanoscience and nanotechnology and the reason of their increasing attention in the last decades [1].

In this context, the nanophotonics understood as the interaction of light with matter at the nanoscale has become a topic of rapidly increasing scientific interest and technological relevance, engaging many disciplines [2]. Even more, light-matter interactions at the nanoscale define the linear and non-linear optical properties of metallic nanostructures and hence are fundamental to understand and to control nanoscale localization of light at length scales far below the diffraction limit in the form of *surface plasmon* (SP) excitations [3].

These SP excitations can take various forms, ranging from *surface plasmon polaritons*, freely propagating excitations of electron density waves along the surface of a conductor, to *localized surface plasmon resonances* (LSPR), localized resonant electron oscillations on metal nanoparticles [4]. The amplitude of these resonant oscillations can overcome the excitation amplitude by orders of magnitude, leading to a substantial enhancement of the electromagnetic field (EF) [5].

This fascinating phenomenon has motivated research and development of plasmonic nanoparticles tailored for a broad range of applications spanning from biomedicine to solar energy technology [6]. More specifically, between the different applications, it is possible to find cancer and photothermal therapy [7, 8], biological labels [9], biosensing [10–12], light-harvesting in photovoltaics [13–15], nanocatalysis [16], optical filters [17], enhanced optical transmission through subwavelength apertures [18], light guiding and manipulation at the nanoscale [19], different surface enhanced imaging techniques [20–23], and even computer science [24] among many others.

LSPRs typically arise in noble metals like gold and silver nanostructures. These materials present attractive and unique optical properties due to they LSPRs as they are stable under a wide range of conditions and have a high charge carrier density [25] resulting in enhanced and geometrically tunable absorption and scattering resonances.

However, LSPRs are not limited to these metallic nanostructures and can also be achieved in other materials like copper [26], aluminium [27], heavily doped semiconductors [28] and metal oxides [29–32], chalcogenides [33], and even in graphene [34].

An advantage of using heavily doped semiconductors for nanoplasmonics is that their free carrier concentrations can be dynamically controlled by adjusting certain parameters as doping, temperature, pressure, stoichiometry, and phase transitions. This ability to manipulate the free carrier concentration of these nanostructures, allows not only the engineering of LSPRs but also active control within working devices, providing additional means of tuning the optical properties not readily available in metals [30, 35, 36].

However, despite their stoichiometric and undoped structure, it has been recently shown that anisotropic copper sulfide (CuS) nanocrystals, selectively trapped in the covellite phase, can exhibit intense and size-tunable LSPR at near-infrared (NIR) wavelengths [37].

On the side of nonstoichiometric cooper chalcogenides nanocrystals ($Cu_{2-x}X$, with X = S, Se, Te), these are convenient model systems for assessing the emergence of LSPR due to self-doping, as cation deficiency can be adjusted not only by selecting crystal phase and composition in the preparation stage [29,30,38–41], but also by performing post-synthesis

red-ox and cation-exchange reactions [37].

Thus, control over the structure and the stoichiometry, provides a useful tool for achieving dynamic and even reversible LSPR tunability through manipulation of the free hole carrier density, something hard-to-reach in noble metal nanoparticles, in which LSPR response is permanently locked in once geometric parameters (size and shape) have been engineered. Nonstoichiometric $Cu_{2-x}X$ nanocrystals have already been proposed to be practically exploitable in several previousl mentioned applications like biomedical imaging, photothermal cancer therapy, energy conversion and storage, and sensing [28–30, 38, 42]. However, full realization of their technological potential is still in development stage, then a deep understanding of the detailed physical origin of LSPR on this structures is necessary to increase the flexibility with which LSPR may be deliberately manipulated by rational material design.

In this context, and motivated by recently synthesized mixed-phase nonstoichiometric copper chalcogenides nanocrystas $Cu_{2-x}S$ by a collaborating research group, in chapter 3, we have performed classical simulations, within the frame of the discrete dipole approximation (DDA), in order to model and analize theoretically the plasmonic character as well as the carrier density of these nanostructures by reproducing their experimental extinction spectra.

As stated before, LSPRs, can also be achieved in transition metal oxides (TMO) nanostructures [31]. In particular, TMOs nanocrystals are interesting candidates to host LSPRs because they exhibit fascinating properties arising from the unique character of the outer-d valence electrons [43]. Tungsten oxide nanocrystals are a system of particular interest for the study of tunable plasmon resonances in nanoparticles, as tungsten oxide is stable under a wide range of conditions and has a band gap of 2.6 eV, which is ideal for absorption of visible light.

In the case of $WO_{3-\delta}$, a variety of oxygen-deficient stoichiometries can be obtained, leading to some contradictory results, ranging from $WO_{2.72}$ ($W_{18}O_{49}$) nanowires which appear to be semiconducting on the basis of electrical transport and photoluminescence studies [44,

45], to $W0_{2.8}$ (W_5O_{14}) nanowires which appear to be metallic on the basis of XPS and electrical transport measurements [46]. It has been also recently shown that nanoscale $WO_{2.83}$ ($W_{24}O_{68}$) nanorods support strong LSPRs and that these LSPRs account for a strong absorption feature ranging from the red edge of the visible to the NIR region [36].

Considering the above, and with the extra motivation of recently synthesized nonstoichiometric $WO_{3-\delta}$ nanocrystals of hemitubular morphology by a collaborating research group, in chapter 4, we have performed classical and semiclassical calculations, within the frame of the DDA and finite element method with the aim of sheed light on the unique structural-optical properties, of these novel nanostructures, which experimentally show tunable NIR to mid-IR plasmon resonances, essentially dependent on their aspect ratio.

As mentioned above, the recent advances in the fabrication and characterization of nanodevices have opened the possibility of tailoring plasmonic modes and, as a consequence, the response of nanosystems to external radiation [47–49]. From these advancements, a number of applications have been realized and/or proposed over the last few years, including optoelectronic hybrid devices [50,51], optical nanoantennas [52], optical traps [53], nano-sensors [54–56], and broad-band light harvesting devices [57], among many others.

Many properties of these nanodevices can be well understood in terms of classical optics [4]. However, if one of the characteristic lengths of the system reaches the subnanometric scale, quantum effects emerge in the optical response [48,58], as has been observed over the last few years in a series of breakthrough experiments [59–63]. In this regime, the theoretical treatment of the electromagnetic response must include the inhomogeneities of valence-electron densities and of photoinduced currents between the constituents of the device. Although there are some recent theoretical attempts aimed at incorporating such effects into the realm of classical optics [64,65], in principle, the quantum behavior of both ground- state and light-induced densities should be explicitly treated to obtain reliable theoretical predictions.

A prototypical case is a system made up of two metallic nanoparticles with subnanometric separation. In this metallic nanodimer, the establishment of a photoinduced electric

current between the particles changes the plasmonic modes of the system [66–68]. The main trends [69, 70] can be explained by describing the nanoparticles with the spherical jellium model in which the atomic structure is neglected, and by evaluating the optical response using the quantum mechanical time-dependent density functional theory (TDDFT) [71–74]. The latter provides the necessary accuracy when describing both the inhomogeneity of the electron density and the inherent nonlocality of the electromagnetic response. Thus, the combination of the jellium model and the TDDFT-based quantum treatment of light-matter interactions defines what is now considered to be state of the art in theoretical nanoplasmonics. Consequently, this approach has been applied to analyze the tunable response properties of nanorods [75], plasmonic cavities formed by nanowires [76–79], nanomatryushkas [80], and more recently, the optical properties of doped semiconductor nanocrystals [81]. Furthermore, the predictions of the jellium/TDDFT method can also be used to assess [76, 78] the capabilities of sophisticated refinements of classical optics [64, 65, 82–90], whose range of applicabilities is certainly broader because the numerical implementation of fully quantum methods is limited to systems containing up to thousands of atoms.

The widespread use of the jellium model when analyzing simple sp systems can be easily justified on the basis of the collective character of the plasmonic response. Moreover, the dynamical screening due to d electrons in noble-metal nanostructures can be mimicked by a dielectric background with an appropriate dielectric function [91]. Then, the atomic structure can be safely neglected in nanostructures made up of weakly interacting compact elements. However, this is not a valid approximation in systems like hybrid nanoclusters [92], where the chemical composition of the nanoparticle is essential to understanding its optical properties. As mentioned previously, the electromagnetic response of a nanodimer is greatly affected by the induced current between the particles. Therefore, in chapter 6, by using *atomistic* TDDFT we study how the relative orientation of theese nanodimers, leading to different atomic arrangements around the dimer junction, have to be taken into account to quantify the actual role played by the anisotropy of the atomic structure in the establishment of induced photocurrents and to determine those regimes

in which its description is relevant.

Additionally, in chapter 7 we show how the influence of a one-atom junction between the two atomic cluster modify their absorption spectra, leading (or not) to the establishment of a photoinduced electric current between the particles. Even more, depending on the magnetic nature of the atom bridging the system, we studied the possibility of a spin-dependent contribution to the absorption spectra, and then to the optical properties of the dimer, which could have tremendous implications on the development of optoelectronic devices.

One of the most determinant ingredients in the recent advences in nanophotonics is the rapid development, and the increasing availability of intense and ultrashort laser systems over the last years, which has opened up a wide range of new applications in industry, material science, medicine, and even in the arts. One important physical effect in light-matter interaction driven by these intense and ultrashort laser pulses, is the capacity to couple large amounts of energy into the target on a femtosecond time scale, leading to a growing interest in material removal or laser ablation induced by intense and ultrashort lasers pulses, which can be used for the deposition of thin films, the creation of new materials, for micromachining, and even for picture restoration and cleaning [93, 94].

Regarding the time scales, femtosecond laser ablation has the important advantage in such applications compared with standard ablation using nanosecond pulses because there is little or no secondary effects like mechanical or thermal damage on the target being ablated, i.e., neither collateral damage due to shock waves, nor heat conduction/difussion are produced in the material. [94–102].

Along with the great interest in the material removal induced by intense femtosecond lasers pulses, several experimental and theoretical studies has been published on the topic, some of them including different analytical models wich fits reasonably well the experimental results of ultrashort laser ablation processes [103–107], and a thorough knowledge of the short-pulse laser interaction with the target material is being reached rapidly. However, many fundamental questions remain concerning the physical origin of the material removal

process by femtosecond laser irradiation [108].

On of this questions is what is the physical mechanism of ion removal from a surface illuminated by a femtosecond laser pulse in the so-called *gentle ablation* regime. Some authors argue that the electrons that are removed from the material by the laser pulse, pull ions from the surface. That is called *e*lectrostatic ablation [104, 105, 109]. However there are even more studies stating that electrons quickly fly away, and the ions are pushed out of the material by the excessive leftover positive charge [110–119] . That is the Coulomb explosion (CE) mechanism. Then in chapter 5 we present some results based on simulations of laser ablation processes of low-dimensional structures, with the goal of sheed light on the controversy about the mechanism of ablation in the genle ablation regime.

Last but not least, all the basics corresponding to the theoretical background and the comptutational details necessary to develop the work of this thesis is presented in chapter 2. Sumarizing, through the following chapters we have modeled different nanoplasmonic-related systems, going from classical to atomistic ab initio methods. In chapter8 we present the final conclusions of the work as well as the perspectives.

Chapter 2

Theoretical & Computational Background

2.1 Introduction

Localized surface plasmons (LSPs) are collective and non-propagating oscillations (excitations) of conduction electrons around the surface of a metallic object that arise as a result of a resonant coupling with an external incident electromagnetic (EM) field [4,20,120,121]. Such strong induced charge oscillations are driven by the force exerted by the (oscillating) incident field, whereas the restoring force depends very sensitively on electron-electron interactions and on the curvature of the surface, leading to the emergence of resonance modes (localized surface plasmon resonance), and consequently to a field amplification (enhancement) and concentration in subwavelength regions, both inside, as well as in the near-field region outside the object, which is the basis of plasmon-enhanced spectroscopies [54, 122].

In many cases of interest, the plasmonic properties of a nanostructure can be theoretically characterized just by solving the classical Maxwell's equations with appropriate boundary conditions. In these cases, the electromagnetic response of the nanostructure can be successfully described by a *local* permittivity $\epsilon(\omega)$. That point, together with the

conceptual simplicity of this *local-optics approximation,* in adition to the existence of a number of efficient numerical implementations [120, 123, 124] explains its widespread use in theoretical classical plasmonics.

For nanodevices where the separation between metallic constituents [125,126] and/or their radii of curvature is smaller than a few nanometers [127], the local-optics approximation breaks down and the intrinsic spatially *nonlocal* nature of the optical response has to be incorporated into the classical theory, either by using simplified hydrodynamic models [128, 129] or by defining space-dependent dielectric functions in the metal-dielectric interfaces [130]. Even if such a nonlocality is included in a very crude manner, many deficiencies of the standard local-optics approximation are remedied. However, the unrealistic sharp boundaries between a metallic object and the surrounding dielectric medium are still kept. That is, classical nonlocal optics neglect the inhomogeneity of the electron density at the surface of a metal (the so-called electron-density spill-out). As a consequence, features like size-dependent shifts of the main LSP of isolated small nanoparticles [91] are beyond the scope of classical nonlocal theories[1]

On the other hand, recent experiments on the optical properties of two metallic nanoparticles at subnanometric separation have pointed out a discrepancy from the predictions of both local- and nonlocal-optics [60–63, 131–133]. In this regime the optical response is affected by the overlap of electron densities of the two nanoparticles and by the establishment of a photoinduced tunnel current between them [65, 69, 70]. The latter can be treated, even in the realm of local optics, by including effective dielectric media in what are called *quantum-corrected* classical methods [65], but the lack of electron density spill-out is a drawback. For such systems, classical methods appear as inapplicable, which has contributed to the emergence of the field of quantum nanoplasmonics [58]. As a consequence, methods like time-dependent density functional theory (TDDFT) [71], hitherto restricted to condensed matter physics and quantum chemistry, are gaining more and more importance in the field of plasmonics.

[1] In many practical applications the above-mentioned, and other limitations are not relevant, so nonlocal optics can be consider as state of the art in classical plasmonics.

Then, this chapter is devoted to define the theoretical framework in which this work is based, and the computational tools used and implemented. It is divided in two main secctions, the first one is the correspondig to the classical approach, where we shall briefly describe the basis of scatterig theory in the framework of classical EM theory through the Maxwell equations and linear optics, being able to describe some idealized models (which will be done in Chapters X and Y to analize the absorption spectra of real samples). The second part of this chapter is about *ab-initio* methods, here we briefly present the theoretical foundations of TDDFT, and some of its capabilities, required to analyze, the optical absorption of simple model systems (which will be done in Chapters Z). Finally, we will briefly mention some implemented features in the Octopus code, in which the ab-initio calculations were performed (This features were used in Chapters Z and W).

2.2 Classical approach

Matter is composed of a large number of discrete elementary electric charges. If matter is illuminated by an oscillating EM field, their electric charges are excited and set into an oscillatory motion at the same frequency of electric field of the incidend wave. This oscillatory motion of the electric charges is an acccelerated motion, and accelerated charges radiate electromagnetic energy. This phenomenon is called *scattering* due to radiation is scattered by the electric charges, and in general, gives rise to light with a polarization state different from that of the incident beam[2]. Aditionally, the electric charges may transform part of the incident electromagnetic energy into other forms such as heat, a process called *absorption*.

However, even at the subnanometer lenght scale, the number of elementary charges forming a nanoparticle is extremely large, and solving the scattering problem directly, for each charge is impracticable. Fortunately, the same problem can be treated by using the concepts of macroscopic electromagnetics, which treat the large collection of charges

[2]Although the oscillatory motion of the electric charges is at the same frequency of electric field of the incidend wave, the scattered light could not have the same frequency as the incident light.

as a macroscopic body with a specific distribution of the refractive index. So, begin with the basic equations governing the electromagnetic response of matter, the so-called *macroscopic* Maxwell's equations.

2.2.1 Macroscopic Maxwell equations

Let us consider a target illuminated by an electromagnetic wave represented by the fields E_{inc} and H_{inc}. At the surface of the target the wave is partially refracted (E and H) and partially reflected (E_{sca}, H_{sca}). These fields E and H must satisfy the Maxwell's equations as well as the vector wave equation, thus we take as a starting point the Maxwell's equations for macroscopic electromagnetic fields, that describe the large-scale behaviour of matter without having to consider atomic scale details at interior points in matter, which in SI units may be written in the following form

$$\nabla \cdot D(r,t) = \rho_{ext}(r,t) \tag{2.1}$$

$$\nabla \times E(r,t) = -\frac{\partial}{\partial t} B(r,t) \tag{2.2}$$

$$\nabla \cdot B(r,t) = 0 \tag{2.3}$$

$$\nabla \times H(r,t) = \frac{\partial}{\partial t} D(r,t) + J_{ext}(r,t) \tag{2.4}$$

where $E(r,t)$ is the electric field, $D(r,t)$ is the electric displacement or electric flux density, $B(r,t)$ is the magnetic induction or magnetic flux density and $H(r,t)$ is the magnetic field. These equations connect the four mentioned fields with the external charge $\rho_{ext}(r,t)$ and current density $J_{ext}(r,t)$. The relationship between the flux density fields D and B with the electric and magnetic fields E and H are given by introducing the electric and magnetic polarization fields P and M,

$$D(r,t) = \varepsilon_0 E(r,t) + P(r,t) \ , \tag{2.5}$$

$$B(r,t) = \mu_0 H(r,t) + \mu_0 M(r,t) \ , \tag{2.6}$$

where ε_0 and μ_0 are the electric permittivity and the and magnetic permeability of free space respectively. Since we are dealing with nonmagnetic media, we do not need to consider the magnetic response represented by M, limiting our description to electric polarization effects. The electric polarization field P describes the electric dipole moment per unit volume inside the material, caused by the alignment of microscopic dipoles with the electric field. It is related to the *internal* charge density via $\nabla \cdot P = -\rho$. Charge conservation ($\nabla \cdot J = -\partial\rho/\partial t$) further requires that the *internal charge and current densities* are linked via[3]

$$J = \frac{\partial P}{\partial t} . \tag{2.7}$$

Inserting Eq. (2.5) into Eq. (2.1), leads to

$$\nabla \cdot E = \frac{\rho_{tot}}{\varepsilon_0} . \tag{2.8}$$

Now, assuming an homogeneous and isotropic medium and approximating its response to be linear, Eq. (2.5) and Eq. (2.6) can be written as

$$D = \varepsilon_0 \varepsilon E , \tag{2.9}$$

$$B = \mu_0 \mu H , \tag{2.10}$$

where ε is the dielectric constant or relative permittivity and $\mu = 1$ is the relative permittivity of the nonmgnetic medium. The linear relationship between D and E given by Eq. (2.9) is often also implicitly defined by using the macroscopic electric susceptibility

[3]We distinguish between external (ρ_{ext}, J_{ext}) and internal (ρ, J) charge and current densities, so that in total $\rho_{tot} = \rho_{ext} + \rho$ and $J_{tot} = J_{ext} + J$.

χ, which describes the linear relationship between P and E via[4]

$$P = \varepsilon_0 \chi E \, . \tag{2.11}$$

where $\varepsilon = 1 + \chi$ can be obtained inserting Eq. (2.5) and Eq. (2.11) into Eq. (2.9).

Finally, the internal current density J caused by the electric field E, can be defined via the conductivity σ by

$$J = \sigma E \, . \tag{2.12}$$

Now, for the sake of simplification we restrict the considerations to only harmonic waves, hence the time dependence of the fields can be separated with the ansatz

$$E = E(r) e^{-i\omega t} \, , \tag{2.13}$$

$$H = H(r) e^{-i\omega t} \, . \tag{2.14}$$

By using Eq. (2.13) and Eq. (2.14) in Eqs. (2.1) to (2.4) and assuming no static charges ($\rho = 0$) we obtain

$$\nabla \cdot (\varepsilon E) = 0 \tag{2.15}$$

$$\nabla \times E = i\omega \mu_0 H \tag{2.16}$$

$$\nabla \cdot B = 0 \tag{2.17}$$

$$\nabla \times H = (-i\varepsilon\varepsilon_0\omega + \sigma) E \tag{2.18}$$

Eq. (2.15) can be further simplified for isotropic and homogeneous matter, for which ε is

[4] In general, the fields P and E are not necessary parallel (anisotropic media) and can be described by a series expansion of P in powers of E (nonlinear media), where susceptibilities $\chi_{ijk\ldots}$ are introduced as constants in relation to E. Then, for each component $i = x, y, z$ of P

$$P_i = \varepsilon_0 \sum_j \chi_{ij} E_j + \varepsilon_0 \sum_j \sum_k \chi_{ijk} E_j E_k + \varepsilon_0 \sum_j \sum_k \sum_l \chi_{ijkl} E_j E_k E_l + \ldots$$

only a scalar, to

$$\nabla \cdot E \;=\; 0\;. \tag{2.19}$$

However, it is worth to note that this simplification is not always allowed. Nevertheless, an approximate solution for scattering by an anisotropic target can be obtained by taking the solution for each direction separately and averaging them accordingly[5]. In the following, we assume for simplicity homogeneous and isotropic materials, for which Eq. (2.19) holds.

For solving these Maxwell equations simultaneously for E and H, Eqs. (2.16) and (2.18) must be decoupled. This can be achieved by taking the curl of one equation and inserting the result into the other one, resulting in the vector wave equation or Helmholtz equation

$$\nabla^2 Z - k^2 Z \;=\; 0\;, \tag{2.20}$$

where Z represents either E or H fields, and the wavenumber k satisfies the dispersion relation

$$k^2 \;=\; \frac{\omega^2}{c^2}\left[\varepsilon(\omega) + i\frac{\sigma(\omega)}{\omega\varepsilon_0}\right]\;, \tag{2.21}$$

$$\;=\; \frac{\omega^2}{c^2} n^2(\omega)\;, \tag{2.22}$$

where $n(\omega) = n'(\omega) + in''(\omega)$ is the complex refractive index. The term in parentheses in Eq. (2.21) combines the permittivity ε (polarization) with the conductivity σ (absorption) to give the complex dielectric function $\varepsilon(\omega) = \varepsilon'(\omega) + i\varepsilon''(\omega)$. Eqs. (2.21) and (2.22) yields to

$$n(\omega) \;=\; \sqrt{\varepsilon(\omega)}\;. \tag{2.23}$$

[5]Se puede hacer referencia al capítulo de los hemitubos de Davide.

Therefore

$$\varepsilon' = n'^2 - n''^2 \,, \tag{2.24}$$

$$\varepsilon'' = 2n'n'' \,. \tag{2.25}$$

By solving Eqs. (2.24) and (2.25) for n' and n'' we obtain

$$n' = \sqrt{\frac{\sqrt{\varepsilon'^2 + \varepsilon''^2} + \varepsilon'}{2}} \,, \tag{2.26}$$

$$n'' = \sqrt{\frac{\sqrt{\varepsilon'^2 + \varepsilon''^2} - \varepsilon'}{2}} \,. \tag{2.27}$$

The term n'' is called the *extinction coefficient* and determines the optical absorption of electromagnetic waves propagating through the medium. It is linked to the absorption coefficient α of Beer's law (describing the exponential attenuation of the intensity of a beam propagating through the medium via $I(x) = I_0 e^{\alpha x}$) by the relation

$$\alpha(\omega) = \frac{2n''(\omega)\omega}{c} \,. \tag{2.28}$$

Consequently, the imaginary part ε'' of the complex dielectric function determines the amount of absorption inside the medium. For $|\varepsilon'| \gg |\varepsilon''|$, the real part n' of the refractive index n, quantifying the lowering of the phase velocity of the propagating waves due to polarization of the material, is mainly determined by ε'. Examination of Eq. (2.21) thus reveals that the real part of σ determines the amount of absorption, while the imaginary part contributes to ε' and therefore to the amount of polarization.

Finally, combining Eq. (2.2) with Eq. (2.4), and assuming no external stimuli, we obtain the wave equation

$$\nabla \times \nabla \times E = -\mu_0 \frac{\partial^2 D}{\partial t^2} \,, \tag{2.29}$$

By Fourier transforming Eq. (2.29) to frequency domain we obtain

$$\mathrm{K}(\mathrm{K}\cdot E) - K^2 E \;=\; -\varepsilon(\mathrm{K},\omega)\frac{\omega^2}{c^2}E\ . \tag{2.30}$$

being $c = 1/\sqrt{\varepsilon_0\mu_0}$ the speed of light in vacuum. For transverse waves, (K is perpendicular to E), $\mathrm{K}\cdot E = 0$, and the generic dispersion relation is obtained from Eq. (2.30)

$$K^2 E \;=\; -\varepsilon(\mathrm{K},\omega)\frac{\omega^2}{c^2}E\ . \tag{2.31}$$

But for longitudinal waves (K is parallel to E), Eq. (2.30) implies that $\varepsilon(\mathrm{K},\omega) = 0$, meaning that longitudinal collective oscillations can only occur at frequencies corresponding to zeros of $\varepsilon(\omega)$[6].

These kind of longitudinal charge oscillations are referred to as *plasmons* due to the fact, that they were first predicted and detected in plasmas [134].

The dielectric function $\varepsilon(\mathrm{K},\omega)$ describes the response of a system to an external electric perturbation. It is itself determined by the electronic properties of the material, such as intra- and interband transitions and collective excitations. In order to convey a rudimentary understanding of the optical and electrical properties described by ε, we will consider a few classical models: The Drude model, the Lorentz model, and the so-called Drude-Lorentz model which is a combination of both Drude and Lorentz models. The Drude model is useful for the understanding of free-electron gases, *i.e.* ideal metals. The Lorentz model incorporates single particle excitations, *e.g.* interband transitions, and can be used to study insulators and semiconductors, and can be regarded as an extension of the Drude model.

[6] With some considerations, we could reach the same result with a different approach by expressing the fields E and B in terms of a vector potential $A(r,t)$ and a scalar potential $\phi(r,t)$

2.2.1.1 The Free-electron Gas and The Drude Model

In the following, the dielectric function will be derived for the simple case of an ideal metal. In this case, the conduction electrons behave like free charged particles. In the context of this classical model, the equation of motion for the conduction electrons with mass m and charge $-e$ in a field E is given by

$$m\frac{\partial^2}{\partial t^2}u(t) + m\gamma\frac{\partial}{\partial t}u(t) \;=\; -eE(t)\;, \tag{2.32}$$

where γ represents the damping due to scattering in the electron gas and provides an energy-loss mechanism. Assuming an harmonic time dependence $E(t) = E_0 e^{-i\omega t}$ of the driving field, a particular solution of this equation describing the oscillation of the electron is $u(t) = u_0 e^{-i\omega t}$. The complex amplitude $u(t)$ incorporates any phase shifts between driving field and response via

$$u(t) \;=\; \frac{eE(t)}{m(\gamma^2\omega^2 + i\gamma\omega)}\;. \tag{2.33}$$

The displaced electrons contribute to the macroscopic polarization $P = -N\ e\ u(t)$, explicitly given by

$$P \;=\; -\frac{Ne^2E(t)}{m(\omega^2 + i\gamma\omega)}\;. \tag{2.34}$$

Using Eq. (2.34) in Eq. (2.9) yields to

$$D \;=\; \varepsilon_0\left(1 - \frac{\omega_p^2}{\omega^2 + i\gamma\omega}\right)E(t)\;, \tag{2.35}$$

where $\omega_p = \sqrt{Ne^2/\varepsilon_0 m}$, is the *plasma frequency* of the free electron gas. Therefore, the complex dielectric function of the free electron gas is given by

$$\varepsilon(\omega) \;=\; 1 - \frac{\omega_p^2}{\omega^2 + i\gamma\omega}\;, \tag{2.36}$$

where the real and imaginary parts are

$$\varepsilon'(\omega) = 1 - \frac{\omega_p^2}{\omega^2 + \gamma^2} , \tag{2.37}$$

$$\varepsilon''(\omega) = \frac{\omega_p^2 \gamma}{\omega(\omega^2 + \gamma^2)} . \tag{2.38}$$

As can be seen from Eq. (2.37), $\varepsilon'(\omega)$ vanishes at a frequency $\omega = \sqrt{\omega_p^2 - \gamma^2}$. With such a frequency dependent dielectric function, the solution of Maxwell's equations can be divided into three cases: (i) $\varepsilon' < 0$, (ii) $\varepsilon' > 0$, and (iii) $\varepsilon' = 0$ when $\omega = \sqrt{\omega_p^2 - \gamma^2}$. In region (i), $\varepsilon' < 0$, the solution to Maxwell's equations are exponentially damped waves. Thus, electromagnetic waves with a frequency below $\sqrt{\omega_p^2 - \gamma^2}$ can not exist within a free-electron gas: from a light-optical point of view the material is not transparent. In region (ii), $\varepsilon' > 0$, the solutions are transverse plane waves (damped because of a nonvanishing γ). As such, the electron gas becomes increasingly transparent for waves with frequencies above $\sqrt{\omega_p^2 - \gamma^2}$. In region (iii), at exactly $\omega = \sqrt{\omega_p^2 - \gamma^2}$, ε', the real part of the dielectric function $\varepsilon(\omega)$ vanishes. In this case, the solutions are associated with longitudinal electric waves, *i.e.* plasmons. These longitudinal modes (usually) appear as pronounced peaks. These modes are often referred to as volume plasmon or bulk plasmon. The classical Drude model describes the dielectric function of real metals, where the conduction electrons can be approximated as a free-electron gas relatively well. In the free-electron model, $\varepsilon \to 1$ at $\omega \gg \omega_p$. For the noble metals (e.g. Au, Ag, Cu), an extension to this model is needed in the region $\omega > \omega_p$ (where the response is dominated by free s electrons), since the filled d band close to the Fermi surface causes a highly polarized environment. This residual polarization due to the positive background of the ion cores can be described by adding the term $P_\infty = \varepsilon_0(\varepsilon_\infty - 1)E$ to (1.2a), where P now represents solely the polarization (1.18) due to free electrons. This effect is therefore described by a dielectric constant ε_∞ (usually $1 \leq \varepsilon_\infty \leq 10$), and we can write

$$\varepsilon(\omega) = \varepsilon_\infty - \frac{\omega_p^2}{\omega^2 + i\gamma\omega} . \tag{2.39}$$

2.2.1.2 The Lorentz Model

In metals, the optical response for photon energies below the threshold of transitions between electronic bands, is described satisfactorily by the complex dielectric function of the Drude model. However, for some of the noble metals, interband transitions, where electrons from the filled band below the Fermi surface are excited to higher bands, already start to occur for quite low energies (approximately 1 eV).

Then, despite the Drude model is sufficient describing the optical properties of metals, noble metals are inadequately described at visible frequencies. This can be overcome by adding an harmonic oscillator term $m\omega_L^2 u(t)$ to Eq. (2.32). By adding this term, interband transitions are thus described using the classical picture of a bound electron with resonance frequency ω_L. This Lorentz discrete transition frequency ω_L stands for the allowed quantum energy of conduction electron transitions from occupied states to unoccupied states (immediately outside of the conduction band).

Then, the equation of motion now reads

$$m\frac{\partial^2}{\partial t^2}u(t) + m\gamma\frac{\partial}{\partial t}u(t) + m\omega_L^2 u(t) \;=\; -eE(t)\ . \tag{2.40}$$

Following the same steps as for the derivation of the Drude dielectric function leads to

$$\varepsilon(\omega) \;=\; 1 - \frac{Ne^2/m\varepsilon_0}{(\omega^2-\omega_L^2)+i\gamma\omega}\ , \tag{2.41}$$

$$\;=\; 1 - \frac{f_L\omega_L^2}{(\omega^2-\omega_L^2)+i\gamma\omega}\ , \tag{2.42}$$

where f_L is a weighting factor, standing for the oscillator strengh of the transition, representing the probability of such an excitation. Then, the real and imaginary parts of the Lorentz dielectric functions read

$$\varepsilon'(\omega) \;=\; 1 - \frac{\omega_L^2(\omega^2-\omega_0^2)}{(\omega^2-\omega_0^2)^2+\gamma^2\omega^2}\ , \tag{2.43}$$

$$\varepsilon''(\omega) \;=\; \frac{\omega_L^2\omega\gamma}{(\omega^2-\omega_0^2)^2+\gamma^2\omega^2}\ . \tag{2.44}$$

Again, as for the Drude model, the frequency dependent behavior can roughly be divided into three regions: (i) $\omega \ll \omega_L$, (ii) $\omega \approx \omega_L$, and (iii) $\omega \gg \omega_L$. In region (i), ε'' is very small and hence there is almost no absorption. On the other hand, region (ii) exhibits a strong absorption. And in region (iii), the binding energy of the electrons is much smaller than the energy of the perturbation, then the electrons behave like a free electron gas. Similar to the Drude model, ε' vanishes at the frequency $\omega = \omega_L$, suggesting that plasmons can occur in non-metallic materials, since the condition for the occurrence of a plasmon excitation ($\varepsilon' = 0$) can still be fulfilled even if there bound electrons in the medium.

It should be noted that depending on the target, many different resonant oscillators with different frequency ω_j may exist and then, the Lorentz dielectric function should be written as sum over all individual resonators, then Eq. (2.42) should be writtes as

$$\varepsilon(\omega) \;=\; 1 - \sum_j \frac{f_j \omega_{Lj}^2}{(\omega^2 - \omega_{Lj}^2) + i\gamma_j \omega} \; . \tag{2.45}$$

2.2.1.3 The Drude-Lorentz Model

A medium, where both, free electrons and resonant oscillators in the form of interband transitions are present, can be described as a combination of the Drude and the Lorentz model. The first one describing the contribution of free electrons and the second one the contribution of bound electrons by a single or several oscillators.

Again, allowing j different resonant oscillators with frequencies ω_{Lj} and N_j electrons the dielectric function reads

$$\varepsilon(\omega) = 1 - \frac{\omega_p^2}{\omega^2 + i\gamma\omega} - \sum_j \frac{f_j \omega_{Lj}^2}{(\omega^2 - \omega_{Lj}^2) + i\gamma_j \omega} \; . \tag{2.46}$$

Eq. (2.46) is the general form of the Drude-Lorentz dielectric function. However, in order to perform numerical simulations it can be further simplified. Limiting the model to only one ($j = 1$) resonant oscillator (interband transition of energy difference $\hbar\omega_L$), the

dielectric function of Eq. (2.46) can be written as

$$\varepsilon(\omega) = 1 - \frac{\omega_p^2}{\omega^2 + i\gamma\omega} - \frac{f_L\omega_L^2}{(\omega^2 - \omega_L^2) + i\gamma_L\omega} \ , \tag{2.47}$$

where the subscript j of some of the parameters in Eq. (2.46) has been replaced by L to avoid misunderstandings.

Finally, as in the case of the Drude model, the residual polarization due to the positive background of the ion cores can be described by a dielectric constant ε_∞, then Eq. (2.47) reads

$$\varepsilon(\omega) = \varepsilon_\infty - \frac{\omega_p^2}{\omega^2 + i\gamma\omega} - \frac{f_L\omega_L^2}{(\omega^2 - \omega_L^2) + i\gamma_L\omega} \ . \tag{2.48}$$

As we will see in chapters 3 and 4 the Drude-Lorentz dielectric function described by Eq. (2.48) is qualitatively correct for the description of heavily doped semiconductor nanostructures.

It is worth to note that both in the Drude model and in the Drude-Lorentz model, the parameters, ω_p and γ_D , are directly related to the averaged conduction electrons density, n_e , their effective mass, m^*, their Fermi velocity, v_F, and their conductivity σ, through the well-known expressions [20]:

$$\omega_p = \sqrt{\frac{e^2 n_e}{\varepsilon_0 m^*}} \ , \tag{2.49}$$

$$\gamma_D = \gamma_{bulk} + \gamma_{surf} \simeq \frac{n_e e^2}{\sigma m^*} + \mathcal{A}\frac{v_F}{D} \ , \tag{2.50}$$

where the surface scattering contribution to the damping, γ_{surf} , is approximated in terms of a characteristic length of the nanoparticle, D, and a geometry-dependent parameter $\mathcal{A} \sim \infty$. Also, the number of carriers per molecular unit is $N_{cpm} = n_e M/(\rho N_A)$, where M is the molar mass, ρ is the mass density, and N_A is Avogadro's constant.

2.2.2 Analitical and Numerical Methods

Exact solutions to Maxwell's equations are known only for special geometries such as spheres, spheroids, or infinite cylinders. For targets of arbitrary shapes, numerical implemantations are needed such as the discrete-dipole approximation (DDA).

2.2.2.1 Scattering and Absorption of selected geometries

Localized surface plasmons are non-propagating excitations of the conduction electrons of metallic nanostructures coupled to the electromagnetic field. These modes arise naturally from the scattering problem of a small, sub-wavelength conductive nanoparticle in an oscillating electromagnetic field. The curved surface of the particle excerts an effective restoring force on the driven electrons, so that a resonance can arise, leading to field amplification both inside and in the near-field zone outside the particle. This resonance is called the *localized surface plasmon* or short localized plasmon resonance.

The interaction of a particle of size d with the electromagnetic field can be analyzed using the simple quasi-static approximation provided that the particle is much smaller than the wavelength of light in the surrounding medium. In this case, the phase of the harmonically oscillating electromagnetic field is practically constant over the particle volume, so that one can calculate the spatial field distribution by assuming the simplified problem of a particle in an electrostatic field. The harmonic time dependence can then be added to the solution once the field distributions are known. As we will show below, this lowest-order approximation of the full scattering problem describes the optical properties of nanoparticles of dimensions below 100 nm adequately for many purposes.

2.2.2.2 Spheres

We start with the most convenient geometry for an analytical treatment: a homogeneous, isotropic sphere of radius a located at the origin in a uniform, static electric field $E = E_0\hat{z}$[7].

[7]Se puede poner una figura.

The surrounding medium is isotropic and non-absorbing with dielectric constant ε_m, and the field lines are parallel to the z-direction at sufficient distance from the sphere. The dielectric response of the sphere is further described by the dielectric function $\varepsilon(\omega)$. In the electrostatic approach, we are interested in a solution of the Laplace equation for the potential, $\nabla^2\Phi = 0$, from which we will be able to calculate the electric field $E = -\nabla\Phi$. Due to the azimuthal symmetry of the problem, the general solution is of the form [135].

$$\Phi(r,\theta) = \sum_{l=0}^{\infty} \left[A_l r^l + B_l r^{-(l+1)}\right] P_l(\cos\theta) \ , \tag{2.51}$$

where $P_l(\cos\theta)$ are the Legendre Polynomials of order l, and θ is the angle between the position vector r at a point "P" and the z-axis. Due to the requirement that the potentials remain finite at the origin, and applying the appropiate boundary conditions the solution for the potentials Φ_{in} inside and Φ_{out} outside the sphere, these can be written as

$$\Phi_{in} = -\frac{3\varepsilon_m}{\varepsilon + 2\varepsilon_m} E_0 r\cos\theta \ , \tag{2.52}$$

$$\Phi_{out} = -E_0 r\cos\theta + \frac{\varepsilon - \varepsilon_m}{\varepsilon + 2\varepsilon_m} E_0 a^3 \frac{\cos\theta}{r^2} \ . \tag{2.53}$$

It is worth to note that Φ_{out} describes the superposition of the applied field and that of a dipole located at the particle center, then we can rewritte Φ_{out} by introducing the dipole moment $\mathbf{p}$ as

$$\Phi_{out} = -E_0 r\cos\theta + \frac{\mathbf{p}\cdot\mathbf{r}}{4\pi\varepsilon_0\varepsilon_m r^3} \ , \tag{2.54}$$

with

$$\mathbf{p} = 4\pi\varepsilon_0\varepsilon_m a^3 \ \frac{\varepsilon - \varepsilon_m}{\varepsilon + 2\varepsilon_m}\mathbf{E}_0 \ . \tag{2.55}$$

Therefore, we see that the applied field induces a dipole moment inside the sphere of magnitude proportional to $|\mathbf{E}_0|$. Then, if we introduce the complex *polarizability* α of a small sphere of sub-wavelength diameter in the electrostatic ap- proximation, defined via

$\mathbf{p} = \varepsilon_0 \varepsilon_m \alpha \mathbf{E}_0$, we arrive at

$$\alpha = 4\pi a^3 \ \frac{\varepsilon - \varepsilon_m}{\varepsilon + 2\varepsilon_m} \ . \tag{2.56}$$

We note that it shows the same functional form as the Clausius- Mossotti relation [135]. It is apparent that the polarizability experiences a resonant enhancement under the condition that $|\varepsilon + 2\varepsilon_m|$ is a minimum, which for the case of small or slowly-varying Im$[\varepsilon]$ around the resonance simplifies to

$$\mathrm{Re}[\varepsilon(\omega)] = -2\varepsilon_m \ . \tag{2.57}$$

This relationship is called the Fröhlich condition and the associated mode (in an oscillating field) the dipole surface plasmon of the metal nanoparticle. For a sphere consisting of a Drude metal with a dielectric function (1.20) located in air, the Fröhlich criterion is met at the frequency $\omega_0 = \omega_p/\sqrt{3}$. Eq. (2.57) further expresses the strong dependence of the resonance frequency on the dielectric environment: The resonance red-shifts as ε_m is increased. Metal nanoparticles are thus ideal platforms for optical sensing of changes in refractive index. We note that the magnitude of α at resonance is limited by the incomplete vanishing of its denominator, due to Im$[\varepsilon(\omega)] \neq 0$.

The distribution of the electric field $\mathbf{E} = -\nabla\Phi$ can be evaluated from the potentials (2.52) and (2.54) to

$$E_{in} \ = \ \frac{3\varepsilon_m}{\varepsilon + 2\varepsilon_m} E_0 \ , \tag{2.58}$$

$$E_{out} \ = \ E_0 + \frac{3\mathbf{n}(\mathbf{n}\cdot\mathbf{p}) - \mathbf{p}}{4\pi\varepsilon_0\varepsilon_m} \ \frac{1}{r^3} \ . \tag{2.59}$$

As expected, the resonance in α also implies a resonant enhancement of both the internal and dipolar fields. Now, for small spheres with radius $a \ll \lambda$, its representation as an ideal dipole is valid in the quasi-static regime, *i.e.* allowing for time-varying fields but neglecting spatial retardation effects over the particle volume. Under plane-wave illumination with $E(r,t) = E_0 e^{-i\omega t}$, the fields induce an oscillating dipole moment $\mathbf{p}(t) = \varepsilon_0\varepsilon_m\alpha E_0 e^{-i\omega t}$,

with α given by the electrostatic result of Eq. (2.56). The radiation of this dipole leads to scattering of the plane wave by the sphere, which can be represented as radiation by a point dipole. From the viewpoint of optics, it is much more interesting to note that another consequence of the resonantly enhanced polarization α is a concomitant enhancement in the efficiencywith which a metal nanoparticle scatters and absorbs light. The corresponding cross sections for scattering and absorption C_{sca} and C_{abs} can be calculated via the Poynting vector [3] to

$$C_{sca} = \frac{k^4}{6\pi} |\alpha|^2 = \frac{8\pi}{3} k^4 a^6 \left| \frac{\varepsilon - \varepsilon_m}{\varepsilon + 2\varepsilon_m} \right|^2 , \tag{2.60}$$

$$C_{abs} = k \, \mathrm{Im}[\alpha] = 4\pi k a^3 \, \mathrm{Im} \left[\frac{\varepsilon - \varepsilon_m}{\varepsilon + 2\varepsilon_m} \right] . \tag{2.61}$$

For small particles with $a \ll \lambda$, the efficiency of absorption, scaling with a^3, dominates over the scattering efficiency, which scales with a^6. We point out that no explicit assumptions were made in our derivations so far that the sphere is indeed metallic. Eqs. (2.60) and (2.61) whith the expressions for the cross sections, are thus valid also for dielectric scatterers, and demonstrate a very important problem for practical purposes. Due to the rapid scaling of $C_{sca} \propto a^6$, it is very difficult to pick out small objects from a background of larger scatterers. They also shows that indeed for metal nanoparticles both absorption and scattering (and thus extinction) are resonantly enhanced at the dipole particle plasmon resonance, *i.e.* when the Frölich condition given by Eq. (2.57) is met [20]. For a sphere of volume V and dielectric function $\varepsilon = \varepsilon' + i\varepsilon''$ in the quasi-static limit, then the explicit expression for the extinction cross section $C_{ext} = C_{abs} + C_{sca}$ is

$$C_{ext} = 9 \, \frac{\omega}{c} \varepsilon_m^{3/2} V \frac{\varepsilon''}{[\varepsilon' + 2\varepsilon_m]^2 + \varepsilon''^2} . \tag{2.62}$$

2.2.2.3 Ellipsoids

We now relax the assumption of a spherical nanoparticle shape. However, it has to be pointed out that the basic physics of the localized surface plasmon resonance of a subwavelength metallic nanostructure is well described by this special case. A slightly more

general geometry amenable to analytical treatment in the electrostatic approximation is that of an ellipsoid with semiaxes $a_1 \leq a_2 \leq a_3$, specified by $x^2/a_1^2 + y^2/a_2^2 + z^2/a_3^2 = 1$. A treatment of the scattering problem in ellipsoidal coordinates [3] leads to the following expression for the polarizabilities α_i along the principal axes ($i = 1, 2, 3$):

$$\alpha_i \;=\; 4\pi\; a_1 a_2 a_3\; \frac{\varepsilon - \varepsilon_m}{3\varepsilon_m + 3L_i(\varepsilon - \varepsilon_m)}\;, \tag{2.63}$$

where L_i is a geometrical factor given by

$$L_i \;=\; \frac{a_1 a_2 a_3}{2} \int_0^\infty \frac{dq}{(a_i^2 + q) f(q)}\;, \tag{2.64}$$

with $f(q) = \sqrt{(q + a_1^2)(q + a_2^2)(q + a_3^2)}$. The geometrical factors satisfy $\sum L_i = 1$, and for a sphere $L_i = 1/3$. An important special class of ellipsoids are spheroids. For prolate spheroids, the two minor axes are equal ($a_2 = a_3$), while for oblate spheroids, the two major axes are of same size ($a_1 = a_2$). An examination of Eq. (2.63) reveals that a spheroidal metal nanoparticle exhibits two spectrally separated plasmon resonances, corresponding to oscillations of its conduction electrons along the major or minor axis, respectively. The resonance due to oscillations along the major axis can show a significant spectral red-shift compared to the plasmon resonance of a sphere of the same volume. Thus, plasmon resonances can be lowered in frequency into the near-infrared region of the spectrum using metallic nanoparticles with large aspect ratio. For a quantitative treatment, we note however that Eq. (2.63) is only strictly valid as long as the major axis is significantly smaller than the excitation wavelength.

An equivalent approach can be obtained from the Mie-Gans Theory, where a first rough estimation of the optical properties of an elongated nanoparticle can be made by neglecting its detailed shape and by considering a prolate spheroid of aspect ratio R instead, then

the LSPR absorbance $A(\omega)$ of a solution of prolate spheroids is given by

$$A(\omega) \propto \varepsilon_m^{3/2} \sum_j \frac{\left(\frac{1}{P_j^2}\right)\varepsilon_2}{\left(\varepsilon_1 + \frac{1-P_j}{P_j}\varepsilon_m\right)^2 + \varepsilon_2^2} , \tag{2.65}$$

where ω_m is the dielectric constant of the medium, and P_j are the depolarization factors for axes three axis (x, y, and x) of the spheroid. Assuming that axes x and y have the same width for a prolate speroid. The depolarization factors, then, the absorptions for axial and perpendicular incident E-field polarizations are respectively given by the well-known expressions [3, 4]:

$$A_z(\omega) \propto \omega\varepsilon_m^{3/2} \frac{\varepsilon_2(\omega)}{[\mathcal{P}_z\varepsilon_1(\omega) + (1-\mathcal{P}_z)\varepsilon_m]^2 + \varepsilon_2^2(\omega)} , \tag{2.66}$$

$$A_\perp(\omega) \propto \omega\varepsilon_m^{3/2} \frac{\varepsilon_2(\omega)}{[(1-\mathcal{P}_z)\varepsilon_1(\omega) + (1+\mathcal{P}_z)\varepsilon_m]^2 + \varepsilon_2^2(\omega)} , \tag{2.67}$$

where P_z is given by

$$P_z = \frac{1}{R_{eff}^2 - 1}\left[\frac{R_{eff}}{2\sqrt{R_{eff}^2 - 1}} \ln\left(\frac{R_{eff} + \sqrt{R_{eff}^2 - 1}}{R_{eff} - \sqrt{R_{eff}^2 - 1}}\right) - 1\right] , \tag{2.68}$$

where R_{eff} is the aspect ratio of the spheroid (long axis divided by short axis).

The maxima of Eqs. 2.66 and 2.67 correspond to the frequencies of LSPRs for axial and perpendicular E-field polarization respectively. In the limit of small loses, such frequencies are well approximated by the zeroes of the first terms in the denominators in Eqs. 2.66 and 2.67. In addition, if we assume that $\varepsilon_\infty + \mathrm{Re}[\varepsilon_L(\omega)]$ weakly depends on ω in the region where LSPs arise, the LSP frequencies for prolate spheroids are

$$\frac{\omega_{LSP}}{\omega_p} \simeq \begin{cases} \left(\bar{\varepsilon}_b + \frac{1-P_z}{Pz}\varepsilon_m\right)^{-1/2} & \text{(axial)} , \\ \left(\bar{\varepsilon}_b + \frac{1+P_z}{1-Pz}\varepsilon_m\right)^{-1/2} & \text{(perp)} \end{cases} \tag{2.69}$$

$\bar{\varepsilon}_b$ being a constant that accounts in an averaged manner for the contribution by $\tilde{\varepsilon}_\infty +$

$\mathrm{Re}[\varepsilon_L(\omega)]$.

For a very elongated spheroid ($R_{eff} \gg 1$) we have that $P_z \simeq R_{eff}^{-2} \ln(2R_{eff})$, which is very small. Therefore, the frequency of the axial LSP for elongated spheroids is $\omega_z \simeq (P_z/\varepsilon_m)^{1/2}\omega_P$, regardless the non-Drude contributions to the dielectric response. This behaviour also appears in the collective excitations of long coinage-metal nanorods [136, 137], although in this case the Lorentz-like excitations arise from occupied d-orbitals. On the contrary, the ionic and bound-electron polarizability do always contribute to the frequency of the perpendicular LSP, $\omega_\perp$. In particular, $(\bar{\varepsilon}_b + 2\varepsilon_m)^{-1/2}\omega_P \leq \omega_\perp < (\bar{\varepsilon}_b + \varepsilon_m)^{-1/2}\omega_p$, and the more important the non-Drude contributions to $\varepsilon(\omega)$ are, the narrower the frequency interval where $\omega_\perp$ lies in.

2.2.2.4 Arbitrary Geometries and Discrete Dipole Approximation (DDA)

The DDA, originally developed by Purcell and Pennypacker [138], is a general method for computing scattering and absorption by a particle of arbitrary shape. It works by considering the continuum-solid target as a finite array of polarizable point dipoles with the spacing between them small compared to the wavelength. The points acquire dipole moments in response to the local electric field. The dipoles of course interact with one another via their electric fields [138, 139], so the DDA is also sometimes referred to as the coupled dipole approximation [140, 141]

We may expect that, just as a continuum representation of a solid is appropriate on length scales that are large compared with the interatomic spacing, an array of polarizable points can accurately approximate the response of a continuum target on length scales that are large compared with the interdipole separation. For a finite array of point dipoles the scattering problem may be solved exactly, so the only approximation that is present in the DDA is the replacement of the continuum target by an array of N-point dipoles.

The replacement requires specification of both the geometry (location r_j of the dipoles $j = 1, ..., N$) and the dipole polarizabilities α_j.

For monochromatic incident waves the self-consistent solution for the oscillating dipole moments P_j may be found. From these P_j the absorption and scattering cross sections are computed [139].

The electromagnetic scattering problem must be solved for the target array of point dipoles ($j = 1, ..., N$) with polarizabilities α_j, located at positions r. Each dipole has a polarization $P_j = \alpha_j E_j$, where E_j is the electric field at r that is due to the incident wave $E_{inc} = E_0 e^{ik\cdot r - i\omega t}$ plus the contribution of each of the other $N - 1$ dipoles

$$E_j \;=\; E_{inc,j} - \sum_{k\neq j} A_{jk} P_k \;, \tag{2.70}$$

where $-A_{jk}P_k$ is the electric field at r_j due to the dipole P_k at location r_k. Defining $A_{jj} = \alpha_j^{-1}$ reduces the scattering problem to finding the polarizations P_j that satisfy a system of $3N$ complex linear equations

$$\sum_{k=1}^{N} A_{jk} P_k \;=\; E_{inc,j} \;. \tag{2.71}$$

Once Eq. (2.71) has been solved for the unknown polarizations P_j, the extinction and absorption cross sections C_{ext} and C_{abs} may be evaluated [139]:

$$C_{ext} \;=\; \frac{4\pi k}{|E_0^2|} \sum_{j=1}^{N} \mathrm{Im}\left[E_{inc,j}^{*} \cdot P_j\right] \;, \tag{2.72}$$

$$C_{abs} \;=\; \frac{4\pi k}{|E_0^2|} \sum_{j=1}^{N} \left\{ \mathrm{Im}\left[P_j \cdot (\alpha^{-1})^{*} P_j^{*}\right] - \frac{2}{3} k^3 |P_j|^2 \right\} \;. \tag{2.73}$$

Then, the scattering cross section $C_{sca} = C_{ext} - C_{abs}$.

2.3 Ab-initio approach from TDDFT [8]

Electron spill-out and tunneling are basic manifestations of quantum mechanics which, in principle, can be only extracted from the many-electron wavefunction or approximations

[8] This section is based on Ref. [142].

thereof. The rationale behind hydrodynamic models is the assumption that the quantum motion of electrons can be addressed just by using density and velocity fields [143]. Note that in standard classical nonlocal optics the induced electron density is indeed inhomogeneous but strictly confined into well-defined boundaries. Therefore, just by removing this constraint we should have a clear improvement upon the present prescriptions of nonlocal classical optics. The merit of this "self-consistent" hydrodynamic approximation (HA) is not only the approximate inclusion of genuine quantum effects, but also the possibility of solving Maxwell's equations without imposing any boundary condition at metal-dielectric interfaces. The electron-density varies smoothly over the whole space and both Maxwell's equations and the hydrodynamic equation of motion are solved simultaneously. Only very recently a HA has been presented as a practical tool for the analysis of the optical response from the perspective of classical plasmonics [64]. However, the very same hydrodynamic prescription is well-known in condensed-matter and cluster physics from a long time [73, 143, 144]. For instance, the photoabsorption spectrum of metal nanoparticles [145, 146], magnetoplasmon excitations [147], and even nonlinear ultrafast electron dynamics [148] have been already analyzed under the HA.

The approach to the electron-light interaction in condensed matter physics is quite different. Even if the EM field is considered as a classical entity, theoretical efforts are directed towards the efficient but accurate solution of the quantum many-electron problem. Many-body perturbation theory or time-dependent density functional theory (TDDFT) [71] are the methods of choice in ab-initio condensed-matter physics [72], and the *quantum* plasmon is simply one of the plethora of the elementary excitation processes in many-body systems. A plasmon in an extended system (bulk or surface) consists of a coherent continuous set of single-electron excitations [20, 73, 149, 150]. However, in a localized system where the one-electron energy levels are discrete, the analysis of collective excitation must be carried out with care. For example, whether a spectral peak in the absorption spectrum of a finite electron system can be labelled as a plasmon or not is still a matter of debate [151–155]. In any case, the quantum picture of the plasmon always relies on its microscopic description (a "bottom-up" procedure), whereas the classical pictures starts

from the macroscopic outcome (the induced density), corresponding to a "top-down" approach. From this point of view, HA is an oversimplification of the electron dynamics where single-electron transitions are neglected.

Among the quantum many-body theoretical methods, TDDFT has become the preferred tool to evaluate optical properties in intermediate and large nanosystems (for a detailed discussion on the foundations and applications of TDDFT see Refs. ([72,74,156–158]). It has the advantage of describing the correlated dynamics of electrons in terms of independent particles. Therefore, the calculation of the time evolution of many-electron systems is achievable because the complicated many-body features are contained in the so-called exchange-correlation (XC) potential, $v_{\rm XC}(r,t)$.

2.3.1 TDDFT

TDDFT is the formal extension of the Hohenberg-Kohn-Sham density functional theory (DFT) [159, 160]. According to DFT, for an N-electron system under the action of an external potential $v_{\rm ext}(\boldsymbol{r})$ we have the three following exact statements: **i)** The ground-state electron density $n_0(\boldsymbol{r})$, unambiguously defines the many-electron ground state $|\Psi_0\rangle$; **ii)** There exists an *energy functional* $E\,[n]$ whose minimum equals the ground-state energy and its reached at $n(\boldsymbol{r}) = n_0(\boldsymbol{r})$; **iii)** The minimization can be made by defining a fictitious system of independent fermions, the so-called Kohn-Sham (KS) system, whose ground-state density is also $n_0(\boldsymbol{r})$. In Hartree atomic-units ($m_e = \hbar = e = 1$) the energy functional is

$$E[n] = T_{\rm S}[n] + W_{\rm H}[n] + E_{\rm XC}[n] + \int v_{\rm ext}(\boldsymbol{r}) n(\boldsymbol{r})\; d\boldsymbol{r}\;, \tag{2.74}$$

where $T_{\rm S}[n]$ is the kinetic energy of a fictitious KS system with density $n(\boldsymbol{r})$, $W_{\rm H}[n]$ is the *classical* electron-electron interaction energy, $E_{\rm XC}[n]$ is the so-called exchange-correlation (XC) functional, and the last term in the right hand side of Eq. (2.74) is the interaction energy with the external potential. As a consequence, the universal functional $E_{\rm XC}[n]$ contains all the quantum many-body corrections to the classical electron-electron interaction energy and to the kinetic energy of the KS system. By imposing the variational

character of $E[n]$, we arrive at the well-known set of self-consistent Kohn-Sham equations for the ground state:

$$\left(\hat{t} + \hat{v}_{\rm ext} + \hat{v}_{\rm XC} + \hat{v}_{\rm H}\right)|\phi_n\rangle = \varepsilon_n|\phi_n\rangle \ ; \tag{2.75}$$

$$v_{\rm XC}(\boldsymbol{r}) = \left.\frac{\delta E_{\rm XC}[n]}{\delta n(\boldsymbol{r})}\right|_{n=n_0} \ , \ v_{\rm H}(\boldsymbol{r}) = \int \frac{n_0(\boldsymbol{r}_1)}{|\boldsymbol{r}-\boldsymbol{r}_1|} d\boldsymbol{r}_1 \tag{2.76}$$

$$n_0(\boldsymbol{r}) = \sum_\sigma \sum_{n=1}^{N} |\phi_n(\boldsymbol{r},\sigma)|^2 \ \ \text{with} \ \ \varepsilon_1 \leq \varepsilon_2 \leq .... \ , \tag{2.77}$$

where $\hat{t}$ is the one-electron kinetic-energy operator, $|\phi_n\rangle$ are normalized one-electron states, ε_n are their corresponding eigenenergies, and σ is the spin orientation. Hence, the effective one-body potential $\hat{v}_{\rm S} = \hat{v}_{\rm ext} + \hat{v}_{\rm XC} + \hat{v}_{\rm H}$ defines the fictitious KS system of N independent fermions. The only unknown ingredient is the XC functional, and practical applications rely on approximations to $E_{\rm XC}[n]$. The success and popularity of KS-DFT is due to the accuracy obtained by using very simple functional forms of $E_{\rm XC}[n]$, like the local-density (LDA) or generalized-gradient (GGA) approximations [156]. Let us suppose that at $t = 0$ an external perturbation acts on the many-body ground-state $|\Psi_0\rangle$, that is, for $t \geq 0$ the external potential is $v_{\rm ext}(\boldsymbol{r},t) = v_{\rm ext}(\boldsymbol{r}) + \delta v_{\rm ext}(\boldsymbol{r},t)$. For instance, $\delta v_{\rm ext}(\boldsymbol{r},t)$ can be the scalar potential of an incident EM field in the quasi-static approximation (i.e. neglecting retardation effects). The Runge-Gross theorem [71] states that, under very general conditions, the dynamical evolution of the system is the direct time-dependent extension of the ground-state KS equations. Namely, the static Schrödinger equation given by Eq. (2.75) is replaced by its dynamical counterpart

$$\left(\hat{t} + \hat{v}_{\rm ext}(t) + \hat{v}_{\rm XC}(t) + \hat{v}_{\rm H}(t)\right)|\phi_n(t)\rangle = {\rm i}\frac{d}{dt}|\phi_n(t)\rangle \ , \tag{2.78}$$

with the initial conditions $|\phi_n(t=0)\rangle = |\phi_n\rangle$. Here, $v_{\rm H}(\boldsymbol{r},t)$ is the classical Coulomb potential generated by the density $n(\boldsymbol{r},t)$, $v_{\rm XC}(\boldsymbol{r},t)$ is the XC potential for $n(\boldsymbol{r},t)$, and the density itself is given by

$$n(\boldsymbol{r},t) = \sum_\sigma \sum_{n=1}^{N} |\phi_n(\boldsymbol{r},\sigma;t)|^2 \ . \tag{2.79}$$

However, the time-dependent XC potential *is not* the functional derivative of any other functional, but actually a functional of all the electron densities at times $t' < t$. Fortunately, such memory effects can be safely neglected when studying the plasmonic response of a nanosystem. This is the so-called *adiabatic* prescription of TDDFT, where $v_{\rm XC}(\vec{r},t)$ is obtained from the density $n(\vec{r},t)$ at the same time t from

$$v_{\rm XC}(\boldsymbol{r},t) \simeq \left.\frac{\delta E_{\rm XC}[n]}{\delta n(\boldsymbol{r})}\right|_{n=n(\boldsymbol{r},t)} , \tag{2.80}$$

$E_{\rm XC}[n]$ being the XC energy functional used to evaluate the unperturbed ground-state density. If, in addition, $E_{\rm XC}[n]$ is formulated under the LDA or the GGA, we have the so-called adiabatic- LDA (ALDA) or GGA approximations. In the limit of very weak perturbations (linear response regime), the excitation rate due to an external time-dependent perturbation $\delta v_{\rm ext}(\boldsymbol{r},\omega)e^{-{\rm i}\omega t}$ is given by

$$\mathrm{w}(\omega) = -2\ \mathrm{Im}\left[\int \delta v^{*}_{\rm ext}(\boldsymbol{r},\omega)\delta n(\boldsymbol{r},\omega)\ d\boldsymbol{r}\ \right], \tag{2.81}$$

where $\delta n(\boldsymbol{r},\omega)e^{-{\rm i}\omega t} = n(\boldsymbol{r},t) - n_0(\boldsymbol{r})$ is the induced density by such a perturbation. In this linear regime, the induced density can be written as

$$\delta n(\boldsymbol{r},\omega) = \int \chi(\boldsymbol{r},\boldsymbol{r}_1,\omega)\delta v_{\rm ext}(\boldsymbol{r}_1,\omega)\ d\boldsymbol{r}_1\ , \tag{2.82}$$

$\chi(\boldsymbol{r},\boldsymbol{r}_1,\omega)$ being the density-density response of the unperturbed many-electron ground state $|\Psi_0\rangle$ [161]. However, according to the Runge-Gross theorem, $\delta n(\boldsymbol{r},\omega)e^{-{\rm i}\omega t}$ is also the induced density of the KS system but due to a perturbation $\delta v_{\rm S}(\boldsymbol{r},\omega)e^{-{\rm i}\omega t}$ which is equal to the the external one plus the induced Coulomb and XC potentials. That is,

$$\delta n(\boldsymbol{r},\omega) = \int \chi_{\rm S}(\boldsymbol{r},\boldsymbol{r}_1,\omega)\delta v_{\rm S}(\boldsymbol{r}_1,\omega)\ d\boldsymbol{r}_1\ , \tag{2.83}$$

where $\chi_{\rm S}(\boldsymbol{r},\boldsymbol{r}_1,\omega)$ is the linear response of the KS system of independent electrons, and

$$\delta v_{\rm S}(\boldsymbol{r},\omega) = \delta v_{\rm ext}(\boldsymbol{r},\omega) + \int \frac{\delta n(\boldsymbol{r},\omega)}{|\boldsymbol{r}-\boldsymbol{r}_1|} d\boldsymbol{r}_1 + \delta v_{\rm XC}(\boldsymbol{r},\omega)\ . \tag{2.84}$$

The induced XC potential, $\delta v_{\rm XC}(\boldsymbol{r},\omega)$, is formally given by [162]

$$\delta v_{\rm XC}(\boldsymbol{r},\omega) = \int K_{\rm XC}(\boldsymbol{r},\boldsymbol{r}_1,\omega)\delta n(\boldsymbol{r}_1,\omega)d\boldsymbol{r}_1 \ , \tag{2.85}$$

where $K_{\rm XC}(\boldsymbol{r},\boldsymbol{r}_1,\omega)$ is the frequency representation of the so-called dynamical XC kernel

$$K_{\rm XC}(\boldsymbol{r},\boldsymbol{r}_1,t-t_1) = \frac{\delta v_{\rm XC}(\boldsymbol{r},t)}{\delta n(\boldsymbol{r}_1,t_1)} \ . \tag{2.86}$$

On the other hand, the linear response function $\chi_{\rm S}$ can be evaluated in terms of the stationary orbitals $\phi_k(\boldsymbol{r},\sigma)$ with eigenenergies ε_k of the KS Hamiltonian $\hat{h}_{\rm S} = \hat{t} + \hat{v}_{\rm S}$ as follows:

$$\begin{aligned}\chi_{\rm S}(\boldsymbol{r}_1,\boldsymbol{r}_2,\omega) &= \sum_\sigma \sum_{n=1}^{N} \phi_n^*(\boldsymbol{r}_1,\sigma) G_{\rm S}^{(\sigma)}(\boldsymbol{r}_1,\boldsymbol{r}_2,\varepsilon_n+\omega)\phi_n(\boldsymbol{r}_2,\sigma) \\ &\quad + \sum_\sigma \sum_{n=1}^{N} \left[\phi_n^*(\boldsymbol{r}_1,\sigma) G_{\rm S}^{(\sigma)}(\boldsymbol{r}_2,\boldsymbol{r}_1,\varepsilon_n-\omega)\phi_n(\boldsymbol{r}_2,\sigma)\right]^* \end{aligned} \tag{2.87}$$

$G_{\rm S}^{(\sigma)}(\boldsymbol{r}_1,\boldsymbol{r}_2,\Omega)$ being the Green's function

$$\hat{G}_{\rm S}^{(\sigma)}(\boldsymbol{r}_1,\boldsymbol{r}_2,\Omega) = \sum_k \frac{\phi_k(\boldsymbol{r}_1,\sigma)\phi_k^*(\boldsymbol{r}_2,\sigma)}{\Omega - \varepsilon_k + {\rm i}0^+} \ . \tag{2.88}$$

Finally, putting together Eqs. (2.82)–(2.85), we arrive at a linear equation for the induced density which, in matrix notation, reads as

$$[1 - \hat{\chi}_{\rm S}(\omega)\hat{K}_{\rm HXC}(\omega)]\delta n(\boldsymbol{r},\omega) = \hat{\chi}_{\rm S}(\omega)\delta v_{\rm ext}(\boldsymbol{r},\omega) \ , \tag{2.89}$$

where

$$K_{\rm HXC}(\boldsymbol{r}_1,\boldsymbol{r}_2,\omega) = \frac{1}{|\boldsymbol{r}_2-\boldsymbol{r}_1|} + K_{\rm XC}(\boldsymbol{r}_1,\boldsymbol{r}_2,\omega) \ . \tag{2.90}$$

Once $\delta n(\boldsymbol{r},\omega)$ has been obtained, the excitation rate is evaluated from Eq. (2.81) and the energy absorption rate of the system is equal to ω w(ω).

The excitation rate given by Eq. (2.81) is singular when ω is equal to an excitation energy

Ω of the many-body electron system, and from Eq. (2.89) we get that Ω must be a zero of the operator $1 - \hat{\chi}_{\rm S}(\omega)\hat{K}_{\rm HXC}(\omega)$. It also means that $\hat{\chi}_{\rm S}(\omega)\hat{K}_{\rm HXC}(\omega)$ has an eigenvalue equal to one, which is the basis of TDDFT matrix formulations amenable for quantum chemistry calculations [163, 164]. Also note that the limit $\hat{K}_{\rm HXC}(\omega) \to 0$ (that is, in the limit of independent-electron response) those zeros become the poles of $\hat{\chi}_{\rm S}(\omega)$. The latter are, of course, the one-electron excitation energies $\varepsilon_f - \varepsilon_i$ of the KS system.

We need approximations to $K_{\rm HXC}(\boldsymbol{r}_1, \boldsymbol{r}_2, \omega)$ for practical implementations of linear response TDDFT. Under the adiabatic approximation given by Eq. (2.80), the memory effects into the XC potential are neglected. In this case, $K_{\rm XC}(\boldsymbol{r}_1, \boldsymbol{r}_2, \omega)$ does not depend on the frequency and is simply given by

$$K_{\rm XC}(\boldsymbol{r}_1, \boldsymbol{r}_2, \omega) \simeq \left. \frac{\delta v_{\rm XC}(\boldsymbol{r})}{\delta n(\boldsymbol{r})} \right|_{n=n(\boldsymbol{r},t)} , \tag{2.91}$$

and $v_{\rm XC}(\boldsymbol{r})$ can be obtained, for instance, under the LDA. This linear-response ALDA had been already proposed by Zangwill and Solven in 1980 to evaluate the photoabsorption spectra of several rare-gas atoms [165]. The same recipe was applied in seminal works by Eckardt [166] and Puska *et al* [167], to study the optical absorption properties of spherical-jellium clusters.

The number of unoccupied KS states entering into the calculation of the Green function given by Eq. (2.88) is, in general, a critical convergence parameter. However, the evaluation of such an infinite sum can be circumvented for high-symmetry systems by solving the Schrödinger-like equation satisfied by the Green function.

Focusing on nanoparticles with spherical symmetry, it is fairly easy to calculate and analyze the optical absorption of simple sp-metal nanoparticles described by the spherical jellium model [166–170]. In general, good agreements with experiments are obtained after replacing the term $\mathrm{i}0^+$ of Eq. (2.88) by a finite contribution $\mathrm{i}\eta$ with $\eta \sim 0.1$ eV aimed at mimicking non-electronic decay channels (electron-phonon interaction, for instance) and shape/size dispersion in experimental samples [20, 171, 172]. Moreover, the dynamical screening by d electrons, which plays a prominent role in the optical absorption of noble-

metal particles [91, 150, 173, 174], can be simulated in spherical-jellium calculations by a dielectric background with an appropriate permittivity $\epsilon_{\rm b}(\omega)$ (see Eq. (2.36) [175]. Finally, the combination of effective dielectric media and suitable confining potentials can be used to get insights on the optical properties of doped semiconductor nanocrystals while keeping the simplicity of the spherical jellium model [176]. The TDDFT evaluation of optical absorption spectra of metal nanoparticles containing several thousands of conduction electrons can also be addressed at an affordable computational cost as long as the spherical symmetry is preserved [177–182]. This allows us, for instance, to compare the optical absorption of isolated metal nanoparticles at different size-regimes. For each frequency of the external E-field, $\boldsymbol{E}_{\rm ext}(\mathbf{r},t) = E_0 \exp(-{\rm i}\omega t)\boldsymbol{e}_x$ [i.e. $\delta v_{\rm ext}(\boldsymbol{r},\omega) = xE_0$] we evaluate the induced density using Eq. (2.89). The dynamical polarizability is then given by the induced electric dipole divided by the amplitude of the incident E-field:

$$\alpha(\omega) = -\frac{1}{E_0}\int x\delta n(\boldsymbol{r},\omega)d\boldsymbol{r}\ , \tag{2.92}$$

whereas the photoabsorption cross-section is given by

$$\sigma_{\rm abs}(\omega) = \frac{4\pi\omega}{c}\,{\rm Im}\ \alpha(\omega)\ . \tag{2.93}$$

For low-symmetry systems, other possibilities exist to circumvent the explicit sum over unoccopied states in the evaluation of the KS-system linear response. For instance, by using the Sternheimer method it is possible to rewrite the response equations in frequency domain in such a way that the explicit use of the virtual KS states is not needed [183]. Another prescription, which is what we follow from now on, is the explicit resolution of the KS time-dependent Eqs. (2.78) [184]. For instance, if we apply at $t = 0$ a "kick" perturbing potential $\delta v_{\rm ext}(\boldsymbol{r},t) = \tau_0 v_0(\boldsymbol{r})\delta(t)$ the KS wavefunctions at $t = 0^+$ will be

$$\phi_n(\boldsymbol{r},\sigma;0^+) = e^{-{\rm i}\tau_0 v_0(\boldsymbol{r})/\hbar}\phi_n(\boldsymbol{r},\sigma)\ \ ;\ \ 1 \le n \le N\ , \tag{2.94}$$

and for $t > 0^+$ the evolution of the KS system can be obtained from Eq. (2.78) just setting

$\delta v_{\rm ext} = 0$. Since

$$\delta v_{\rm ext}(\boldsymbol{r},t) = \tau_0 v_0(\boldsymbol{r})\delta(t) = \frac{\tau_0}{2\pi}\int_{-\infty}^{+\infty} v_0(\boldsymbol{r})e^{-{\rm i}\omega t}d\omega \ , \tag{2.95}$$

the Dirac-Delta kick is, up to a factor, the superposition of all the monochromatic perturbations $v_0(\boldsymbol{r})\exp(-{\rm i}\omega t)$. If τ_0 is very small, linear response theory guarantees that there will be no coupling between the responses due to different frequencies. Therefore, if $\delta n(\boldsymbol{r},t)$ is the time-dependent induced density given by the time propagation of the KS equations after the Dirac-Delta kick, the density induced by the perturbation $v_0(\boldsymbol{r})\exp(-{\rm i}\omega t)$ is

$$\delta n(\boldsymbol{r},\omega) = \frac{1}{\tau_0}\int_0^{+\infty} \delta n(\boldsymbol{r},t)e^{+{\rm i}\omega t}dt \ , \tag{2.96}$$

since $\delta n(\boldsymbol{r}, t<0) = 0$. The corresponding excitation rate given by Eq. (2.81) is then

$$\mathrm{w}(\omega) = -2\int v_0(\boldsymbol{r})\left[\mathrm{Im}\ \ \delta n(\boldsymbol{r},\omega)\right]\ d\boldsymbol{r} \ , \tag{2.97}$$

and if $v_0(\boldsymbol{r}) = x_i E_0$ (with $i = x, y, z$), the polarizability tensor can be evaluated from

$$\alpha_{ji}(\omega) = -\frac{1}{E_0}\int x_j \delta n(\boldsymbol{r},\omega)d\boldsymbol{r} \ . \tag{2.98}$$

Therefore, the dipole optical-absorption spectrum can be obtained from a single time propagation (or three if we are interested in the full polarizability tensor). The critical convergence parameter is the time-propagation time $T_{\rm max}$ and, in practice, a damping factor $\exp(-\eta t)$ is included into Eq. (2.98). This damping is completely equivalent to that used to broaden the Dirac-Delta peaks in the calculation of the absorption in the frequency domain. Furthermore, we can calculate explicitly the electron motion under arbitrary time-dependent potentials, not necessarily weak. For instance, the time evolution of the system under quasi-monochromatic pulses and pump-probe laser fields is perfectly achievable. Time propagation is presently implemented in many codes, including ad-hoc programs aimed at evaluating the optical response of model jellium nanostructures [70, 77, 78]. In what follows we will use the Octopus package [185–188], which solves the KS

time-dependent equations in a real-space grid representation.

It is worth to note that besides the real-time TDDFT calculations of excited-state properties in molecules under the Yabana-Bertsch scheme [184], the code is able to perform many types of calculations of ground-state and excited-state properties. Although most of the capabilities of the code used throug this work were already implemented, other were to be implemented and/or improved. Next, we briefly mention some of the capabilities of the code required to carry out this Thesis.

2.3.1.1 Forces and the FIRE algorithm for geometry optimizations[9]

The precise determination of the geometrical structure that atoms do adopt on nanostructures is probably the first and most crucial step in their description and understanding. If not all, most methods to obtain stable structures are based on local minimizers. This local minimizers are algorithms adapted to identify the first minimum-energy structure starting from an arbitrary point on the coordinates space, which can be an informed guess or an arbitrary point in parameter space. The algorithm generates a serie of steps that ends when a stop criteria is reached with a determinated accuracy, such as when the gradient is near zero, or when the value of the energy function stops changing. A function represented on a real-space grid is not invariant under translations as one would expect from a physical system. The potential of an atom sitting on top of a grid point might be slightly different from the potential of the same atom located between points. This phenomenon is the so-called "egg-box effect". The egg-box effect is particularly problematic for calculations where the atoms are allowed to move, for example to study the dynamics of the atoms (molecular dynamics) or to find the minimum energy configuration (geometry optimization). Several schemes to control the egg-box effect in Octopus has been studied [189]. The first step is to use pseudo-potential filtering to eliminate Fourier components of the potential that cannot be represented on the grid [190]. Additionally, it has been found a formulation for the forces that reduces the spurious effect of the grid on the calculations. It mainly consist on rewrite the forces in such a way they do not include

[9]This subsection is based on part of the Ref. [188].

the derivative of the ionic potential v_α, but the gradient of the orbitals with respect to the electronic coordinates [191]. As the orbitals are smoother than the ionic potential, the calculation of the forces is more precise than the calculation of the energy when the system is discretized on a grid. As the fast inertial relaxation engine (FIRE) [192] algorithm to perform geometry optimizations rely only on the forces, without needing to evaluate the energy, and has become in one of the most convenient algorithm due to its speed and precision to reach the nearest local mini- mum starting from a given initial configuration [193] we implemented the FIRE algorithm in the Octopus code. The FIRE algorithm is based on molecular dynamics with additional velocity modifications and adaptive time steps which only requires first derivatives of the target function. In the FIRE algorithm, the system slides down the potential-energy surface, gathering "momentum" until the direction of the gradient changes, at which point it stops, resets the adaptive parameters, and resumes sliding. This gain of momentum is done through the modification of the time step Δt as adaptive parameter, and by introducing the following velocity modification

$$v(t) \to V(t) \quad = \quad (1-\alpha)v(t) + \alpha|v(t)|\hat{F}(t) \ , \tag{2.99}$$

where v is the velocity of the atoms, α is an adaptive parameter, and $\hat{F}$ is an unitary vector in the direction of the force F. By doing this velocity modification, the acceleration of the atoms is given by

$$\dot{v}(t) \quad = \quad \frac{F(t)}{m} - \frac{\alpha}{\Delta t}|v(t)|\left[\hat{v}(t) - \hat{F}(t)\right] \ , \tag{2.100}$$

where the second term is an introduced acceleration in a direction "steeper" than the usual direction of motion. Obviously, if $\alpha = 0$ then $V(t) = v(t)$, meaning the velocity modification vanishes, and the acceleration $\dot{v}(t) = F(t)/m$, as usual.

2.3.1.2 Forces and the TDDFT Ehrenfest Dynamics

With the exception geometry optimizations, in which the positions of the nuclei are crucial, for many calculations it is assumed that the dynamics of the nuclei that compose the system are not relevant. Simulations in this context are performed in a clamped ion approximation, where the ions are fixed and the electrons move in the fixed classical potential generated by them. This approximation is justified by the large nuclear mass, compared with the electronic one.

In real-time TDDFT, electron dynamics is described by the time-dependent Kohn-Sham equations given by Eqs. (2.75) to (2.77) [71, 74, 157]. Applying the Ehrenfest theorem to the ionic motion and assuming that ions can be approximated by point charges. The time-dependent equation for ions becomes

$$M_\alpha \frac{d^2}{dt^2} R_\alpha = -\nabla_{R_\alpha} \left(v_{\text{ion}-\text{ion}} + v_{\text{ion}-\text{elec}} + v_{\text{ext}} \right) , \tag{2.101}$$

where R_α and M_α correspond to the coordinates and mass of the α-th ion respectively. The first and second terms on the right-hand side of Eq. (2.101) are time-dependent forces due to ion-ion interactions and ion-electron interactions, respectively. The third term is the force from the external EM fields.

In particular, in this work, we performed calculations in order to study the mechanism of material removal of a target under the influence of a strong laser field. Thus, besides to perform TDDFT Ehrenfest dynamic calculations, it was necessary to extract separately the total, electronic, and ionic forces acting on each of the ion from the rest of system. This is, for each atom, we extracted the forces from the ions, from all electrons, as well as the combined force from both the remaining ions and all electrons separately. As this feature was not included on the Octopus code it was necessary to implement it.

Chapter 3

Theoretical analysis of the optical properties of mixed samples of $Cu_{2-x}S$ nanocrystals

3.1 Introduction

As we stated at the begining of this work (see Chapter 2) LSPs are collective and non-propagating oscillations (excitations) of conduction electrons around the surface of a metallic object that arise as a result of a resonant coupling with an external incident electromagnetic (EM) field. However, in the realm of semiconductor nanomaterials, a crystal lattice heavily doped with cation/anion vacancies or ionized atomic impurities is considered to be a general prerequisite to accommodating excess free carriers that can support localized surface plasmon resonances [8, 25, 30]. In this context and going beyond, it has been recently denmostrated that anisotropic copper sulfide nano-crystals, selectively trapped in the covellite phase, can exhibit intense and size-tunable LSPR at near-infrared wavelengths despite their stoichiometric, undoped structure [37], where experimental extinction spectra were satisfactorily reproduced by theoretical calculations performed by the discrete dipole approximation (DDA) method within the framework of

the Drude-Sommerfeld model.

Following these recent results on the stoichiometric CuS (covellite) disk-like nanocrystals reported by Xie *et.al.* [37], experimental NIR spectra of nonstoichiometric mixed-phase samples were rationalized on the basis of electrodynamic scattering simulations performed within the frame of the discrete dipole approximation (DDA) [201]. This method allows to compute scattering and absorption cross-sections of targets of arbitrary geometry by solving the relevant Maxwell's equations. Namely, the target is treated as a finite array of interacting and polarizable points, which acquire dipole moments in response to a local electric field produced by the incident light and by the electric filed generated by the other dipoles. The polarizabilities of the dipoles are described by the effective bulk dielectric function $\varepsilon(\omega)$ of the target.

3.2 DDA fitting of the experimental spectra

3.2.1 Methodology

Thus, electromagnetic scattering calculations were performed within the frame of the discrete dipole approximation method [201] using the Amsterdam DDA code [202]. The interdipole distance used in all the calculations was 0.25 nm, and we considered orientation averaging of different incident polarized plane waves.

To extract the parameters of the Drude, and Drude-Lorentz models associated with the different phases and samples, the experimental extinction cross sections $\sigma_S^{\mathrm{exp}}(\lambda_i)$, relative to NDs, dissolved in $CHCl_3$ were fitted to the computed ones $\sigma_S^{\mathrm{DDA}}(\lambda_i)$. For each sample ($S$), we computed the relative difference ($\Delta\sigma_S$ between the DDA-calculated and experimental normalized cross-section through the following function:

$$\Delta\sigma_S = \frac{1}{N}\sum_{i=1}^{N}\left|\frac{\sigma_S^{\mathrm{DDA}}(\lambda_i)}{\max[\sigma_S^{\mathrm{DDA}}]} - \frac{\sigma_S^{\mathrm{exp}}(\lambda_i)}{\max[\sigma_S^{\mathrm{exp}}]}\right|, \tag{3.1}$$

where

$$\sigma_S^{\mathrm{DDA}} = \sum_l \left\{ \sigma_l^{\mathrm{DDA}} \times W_l \right\} \ , \tag{3.2}$$

where, l stand for the different phases of the sample, W_l correspond to the weight of each phase, λ_i ranged from 600 to 2100 nm in steps of 50 nm, (thus, originally $N = 31$, but we skipped the values corrensponding to 1650 and 1700 nm, due to the noise on the experimental spectra, so at the end $N = 29$) and the extinction spectra were taken normalized to the corresponding extinction band maxima, $\max[\sigma_S^{\mathrm{DDA}}]$ and $\max[\sigma_S^{\mathrm{exp}}]$.

First, we minimized $\Delta\sigma_S$ for the covellite sample. The experimental data were fitted through a three-dimensional scan of the Drude parameters, as follows: ω_p was varied from 4.3 to 4.7 eV in steps of 0.2 eV; ε_∞ was varied from 7 to 11 in steps of 2; and γ was varied from 0.10 to 0.90 eV in steps of 0.05 eV. This served to assess and confirm the findings by Xie *et al* about the covellite.

Finally, we minimized the absolute difference $\Delta\sigma$ considering all the phases/samples simultaneously, that is, we minimized the following function

$$\Delta\sigma = \frac{1}{4} \sum_S \Delta\sigma_S \ . \tag{3.3}$$

Only ε_∞, and ω_p for the covellite phase were fixed during the calculations. The other parameters were varies as follows: ε_∞ was varied from 1 to 11 in steps of 2; ω_p was varied from 1.0 to 4.5 eV in steps of 0.2 eV: γ was varied from 0.1 to 0.9 eV in steps of 0.05 eV; $\Delta\varepsilon$ was varied from 0 to 1.0 in steps of 0.1; ω_L was varied from 0.2 to 2.0 eV in steps of 0.2 eV; and γ_L was varied from 0.1 to 0.9 in steps of 0.05 eV.

The DDA extinction scattering cross-sections of four mixed-phase samples of nanodisks (NDs) disolved in $CHCl_3$ (refractive index 1.4459) were computed. Depending on the sample, variable crystal-phase compositions, with covellite (CuS), digenite ($Cu_{1.8}S$), and low-chalcocite (Cu_2S), each one characterized by a different stoichiometry and structure,

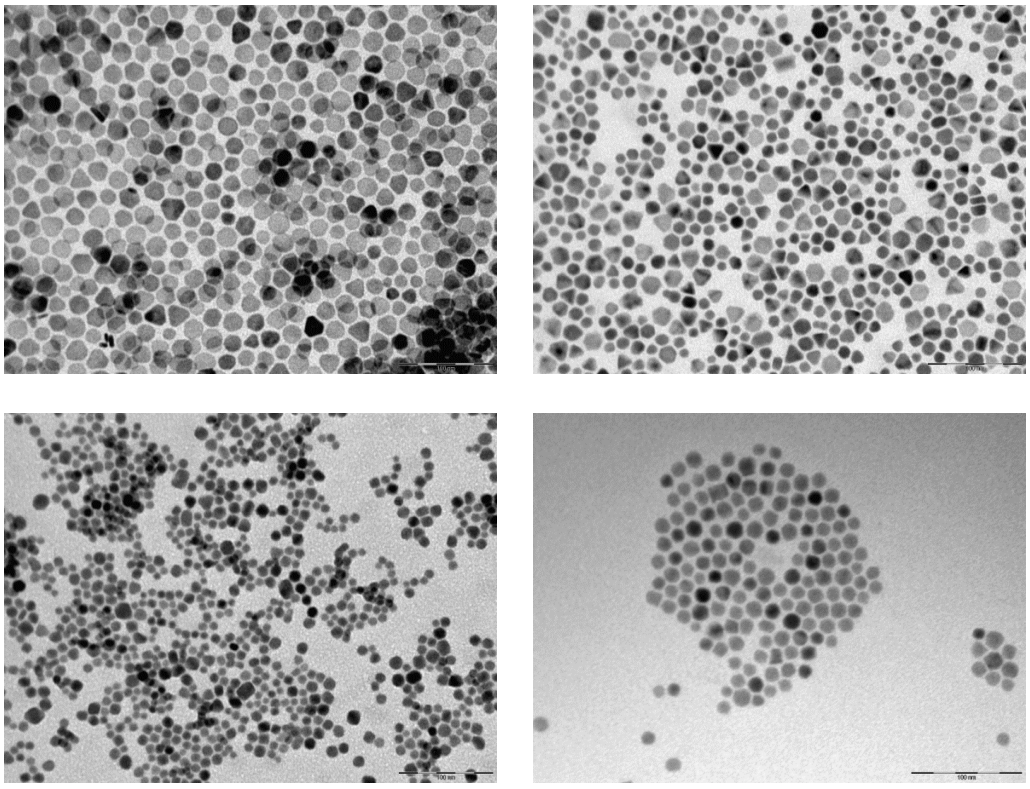

Figure 3.1: Representative low-magnification TEM image galleries of $Cu_{2-x}S$ mixed-phase samples. The relative weight percentages of the different phases are determined by XRD analyses.

are present in different relative weight proportions. The mixed-phase samples were treated as weighted mixtures of identical size and shape NDs, each one characterized by a different dielectric function. The low-magnification TEM images of the mixed-phase samples are shown in Fig 3.1, and details of each sample are displayed on Table 3.1.

$\overline{D}$ (nm)	$\overline{H}$ (nm)	Shape	Relative weight percentages (%)		
			CuS	$Cu_{1.8}S$	Cu_2S
20	5	hexagon	100	0	0
15	7	cylinder	73	27	0
11	7	cylinder	10	73	17
18	8	cylinder	10	86	4

Table 3.1: Morphology of the modeled NDs, and phase-composition of each sample.

As shown recently by Xie *et al* [37], the experimental electromagnetic response properties of stoichiometric copper sulfide (CuS) nanocrystals can be explained under the DDA framework by considering the complex Drude dielectric function. That is, the electromagnetic response of covellite nanocrystals is dominated by collective excitations of

free-carriers, and excellent agreement with experimental data is achieved by taking the values $\varepsilon_\infty = 9$ and $\omega_p = 4.5$ eV. However, recent works have highlighted that the modeling of the bulk dielectric function for nonstoichiometric $Cu_{2-x}S$ phases on the basis of the Drude model, which describes a system of free carriers in a crystal, may not be the most suitable [41], as the carriers supporting the plasmon resonance can experience a certain degree of localization. As it was stated in Chapter 2, one proposed way to overcome this limitation of the Drude model, is to add one or several Lorentzian terms to the Drude dielectric function, in order to take into account localized carriers or interband transitions [41, 203]. This approach, usually known in the literature as Drude-Lorentz model, has been used in previous studies with slight modifications depending on the specific cases [41, 203, 204]. Therefore, we have used the Drude-Lorentz dielectric function (Eq. 2.48) to model spectra of these nonstoichiometric mixed-phase nanostructures.

Our aim was to extract the best set of parameters of the corresponding models, for the whole set of samples, by fitting their experimental spectra. To do so, the relative difference ($\Delta\sigma_S$) for each sample, and the absolute difference ($\Delta\sigma$), considering all the samples simultaneously, between the DDA-calculated and experimental normalized cross-section was minimized through a multi-dimensional scan of the Drude (covellite) and the Drude-Lorentz (digenite and low-chalcocite) parameters. However, when considering all the samples, the best agreement between ($\Delta\sigma$) the DDA-calculated and experimental spectra was found for $\Delta\varepsilon = 0$ for the digenite, and low-chalcocite phases, correspondig to the Drude-only model. This best agreement (absolute minimum, $\Delta\sigma = 2.56\%$) between DDA-calculated and experimental spectra was found for $\varepsilon_\infty = 9$, and $\omega_p = 4.5$ eV for the covellite; $\varepsilon_\infty = 7$, and $\omega_p = 3.8$ eV for the digenite; and $\varepsilon_\infty = 7$, and $\omega_p = 2.2$ eV for the low-chalcocite phase.

For the first sample, the best agreement ($\Delta\sigma_S = 2.92\%$) between DDA-calculated and experimental spectra is found for $\varepsilon_\infty = 9$, $\omega_p = 4.5$ eV, and $\gamma = 0.30$ eV, thus confirming the previously value of the plasma frequency of the covellite by Xie *et al* [37]. The optimized computed optical spectrum for this sample is displayed on Fig. 3.2 together with the experimental one. For the sake of completeness, we also depict the in-plane

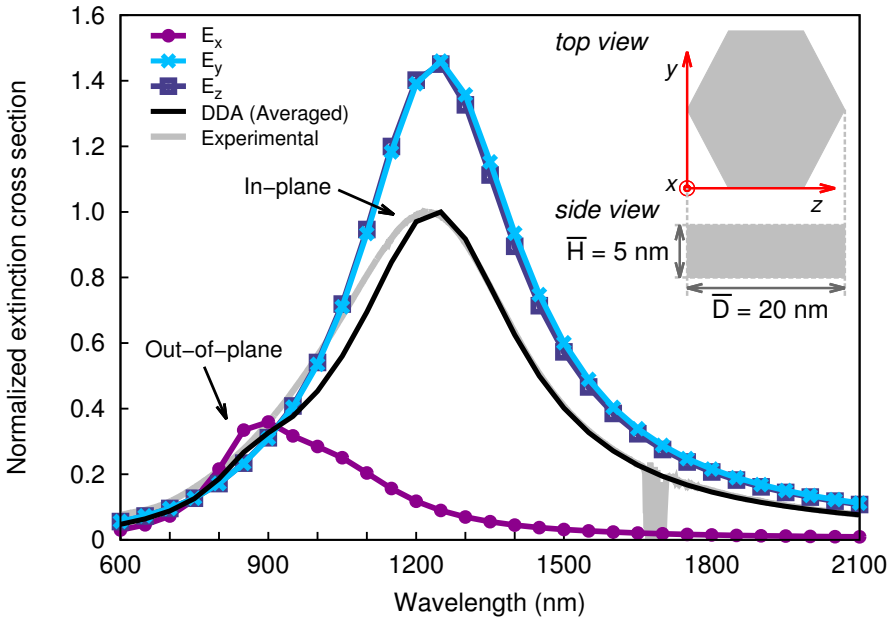

Figure 3.2: Experimental (solid grey line) and theoretical DDA (solid black line) extiction cross-sections of a covellite hexagonal ND ($\overline{\mathrm{H}} = 5$ nm, $\overline{\mathrm{D}} = 20$ nm). The DDA spectra for incident light polarized along the out-of-plane (x) and in-plane axis directions (y, z) are included as well.

(electric field perpendicular to the ND axis) and out-of-plane (electric field parallel to the ND axis) DDA responses. As we may see, the spectrum is dominated by an in-plane localized surface plasmon resonance (LSPR) in the near infrared (NIR) range. The DDA calculation reveals a weaker but recognizable contribution from the out-of-plane LSPR at higher energy due to the large aspect ratio ($\overline{\mathrm{D}}/\overline{\mathrm{H}} = 4$) of the NDs. However, this spectral feature is not resolved in the experimental spectrum as it lies, precisely, in the region where the agreement between theory and experiment is worst. Since the relative allocation of the in- and out-of-plane resonances depends very sensitively on the shape of the NDs, we believe that the small discrepancies between the DDA prediction and the experimental spectrum are due to the presence of geometrically-different disks in the sample.

Concerning the second sample (73% covellite, 27% digenite), the set of parameters which minimize the relative difference ($\Delta\sigma_S = 5.14\%$) are given in Table 3.3, and the experimental and optimized computed spectra are displayed in Fig. 3.3. In particular, the obtained value of $\omega_p = 3.8$ eV of the digenite phase corresponds to $N_h \approx 0.70 \times 10^{22}$ cm^{-3} (*i.e.*, $\sim$ 0.24 holes per $Cu_{1.8}S$ molecular unit), which still approaches the free carrier concentration

	Covellite	Digenite	Low-chalcocite	Mixed
Relative weight percentages (%)	100	0	0	-
Dielectric function	Drude	-	-	-
ε_∞	$9^{(b)}$	-	-	-
ω_p (eV)	$4.5^{(b)}$	-	-	-
γ (eV)	0.30	-	-	-
$\lambda_{\max}^{\exp}$ (nm)	1218	-	-	1218
$\lambda_{\max}^{\mathrm{DDA}}$ (nm)	1150	-	-	1250
$\lambda_{\mathrm{in}}^{\mathrm{DDA}}$ (nm)	1250	-	-	1250
$\lambda_{\mathrm{out}}^{\mathrm{DDA}}$ (nm)	900	-	-	900

Table 3.2: Parameters featuring the steady state NIR extinction of the covellite sampe ND, deduced on the basis of DDA-based calculations, and fits of experimental spectra.

typical of several metals [205–210]. Thus, the CuS NDs were found to accomodate a free hole density 1.4 times higher than the deduced for the $Cu_{1.8}S$ nanocrystals. In this regard, as stated by Xie *et al* [37], it is worth to note that previous estimations of N_h in $Cu_{2-x}S$ nanocrystals with $1.93 < 2-x < 2$, where 0.77×10^{21} cm$^{-3} \lesssim N_h \lesssim 1.36 \times 10^{21}$ cm^{-3} [39], are likely to be imprecise, as the assumed models fails to account for the partially localized character of hole carriers sustaining LPRS in those nonstoichiometric materials.

The aspect ratio of the NDs comprising this second sample is rather small, thus explaining the impossibility to clearly differenciate in- and out-of-plane contributions in the spectra (see Fig. 3.3). The decomposition of the optimized DDA spectra of each phase, according to the polarization of the incident light is presented in Fig. 3.4. As a second conclusion, our DDA calculations indicate that the overall shape of the experimental optical absorption curve is due to a convollution of two peaks, one corresponding to a LSPR ocurring at covellite NDs and a second one, at lower energies, that can be attributed to a collective excitation at digenite NDs. Note in passing that the smaller aspect ratio implies that the experimental results are less sensitive to the shape-dispersion of the NDs in the sample, thus allowing for a better fit of the calculated-DDA absorption.

Finally, for the two non-stoichiometric three-mixed-phase samples (10% covellite, 73% digenite, 17% low-chalcocite; and 10% covellite, 86% digenite, 4% low-chalcocite), the best set of parameters which minimize the relative difference $\Delta\sigma$ between DDA-calculated and

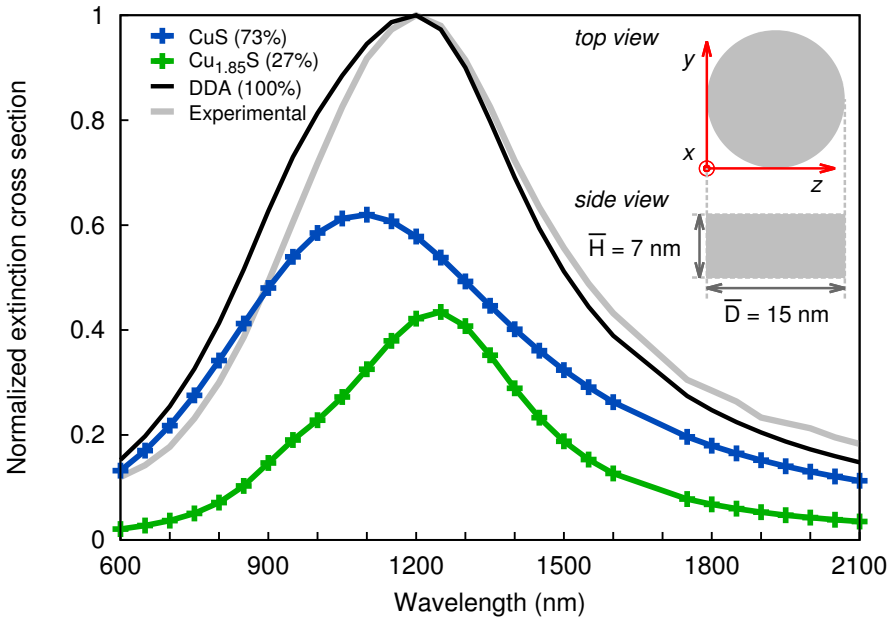

Figure 3.3: Normalized experimental NIR extinction espectra (solid grey line) of the two-mixed-phase sample ND, along with the corresponding normalized DDA-based fits (solid black line). The relative contributions of the covellite (blue line with symbols) and the digenite (green line with symbols) are also depicted.

	Covellite	Digenite	Low-chalcocite	Mixed
Relative weight percentages (%)	73	27	0	-
Dielectric function	Drude	Drude[a]	-	-
ε_∞	9[b]	7	-	-
ω_p (eV)	4.5[b]	3.8	-	-
γ (eV)	0.70	0.30	-	-
$\lambda_{\max}^{\exp}$ (nm)	-	-	-	1135
$\lambda_{\max}^{\mathrm{DDA}}$ (nm)	1000	1250	-	1150
$\lambda_{\mathrm{in}}^{\mathrm{DDA}}$ (nm)	1100	1250	-	1200
$\lambda_{\mathrm{out}}^{\mathrm{DDA}}$ (nm)	950	1100	-	1000

Table 3.3: Parameters featuring the steady state NIR extinction of the two-mixed-phase sampe ND, deduced on the basis of DDA-based calculations, and fits of experimental spectra. [a]The best agreement was found for $\Delta\varepsilon = 0$ on the Drude-Lorentz model, which correnpond to the Drude-only model. [b]This parameters were fixed on the global minimization of $\Delta\sigma$.

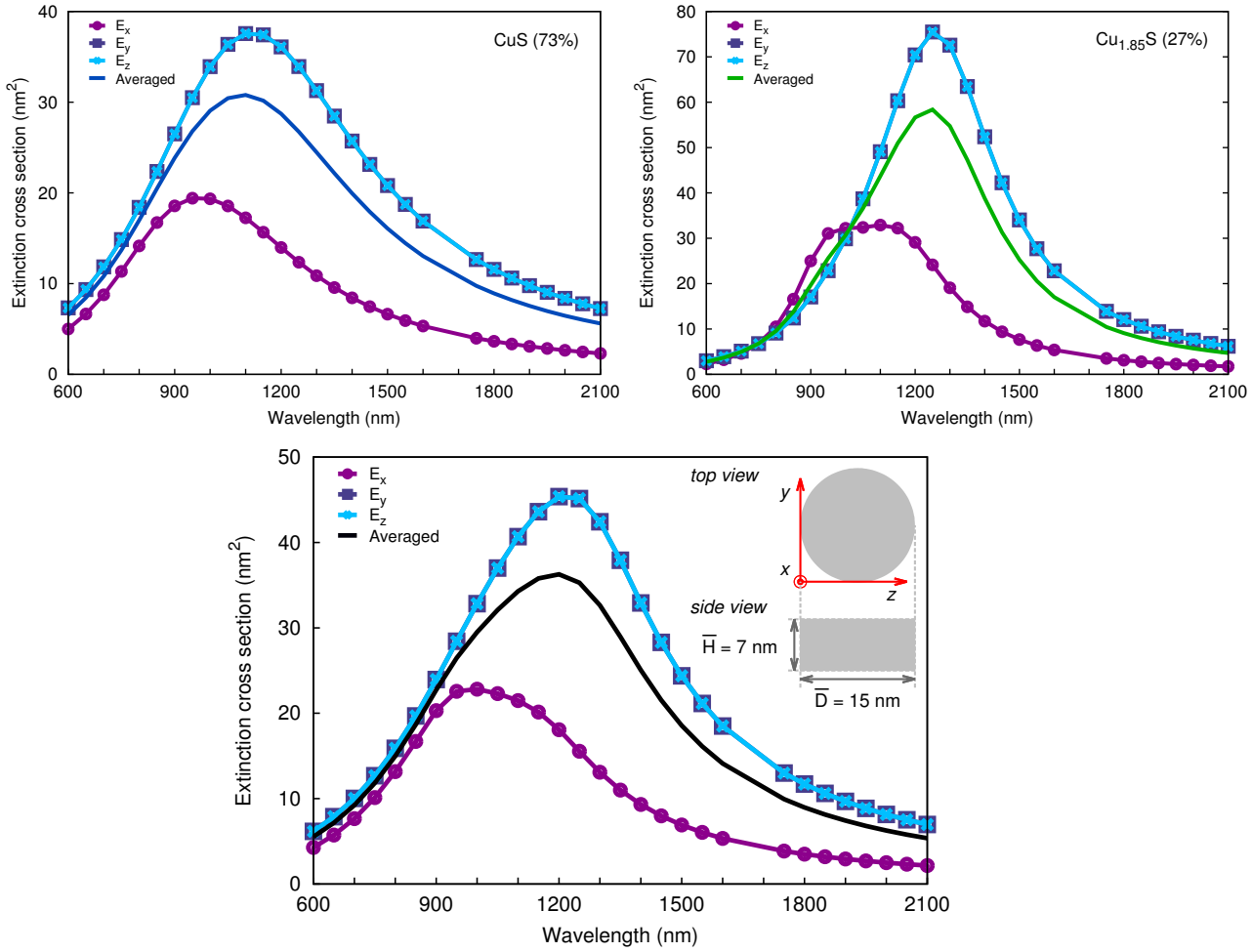

Figure 3.4: DDA extinction cross sections of the two-mixed-phase NDs along with their total in-plane and out-of-plane contributions. The two upper panels correspond to the unweighted cross sections of each phases, whereas the lower panel represents the corresponding averages. Note that the different contributions by each phase are easier to observe in the spectrum corresponding to polarized incident light than in the spectrum associated to unpolarized light.

	Covellite	Digenite	Low-chalcocite	Mixed
Relative weight percentages (%)	10	73	17	-
Dielectric function	Drude	Drude[(a)]	Drude[(a)]	-
ε_∞	9[(b)]	7	7	-
ω_p (eV)	4.5[(b)]	3.8	2.2	-
γ (eV)	0.40	0.60	0.50	-
$\lambda_{\max}^{\exp}$ (nm)	-	-	-	1137
$\lambda_{\max}^{\mathrm{DDA}}$ (nm)	1100	1150	2000	1150
$\lambda_{\mathrm{in}}^{\mathrm{DDA}}$ (nm)	1100	1200	2050	1150
$\lambda_{\mathrm{out}}^{\mathrm{DDA}}$ (nm)	1050	1100	1900	1100

Table 3.4: Parameters featuring the steady state NIR extinction of the three-mixed-phase (10% covellite, 73% digenite, and 17% low-chalcocite) sample ND, deduced on the basis of DDA-based calculations, and fits of experimental spectra. [(a)]The best agreement was found for $\Delta\varepsilon = 0$ on the Drude-Lorentz model, which correnpond to the Drude-only model. [(b)]This parameters were fixed on the global minimization of $\Delta\sigma$.

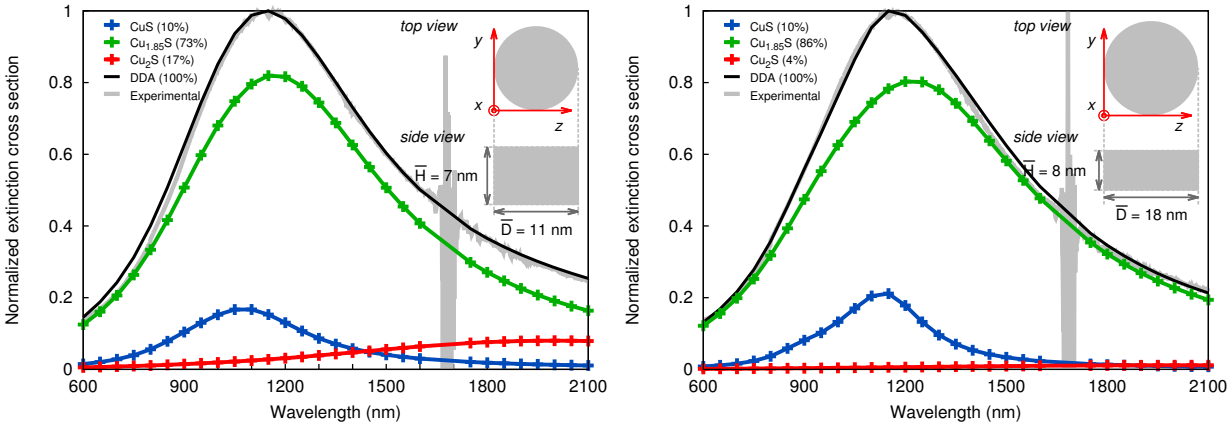

Figure 3.5: Normalized experimental and theoretical NIR extinction espectra of the three-mixed-phase samples. Note the small contributions from the low-chalcocite phase (red line with symbols).

experimental spectra are given in Table 3.4, and Table 3.5 respectively. The experimental and optimized computed spectra for this two samples are displayed in Fig. 3.5. In both cases, the agreement with the experimental data is excellent, being the relative errors of the fitting $\Delta\sigma_S = 0.99\%$ and $\Delta\sigma_S = 1.20\%$ for the third and forth samples, respectively.

The Drude plasma frequency of the low-chalcocite phase corresponds to $N_h = 0.19 \times 10^{22}$ cm^{-3} (*i.e.*, ~ 0.04 holes per Cu_2S molecular unit), which still (around the limit) could be considered on the domain of the carrier densities of semiconductors [30].

	Covellite	Digenite	Low-chalcocite	Mixed
Relative weight percentages (%)	10	86	4	-
Dielectric function	Drude	Drude[(a)]	Drude[(a)]	-
ε_∞	9[(b)]	7	7	-
ω_p (eV)	4.5[(b)]	3.8	2.2	-
γ (eV)	0.25	0.60	0.70	-
$\lambda_{\max}^{\exp}$ (nm)	-	-	-	1135
$\lambda_{\max}^{\mathrm{DDA}}$ (nm)	1150	1200	2050	1150
$\lambda_{\mathrm{in}}^{\mathrm{DDA}}$ (nm)	1150	1250	2100[(c)]	1200
$\lambda_{\mathrm{out}}^{\mathrm{DDA}}$ (nm)	1100	1050	1750	1000

Table 3.5: Parameters featuring the steady state NIR extinction of the three-mixed-phase (10% covellite, 86% digenite, and 4% low-chalcocite) sample ND, deduced on the basis of DDA-based calculations, and fits of experimental spectra. [(a)]The best agreement was found for $\Delta\varepsilon = 0$ on the Drude-Lorentz model, which correnpond to the Drude-only model. [(b)]This parameters were fixed on the global minimization of $\Delta\sigma$. [(c)]This parameter in on the upper limit of the range of wavelengths we simulated.

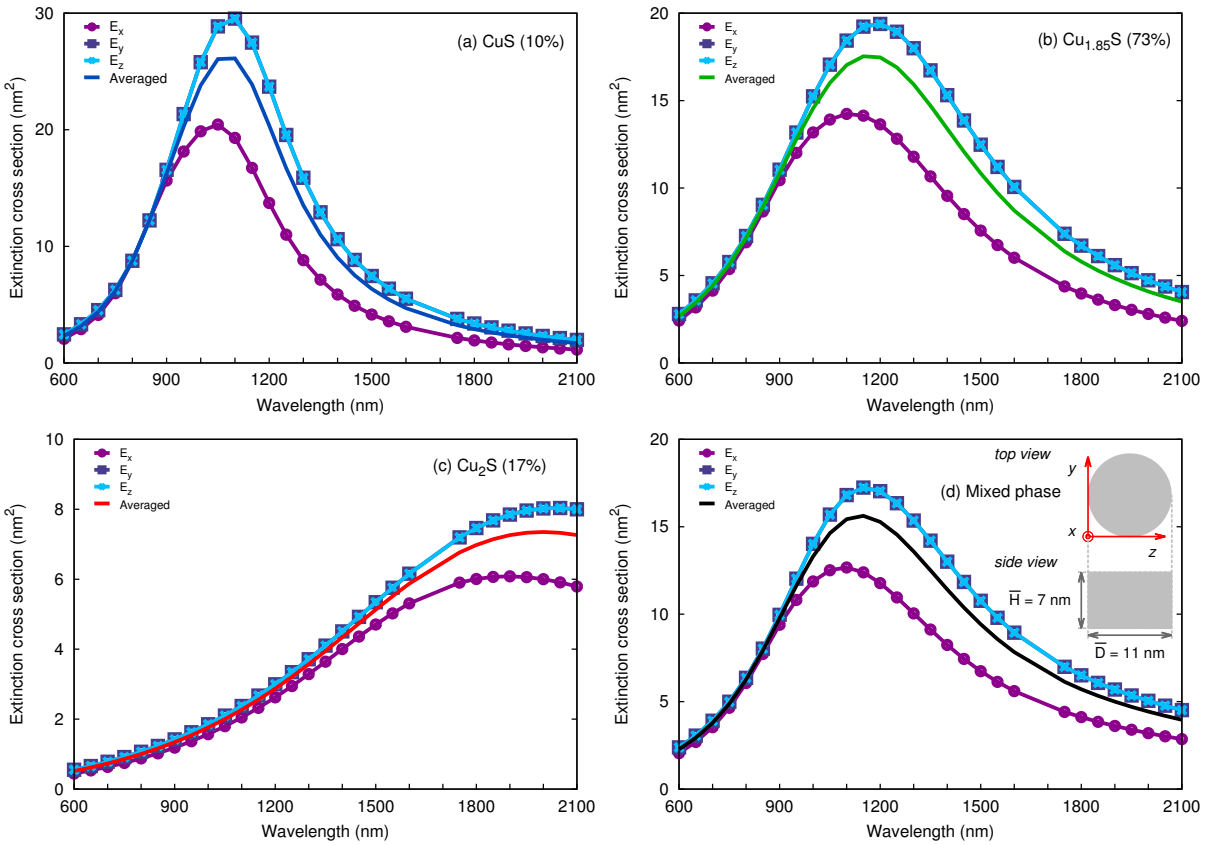

Figure 3.6: DDA extinction cross sections of three-mixed-phase NDs (10% covellite, 73% digenite, and 17% low-chalcocite) along with their total in-plane and out-of-plane contributions. Panels (a), (b), and (c) correspond to the unweighted cross sections of each phase, whereas panel (d) represents the corresponding averages on the mixed-phase sample.

3.2.2 Decomposition of the optical response

Regarding the decomposition of the optical response in LSPRs excited by in-plane and out-of-plane polarized incident light, the aspect ratio of the third sample is equal to 1.57, therefore, the in-plane and out-of-plane responses are expected to be rather similar. This is indeed the case as can be observed in Fig. 3.6. Finally, the larger aspect ratio of the NDs of the forth sample ($\overline{\mathrm{D}}/\overline{\mathrm{H}} = 2.25$) leads to different resonant frequencies for the in-plane and out-of-plane LSPRs of the covellite, digenite, and low-chalcocite phases (see Fig. 3.7). Nevertheless, all contributions can be hardly discriminated in the averaged spectrum, which is dominated by in-plane dipolar LSPRs. As a conclusion, despite the rather small aspect ratio of the mixed-phase samples, a careful theoretical analysis of the absorption spectra clearly demonstrates the shape-dependence of the LSPRs in the plasmonic covellite, digenite, and low chalcocite phases. This further supports the interpretation of the already mentioned experimental findings by Xie *et al* in covellite NDs [37] and also the reported experiments by Hsu *et al* for $Cu_{2-x}S$ NDs [39, 42].

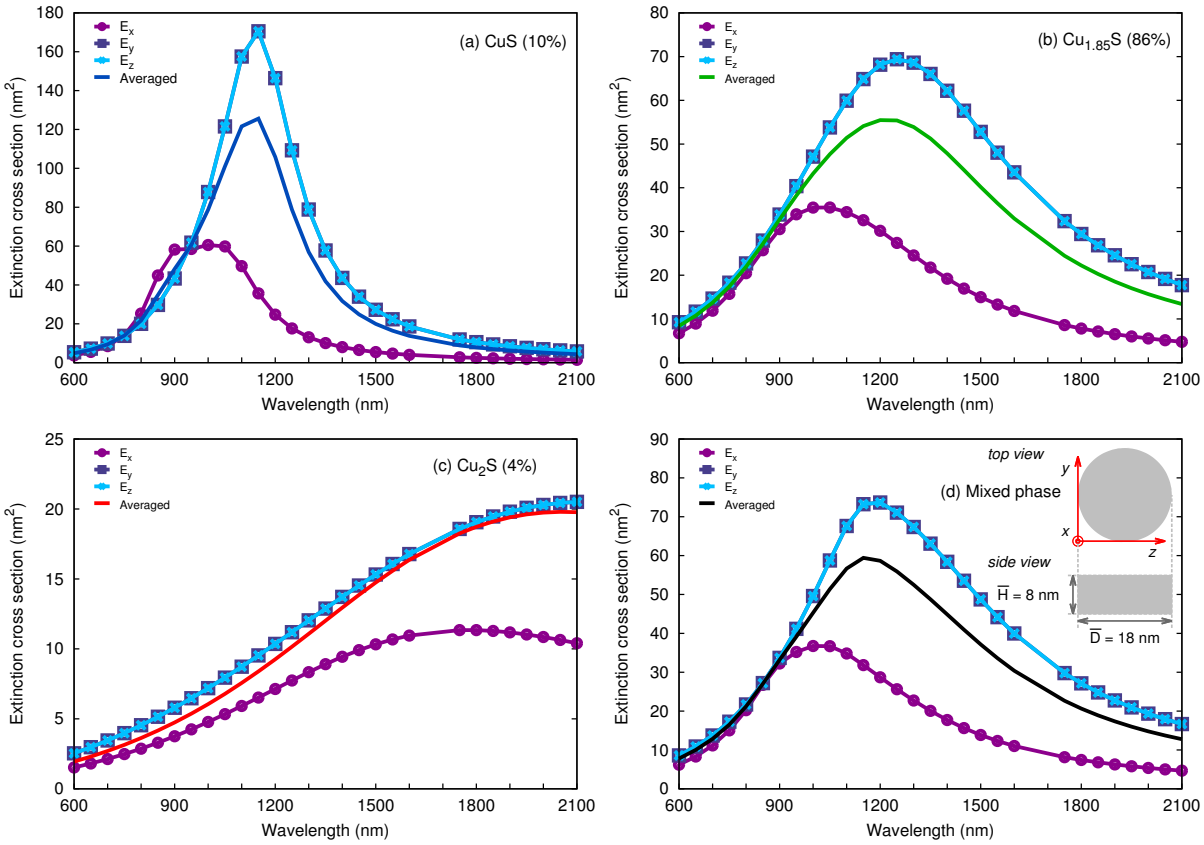

Figure 3.7: DDA extinction cross sections of three-mixed-phase NDs (10% covellite, 86% digenite, and 4% low-chalcocite) along with their total in-plane and out-of-plane contributions. Panels (a), (b), and (c) correspond to the unweighted cross sections of each phase, whereas panel (d) represents the corresponding averages on the mixed-phase sample.

Chapter 4

Theoretical analysis of the optical properties of $WO_{3-\delta}$ hemitubes

4.1 Introduction

As we already know (see chapter 1), doped semiconductor nanostructures are capable of supporting LSPRs [31]. The highly variable carrier density of doped semiconductor nanocrystals, enables a variable resonance frequency over the entire infrared region [30, 33, 211]. Then, varying the doping level by controlling the concentration of vacancies it is possible to tune the resonance frequency of these nanocrystals [30, 36, 39, 40, 212, 213].

In the case of $WO_{3-\delta}$, a variety of oxygen-deficient stoichiometries can be obtained, leading to some contradictory results, ranging from $WO_{2.72}$ ($W_{18}O_{49}$) nanowires which appear to be semiconducting on the basis of electrical transport and photoluminescence studies [44, 45], to $W0_{2.8}$ (W_5O_{14}) nanowires which appear to be metallic on the basis of XPS and electrical transport measurements [46]. It has been also recently shown that nanoscale $WO_{2.83}$ ($W_{24}O_{68}$) nanorods support strong LSPRs and that these LSPRs account for a strong absorption feature ranging from the red edge of the visible to the NIR region [36].

On the other hand, unlike classical metal nanoparticles, there is a controversy on how LSPRs in doped semiconductor nanocrystals are sensitive to anisotropic nanoparticle

shape [214,215]. In this context, faceted octahedral indium-doped cadmium oxide nanocrystals have shown multiband LSPR that were well matched by simulated spectra computed in the framework of the DDA method, in which multipolar spatial modes contributed to the line shape [215,216], whereas despite their anisotropic morphologies $WO_{3-\delta}$ nanorods and $Cu_{2-x}Te$ platelets, rods, and tetrapods have not shown LSPR band-splitting [36,41]. Furthermore, in-plane and out-of-plane modes with shifts with changing the aspect ratio of $Cu_{2-x}S$ nanodisks were observed [42]. Meanwhile, only an in-plane resonant peak red-shift was observed with increasing the diameter of CuS nanoplatelets [214].

Considering the above, and with the extra motivation of recently synthesized nonstoichiometric $WO_{3-\delta}$ (mainly $WO_{2.72}$) nanocrystals of hemitubular morphology by a collaborating research group, in this chapter, we have performed classical and semiclassical calculations, within the frame of the DDA and finite element method with the aim of sheed light on the unique structural-optical properties, of these novel nanostructures, which experimentally show tunable NIR to mid-IR plasmon resonances, essentially dependent on their aspect ratio.

4.2 Hemitube morphology and experimental data

A direct template-free, solution-phase synthesis of plasmonic nonstochiometric $WO_{3-\delta}$ hemi-nanotubes was recently developed by a collaborating research group. These exotic nanocrystals show tunable NIR to mid-IR plasmon resonances, essentially dependent on their aspect ratio.

4.3 Theoretical analysis of the experimental data

In order to make a theoretical analysis of the experimental data, the frequency-dependent $WO_{2.72}$ bulk dielectric function $\varepsilon(\omega)$ is required. Of course, $\varepsilon(\omega)$ might be obtained from a parametrization of different experimental data, as it is customary done in nanoplas-

Lenght L (nm)	Wall thickness a (nm)	Internal diameter b (nm)	Overall diameter c (nm)
16.5 ± 4.2	2.0 ± 1.0	2.0 ± 1.0	5.0 ± 0.5
10.8 ± 3.6	2.0 ± 1.0	2.0 ± 1.0	8.5 ± 0.6
17.9 ± 3.1	2.0 ± 1.0	2.0 ± 1.0	8.0 ± 1.5
59.9 ± 18.7	2.0 ± 1.0	2.0 ± 1.0	6.4 ± 0.6
39.6 ± 7.4	2.0 ± 1.0	2.0 ± 1.0	6.3 ± 1.3
78.4 ± 21.9	2.0 ± 1.0	2.0 ± 1.0	6.5 ± 1.2
62.1 ± 10.7	2.0 ± 1.0	2.0 ± 1.0	8.0 ± 1.0
56.4 ± 14.5	2.0 ± 1.0	2.0 ± 1.0	8.5 ± 1.1

Table 4.1: Morphology of the different $WO_{3-\delta}$ hemitubes.

monics [4]. Unfortunately, to the best of our knowledge the experimental determination of the optical absorption of different bulk-$WO_{3-\delta}$ compounds is still lacking. However, since our primary interest is the analysis of the plasmonic response of $WO_{2.72}$ hemitubes, a qualitative approach to the actual $\varepsilon(\omega)$ can be made from general considerations as follows.

$WO_{3-\delta}$ compounds result from the reduction of WO_3 which, up to quantitative details depending on the phase, is a semiconductor with optical gap $\Delta_g \sim 2.7$ eV [217–219]. The WO_3 valence band consists of oxygen 2p states whereas the bottom of the conduction band arises from unoccupied tungsten 5d states, likely exhibiting a slight hybridization [220, 221]. Hence, the WO_3 optical absorption is governed by interband transitions and its dielectric function mainly consists of a sum of Lorentzians. As anticipated, there are not fully reliable reflectivity measurements providing the whole absorption $\mathrm{Im}\,\varepsilon(\omega)$, but some estimations were already proposed long ago [217] and ab-initio calculations using the many-body Bethe-Salpeter equation [72] have been recently reported [222]. Since we are interested on optical properties at low frequencies, it is legitimate to model the WO_3 dielectric function as a single Lorentzian plus a constant ε_∞ that aims at describing the actual $\omega \to \infty$ limit of the dielectric function ($\varepsilon_\infty \sim 4$) [222, 223], the low-frequency average of the real part of further Lorentzian terms, and possible ionic-background contributions:

$$\varepsilon_L(\omega) = \varepsilon_\infty - \frac{f_L \Omega_L^2}{\omega^2 - \Omega_L^2 + i\omega\gamma_L} \ . \tag{4.1}$$

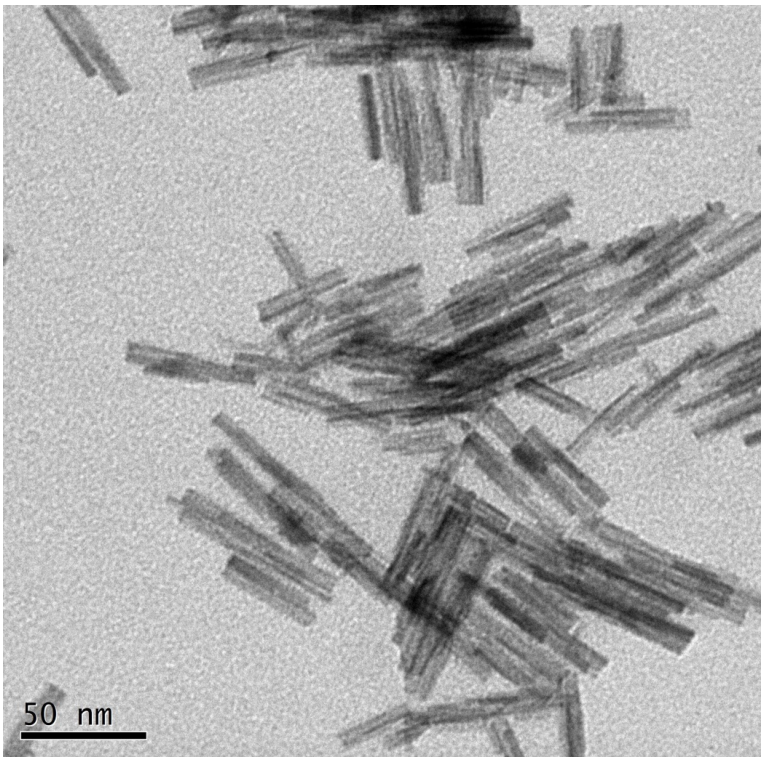

Figure 4.1: Representative low-magnification TEM image of $WO_{3-\delta}$ hemitubes.

Here, Ω_L is the excitation frequency, f_L is the oscillator strength, and γ_L is a damping frequency that accounts for the finite width of the Lorentizian peak. It is worth to note that Eq. 4.1 is a particular case of Eq. 2.45. From the calculations in Ref. [222] we have that $\Omega_L \simeq 4.1$ eV, $\gamma_L \simeq 0.5$ eV, and $f_L \simeq 2$ is a reasonable choice. Estimations based on EELS experiments on WO_3 thin films Ref. [217] suggest slightly different values. In any case, for our purposes the most relevant quantity is the static limit $\varepsilon_L(\omega \to 0)$ since, as we will see later on, the optical response below 2 eV is quite robust against variations of Ω_L and γ_L.

Upon reduction of pure WO_3 samples extra electron states start to appear at the bottom edge of the conduction band, a process accompanied by a shift of the Fermi level, subtle structural reconstructions, and a redistribution of the density of states (thus, some tungsten 5d states could now be present below the Fermi level) [4, 5]. A fully detailed understanding of the whole mechanism has not been achieved yet, but the main trends are now well established [220,221,224–228]. First of all, $WO_{3-\delta}$ is still semiconductor for small number of oxygen vacancies ($\delta \lesssim 0.1$), and the vacancy-induced electron states explains

the blue coloration exhibited by $WO_{3-\delta}$ compounds [218,219] as well as the appearance of low-frequency bulk plasmons in thin metal films [217]. However, $WO_{3-\delta}$ becomes metallic at $\delta \sim 0.1$ and, as a consequence, a strong plasmonic response appears in the near IR region for $WO_{3-\delta}$ nanosheets [229] and for $WO_{2.82}$ nanorods [36]. The Lorentz-like absorption peak is expected to remain regardless the density of oxygen vacancies, as observed in the UV-vis photoluminescence spectrum of $WO_{2.72}$ nanobundles [45].

Bearing all this in mind, it is legitimate to model the $WO_{3-\delta}$ ($\delta \gtrsim 0.1$) dielectric function as the sum of a Drude term, describing the reduction-induced free carriers, and a Lorentz dielectric function, which is expected to be rather similar than the WO_3 one given in Eq. 4.1 and has the same form of Eq 2.48. That is:

$$\varepsilon_L(\omega) = \varepsilon_\infty - \frac{\omega_p^2}{\omega(\omega + i\gamma_D)} - \frac{f_L \Omega_L^2}{\omega^2 - \Omega_L^2 + i\omega\gamma_L} \ , \tag{4.2}$$

where ε_∞ contains in an averaged manner further optical-response mechanisms (extra interband transitions, ionic contributions, etc.), but should not be very different than the reference value $\varepsilon_\infty \sim 4$ corresponding to pristine tungsten trioxide. Then, the bulk-plasmon frequency $\varepsilon(\omega)$, the damping frequency γ_D, and ε_∞ must be regarded as δ-dependent parameters, although will also depend on the specific geometry of the nanostructure [20], as explained in chapter 2. In this way, the vis-IR optical absorption is dominated by free-carriers LSPs, whereas the absorption below $\lambda \sim 450$ nm (2.75 eV) corresponds to interband transitions.

Thus, the parameters ω_P, γ_D, and ε_∞ corresponding to $WO_{2.72}$ can be estimated from the present experimental data. First, surface scattering effects are expected to be almost negligible for the axial modes (note that the length of the hemitubes is of the order of tens of nanometers). Hence, from the experimental FWHM of the main plasmonic peaks for the longest hemitubes we have that the bulk (intrinsic) contribution to the damping frequency γ_D is $\gamma_{bulk} \sim 0.9$ eV, which, as just mentioned, is a good approximation to the Drude damping frequency for axial response.

Second, ω_p and ε_∞ are obtained from a semi-analytical approach to the optical absorption

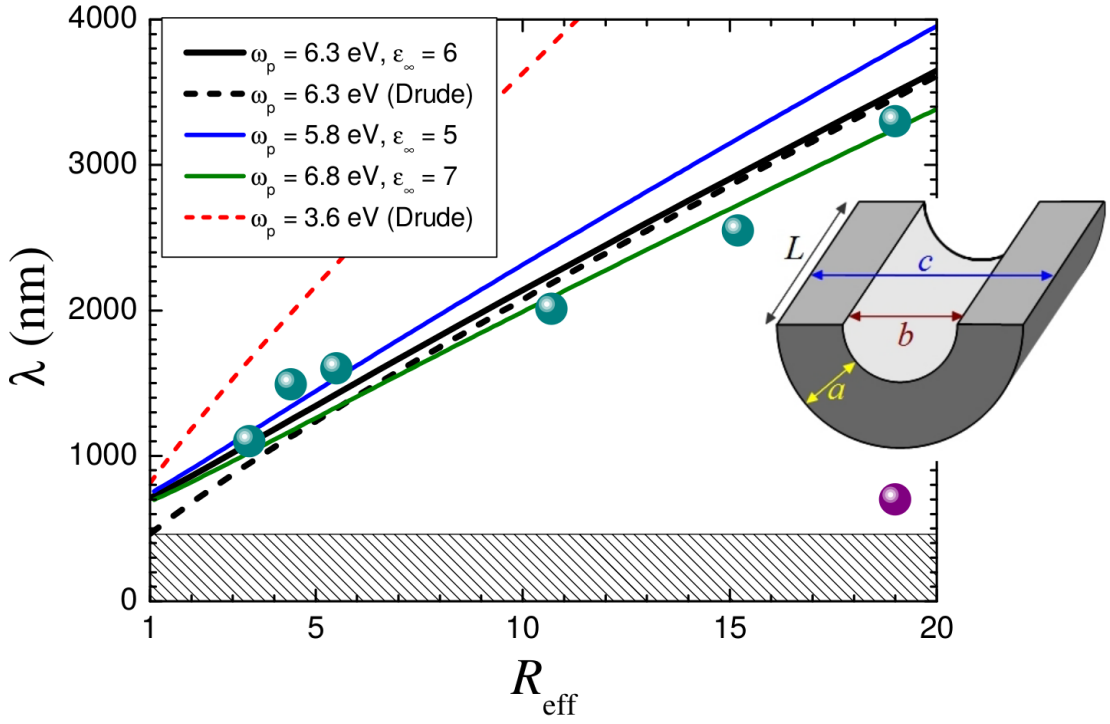

Figure 4.2: Theoretical wavelength of axial plasmonic modes obtained with Drude-Lorentz (solid lines) and Drude-only (dashed lines) dielectric functions (solid lines) as a function of the $WO_{2.72}$ hemitube effective aspect ratio R_{eff}. The experimental wavelengths of the axial modes are represented by green symbols, whereas the wavelength where perpendicular modes arise in the spectrum for large-aspect-ratio hemitubes is depicted by a purple circle. The shadowed area indicates the zone of the spectrum dominated by interband transitions.

by an hemitube (see chapter 2). In brief, the optical response is approximated by the one corresponding to an *equivalent spheroid* of aspect ratio R_{eff}, in such a way that the frequency of maximum absorption for the hemitube and for its equivalent spheroid coincide. Once the effective aspect radii are determined, and since the absorption of a spheroid is fully analytical, it is inexpensive to compare the experimental maxima with the theoretical one for different values of ω_p and ε_∞ (remember that $\gamma_D \simeq 0.9$ eV and the Lorentz parameters are already fixed).

As shown in Fig. 4.2, when the full dielectric function (Eq.4.2) is used with parameters $\varepsilon_\infty \simeq 6$ and $\omega_p \simeq 6.3$ eV, there is a fairly good overall agreement between the experimental and theoretical maxima. A slightly better account of the absorption maxima for the most elongated hemitubes is reached if $\omega_p \simeq 6.8$ eV and $\varepsilon_\infty \simeq 7$, but the agreement for the shortest hemitubes is lost. Similarly, $\omega_p \simeq 5.8$ eV and $\tilde{\epsilon}_\infty \simeq 5$ seem to be more appropriate

for the less elongated hemitubes, but such a choice clearly overestimate the wavelength of the axial mode for the longest hemitubes. That is, bearing in mind the unavoidable size/shapes uncertainties we can conclude that the bulk plasma frequency of $WO_{2.72}$ is $\omega_p = 6.3 \pm 0.5$ eV, whereas $\varepsilon_\infty = 6 \pm 1$.

From Eq.2.49 and Eq.2.50, the carrier density is $n_e \sim 3.46 \times 10^{\ \ 22}$ cm^{-3}, which corresponds to $N_{cpm} \sim 1.75$ carriers per molecular $WO_{2.72}$ unit, and the conductivity is $\sigma \sim 6 \times 10^3\ \Omega^{-1}$cm^{-1} (we have considered that the molar mass is 227.4 g/mol, that the mass density is 7.45 g/cm^3, and that the effective mass of the carriers is $m* \sim 1.2m_e$, as done in previous studies of the plasmonic response of WO_3 nanorods [36]).

Despite the overall good agreement with the experimental axial-plasmon frequencies, the use of an isotropic dielectric function is not appropriate for the present case. Indeed, for axial (perpendicular) modes the natural length D appearing into Eq. 2.50 is the hemitube length L (the wall thickness a). Since $L \gg a \sim 2$ nm, shape anisotropy has to be incorporated into the model dielectric function through an orientation-dependent γ_D. Then, whilst $\gamma_D = \gamma_{bulk} \sim 0.9$ eV is a reasonable choice for the Drude damping frequency of axial modes, for perpendicular modes (i.e. to analyze the optical response if the incident light is polarized on the plane perpendicular to the hemitube axis) we must take a value $\gamma_{D,\perp}$. The Fermi velocity corresponding to $n_e = 3.46^{22}$ cm^{-3} is $v_F \sim 10^4$ cm/s, and taking $D \sim a \sim 1 - 3$ nm in Eq. 2.50 we have that $\gamma_{surf} \sim 0.7 - 0.2$ eV. Thus, in our definite dielectric function the Drude damping frequency is $\gamma_{D,\perp} \simeq 0.9$ eV if the incident light is polarized along the hemitube, but $\gamma_{D,\perp}$ should lie within the range $1.1 - 1.6$ eV if the incident light is perpendicularly polarized with respect to the hemitube axis.

4.3.1 The dielectric function

The model dielectric function that we have derived above assumes that the material is isotropic, since the different values of γ_D aim at incorporating the shape anisotropy of the samples. However, the monoclinic-phase $WO_{2.72}$ holds intrinsic crystal-structure anisotropies, which would lead to a LSP-peak splitting even for nanostructures with aspect

ratio close to one [230]. However, we have already commented that the splitting of the absorption spectra only appears for very elongated hemitubes.

As a consequence, crystal-anisotropy effects are expected to play a minor role if compared to shape-anisotropy ones, so we will not consider the former in our analysis. A different issue is the actual origin of the broadening of the main plasmon peak in the observed spectra. We have considered that it is mainly related to the finite conductivity of the carriers (i.e. to *intrinsic* effects), but the unavoidable size dispersion of the samples and/or the coexistence of hemitubes with slightly different stoichiometries might be important as well. This has been recently reported as the main source of the observed width of plasmon resonances in aluminium-doped zinc oxide nanocrystals [231]. Therefore, our estimated value $\gamma_{bulk} \simeq 0.9$ eV is actually an upper bound for the intrinsic damping $WO_{2.72}$. Note that such a damping lead to quality factors Q of the order of 1.5 for the axial resonances and of the order of 2.0 for the perpendicular ones (although the latter are obscured by the nearby axial modes for the small- and medium-length hemitubes). On the contrary, typical quality factors for coinage-metal plasmonic structures are ten times larger. However, after a simple analysis of the uncertainty of the bulk plasmon frequency by incorporating sample size dispersion and a plausible coexistence of other stoichiometries close to the nominal one $WO_{2.72}$ we can conclude that the quality factor of the plasmon resonances for *individual* hemitubes may be of the order $Q \sim 4$.

4.3.2 DDA numerical spectra

A detailed analysis of the whole vis-IR absorption spectra requires fully numerical discrete-dipole approximation (DDA) calculations since our simple semi-analytical model only accomplishes the hemitubular shape in an averaged manner. The comparison between experimental and numerical DDA results for different samples is presented in Fig.4.3. As expected, there is a very good overall agreement between experiment and theory. The main reason explaining the small quantitative disagreements between DDA and experiments is the unavoidable size/shape uncertainty of the samples. However, is worth men-

tioning that the strong confinement of electrons within the walls conforms to a scenario close to the limit of validity of classical local-optics [76] and hence of the DDA. Non-local optics corrections and/or quantum confinement effects might provide further corrections to the classical-local-optics spectra [81, 232]. In any case, none of these considerations affects the essence of our analysis: numerical DDA simulations with a suitable, physically motivated dielectric functions provide an excellent account of the experimental trends.

DDA calculations allow us to explore in more detail the nature of the absorption spectrum. In Fig.4.4 we present the contributions to the total DDA absorption corresponding to incident light polarized in the x, y, and z directions for a hemitube with effective aspect ratio of 10.7. As can be observed, the plasmonic response appears to be the superposition of three modes. The first and weakest one is located around $\lambda \sim 700$ nm and is excited by x-polarized light. The second appears at a slightly large wavelength ($\lambda \sim 800$ nm) and emerges as a response to y-polarized light. These two spectral features constitute the perpendicular plasmonic response, but are so close to each other that cannot be resolved either in the experimental spectrum or in the total DDA one. Finally, as we have already discussed, the main spectral contribution comes from the axial mode. We also depict in Fig. 4.4 snapshots of the driven induced density for each mode. As expected, induced densities behave as oscillating dipoles along the incident E-field direction, but they are distorted due to the different curvatures of the surface. This is especially evident for the highest-frequency mode (x-axis polarization).

The aspect-ratio dependence of the components of the decomposed absorption is depicted in Fig. 4.5. The x-axis mode appears in a narrow range of wavelengths ($650 - 750$ nm) although its position and shape is practically the same for all the hemitubes with $R_{eff} > 5$. The second perpendicular mode (y-axis polarization) appears in a slightly broader range ($750-1000$nm) but, again, it is quite insensitive to the geometrical details of the hemitubes as long as $R_{eff} > 5$. Finally, the absorption for incident light polarized along the hemitube main axis is redshifted as the aspect ratio of the hemitubes increases. Hence, despite the unique hemitubular shape of the synthetized nanostructures, the perpendicular modes are very robust with respect to variations of the geometry, whereas the axial mode displays

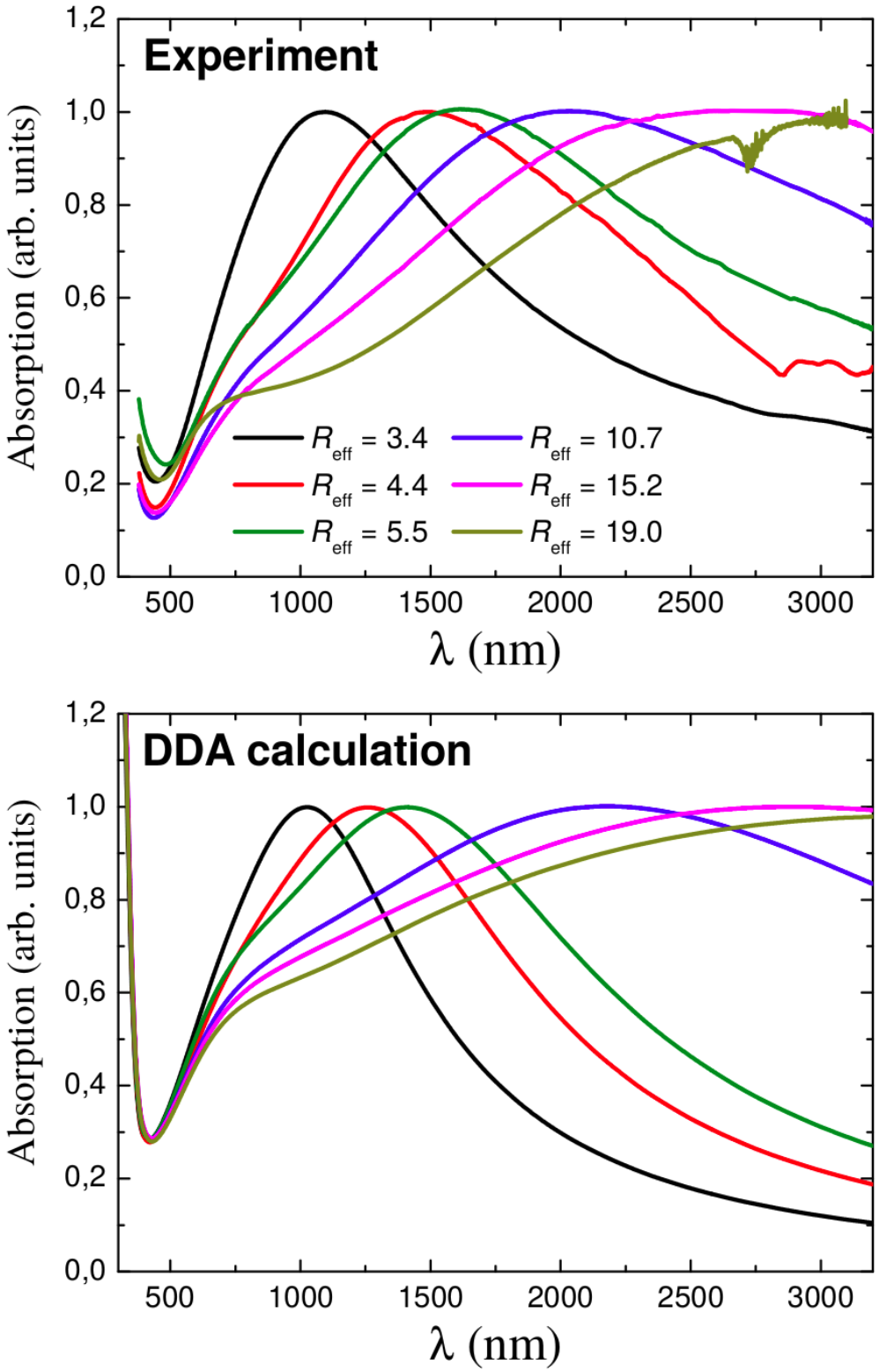

Figure 4.3: Vis-IR normalized absorption of $WO_{2.72}$ hemitubes with different effective aspect ratios R_{eff}. Upper panel: experiments; bottom panel: numerical DDA calculations. The DDA spectra is equal to the incoherent sum of the absorptions for incident light polarized in the three Cartesian directions (x,y,z), and a damping $\gamma_{D,\perp} = 1.4$ eV has been used for the evaluation of the perpendicular response. Note that the λ-dependent representation of the absorption overemphasizes the differences in the long-wavelength range.

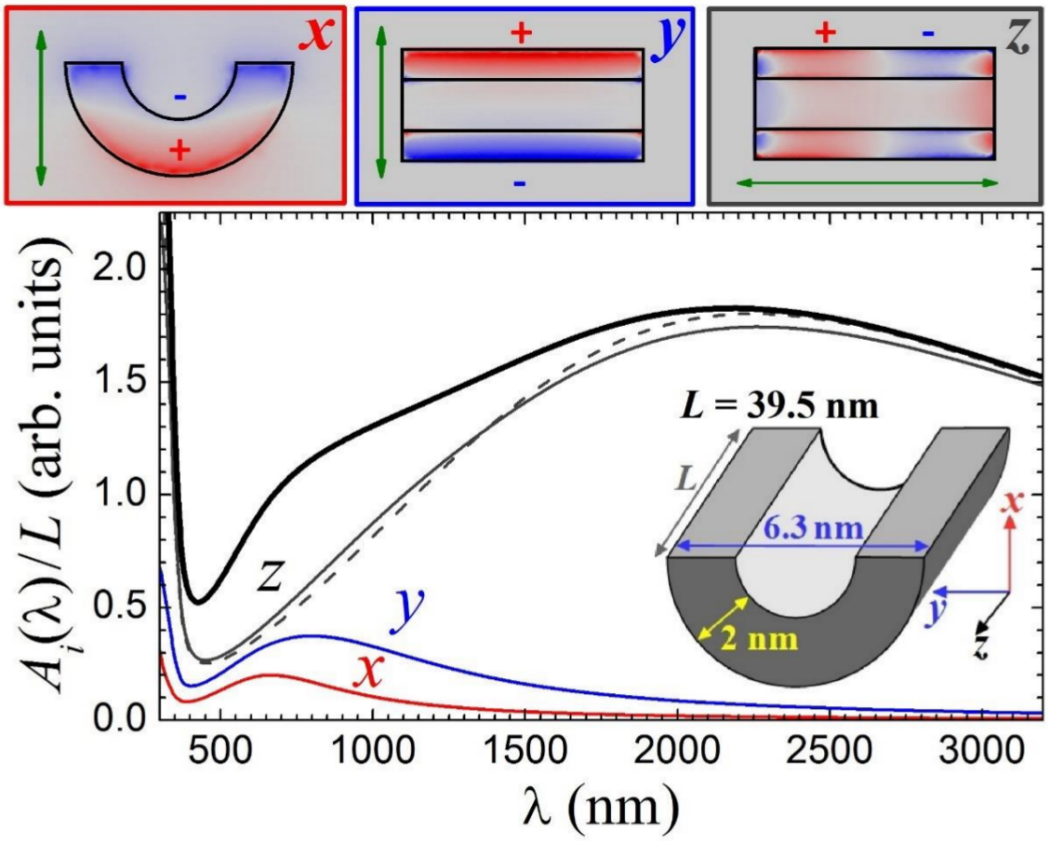

Figure 4.4: (Top panels) Sketch of the driven induced surface charge densities for the three resonances corresponding to each polarization of the incident E-field. (Bottom panel) Decomposition of the DDA absorption (thick black line) for a hemitube (effective aspect ratio $R_{eff} = 10.7$) in contributions corresponding to x-, y-, and z-polarized incident light (red, blue, and dark grey solid lines, respectively). The dark- grey dashed line is the analytical absorption $A_z(\lambda)$ for a spheroid with the same aspect ratio.

the characteristic length tunability of standard, more symmetric nanorods.

4.3.3 Electric field enhancement[1]

Of paramount importance is the analysis of the near field induced by the plasmonic response. Many of the plasmonic-based applications relies on the ability of metallic nanostructures to enhance and concentrate light at a scale far smaller than the wavelength of the incident light.

In the present scenario, the existence of different length scales (length, width, wall thickness) should be reflected on near-field enhancement patterns. This is confirmed in Fig. 4.6, where we plot contour plots of the corresponding E-field enhancement, $|E_{tot}(r,\omega)|/|E_{ext}(r,\omega)|$, for the three frequencies that maximizes the absorptions for external incident fields $E_{ext}(r,\omega)$ polarized along the three Cartesian axes. As we may observe, at a distance $s = 1$ nm from the upper face of the hemitube there exist four well-defined "hot spots" of nanometric size associated to the axial LSP and for x-polarized incident light. Such spots also appear when perpendicular LSP are excited by y-polarized light, but are more diffused. Most noticeably, in all the cases the near-field patterns are distorted according to the hemitubular shape of the nanostructure.

4.3.4 Fine structure of the absorption spectra

As we have seen, optical absorption, induced charge surface densities, and electric field enhancement patterns exhibit a rich structure that are absent in simpler, most compact nanoestructures. As anticipated, it is plausible that loses were overestimated in our calculations since we used damping frequencies ($\gamma_{D,z} = 0.9$ eV and $\gamma_{D,\perp} = 1.4$ eV) aiming at reproducing the experimental optical absorption. For this reason, it is interesting to re-evaluate numerically the optical absorption, but using smaller damping frequencies, and to

[1]The electric field enhancement calculations were made by Antonio Fernández-Domínguez from the Universidad Autónoma de Madrid, and are included in this work for the completeness of the theoretical analisys we did in collaboration.

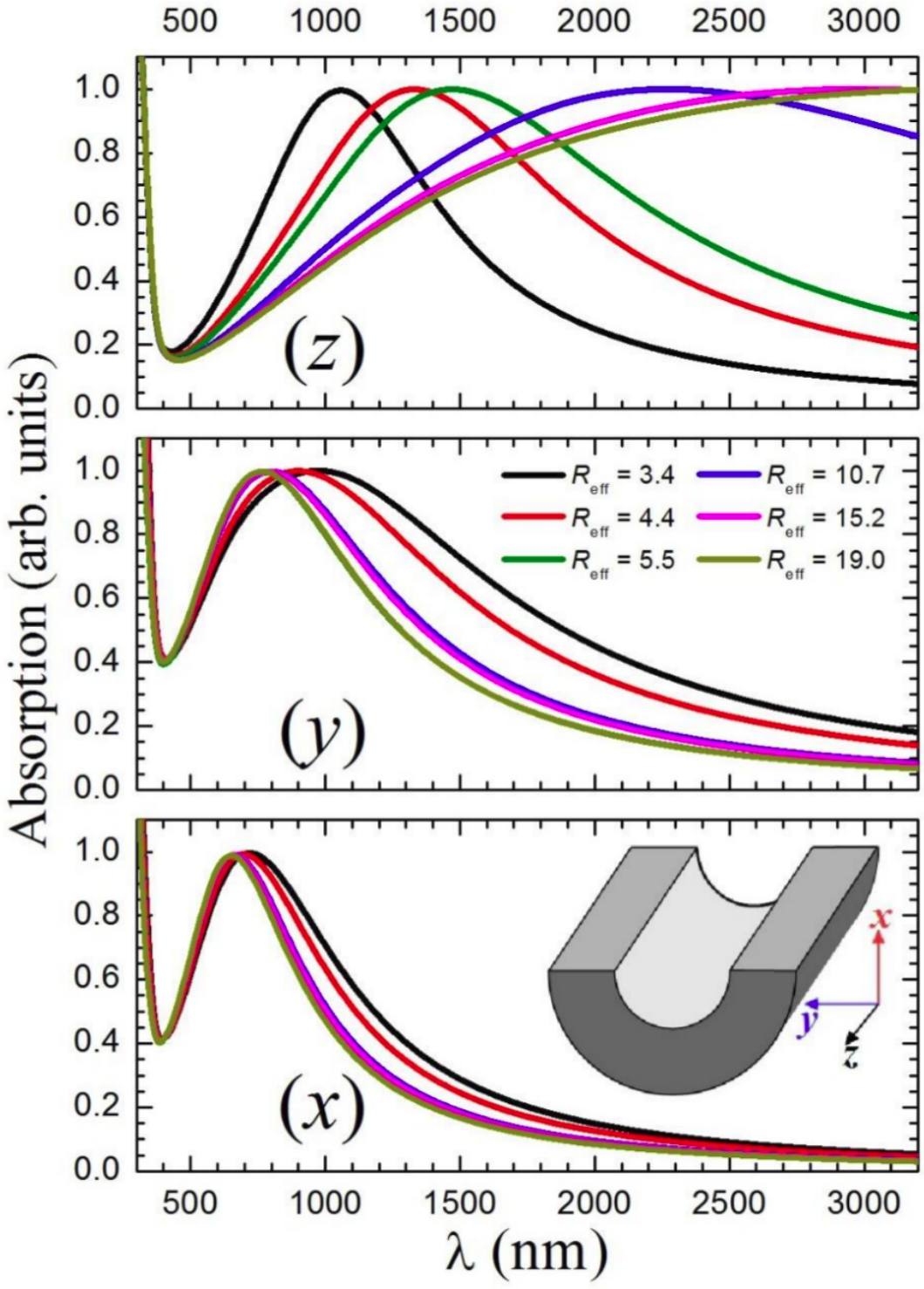

Figure 4.5: DDA absorption spectra for x-, y-, and z-polarized incident light as a function of the effective aspect ratio. Note that the perpendicular response is practically the same for medium and large aspect ratio hemitubes, regardless their geometrical details.

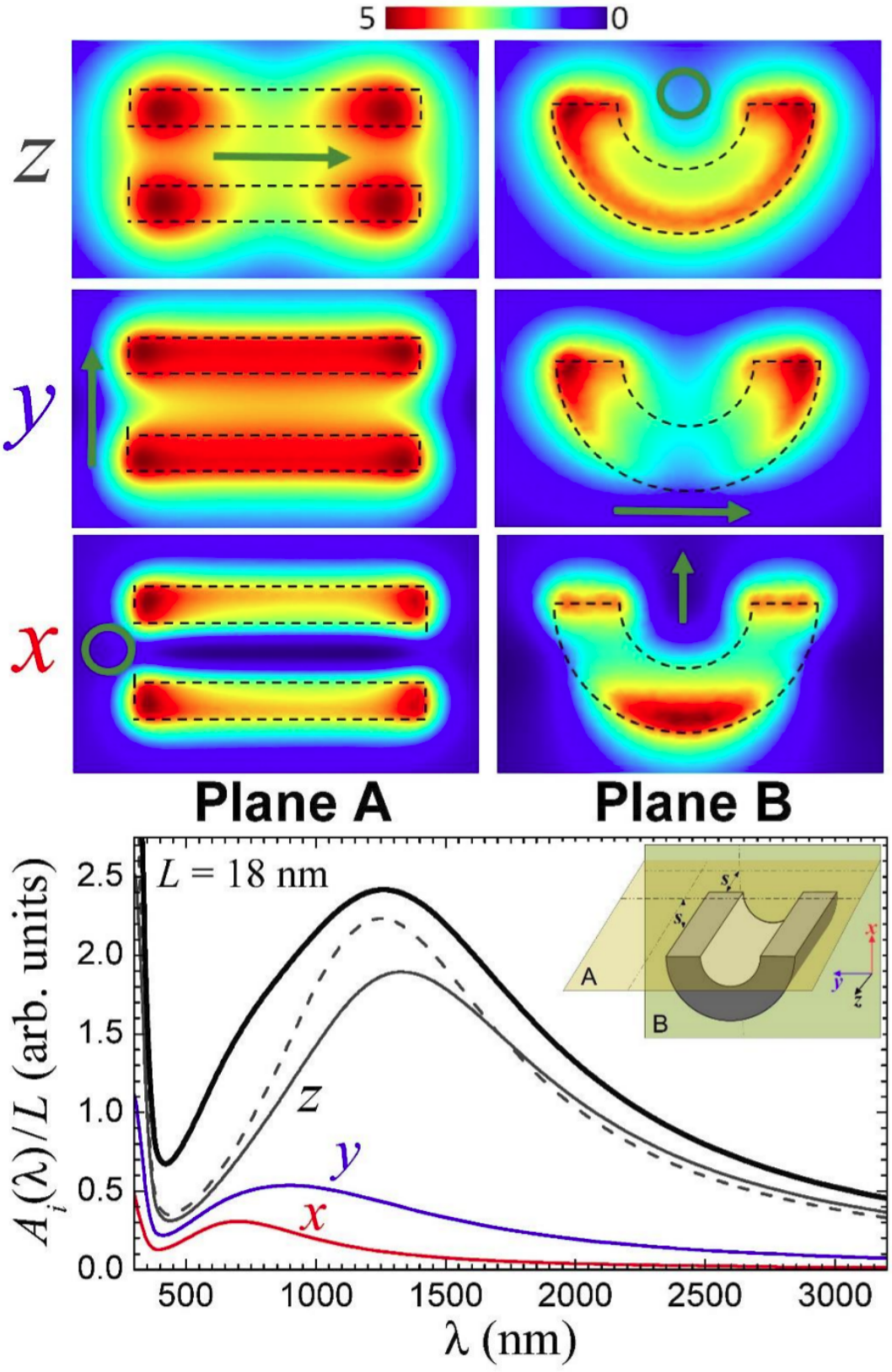

Figure 4.6: Top panels: Contour plots on two selected planes of the electric field enhancement corresponding to the resonances for x-, y-, and z-polarized incident light. As depicted in the inset within the bottom panel, plane A (B) is parallel to the upper (front) face of the hemitube and located at a distance $s = 1$ nm. Bottom panel: As in Fig. 4.4 for a short hemitube with effective aspect ratio $R_{eff} = 4.4$.

compare the absorption spectrum with those corresponding to other simpler geometries.

In Fig.4.7 we present the optical absorption and its polarized-dependent contributions for a short hemitube ($R_{eff} = 4.4$) and for a long one ($R_{eff} = 15.2$) one, but using small damping frequencies ($\gamma_{D,z} = \gamma_{D,\perp} = 0.2$eV). We can see that the single-peak absorptions $A_x(\omega)$ and $A_y(\omega)$ depicted in Fig. 4.5 are actually the result of a convolution of, a least, five resonances. Moreover, some of such resonances can be excited by incident light polarized in different directions. For instance, the weak resonance at $\lambda \simeq 600$ nm can be excited by electric fields oriented in both the x and y directions, whereas there are further resonances that can be excited by electric fields with axial and perpendicular polarizations. In general, the main spectral feature corresponding to incident light which is polarized along a single Cartesian axis cannot be (or can be very weakly) excited by electric fields with perpendicular polarizations. Therefore, the eigenmodes and electric field enhancements associated to these resonances are expected to be quite similar than those depicted in Fig. 4.4 and Fig 4.6, respectively. However, the induced electric dipole for the weakest spectral features is not oriented along any Cartesian axis and, therefore, can be seen as the result of shape-induced hibridizations between simpler modes that resembles those appearing in an elongated ellipsoid. Finally, for the longest hemitube there is a well-defined pure axial mode at $\lambda \simeq 1300$ nm. Although, of course, the induced density has a non-zero dipolar moment along the z-direction, it can be interpreted as a hybridized multipolar mode that can be excited because of the sharp termination of the hemitube. As we will see below, such mode also appears for cylindrical and hemicylindrical nanostructures.

To determine how interband transitions affect the shape of the fine structure of the perpendicular plasmonic modes, in the bottom panel of Fig. 4.8 we depict the Drude-only absorption spectra for a hemitube with aspect ratio $R_{eff} = 15.2$. Here, we have chosen $\omega_P = 3.4$ eV, $\varepsilon_\infty = 1$, and $\gamma_D \simeq 0.2$ eV to guarantee that the perpendicular modes will appear in the vis-near IR. A direct comparison with the spectra represented in the bottom panel of Fig. 4.7 indicates that, as expected, the presence of interband transitions leads to a damping of the resonances at lowest wavelengths, that is, of the plasmon modes that

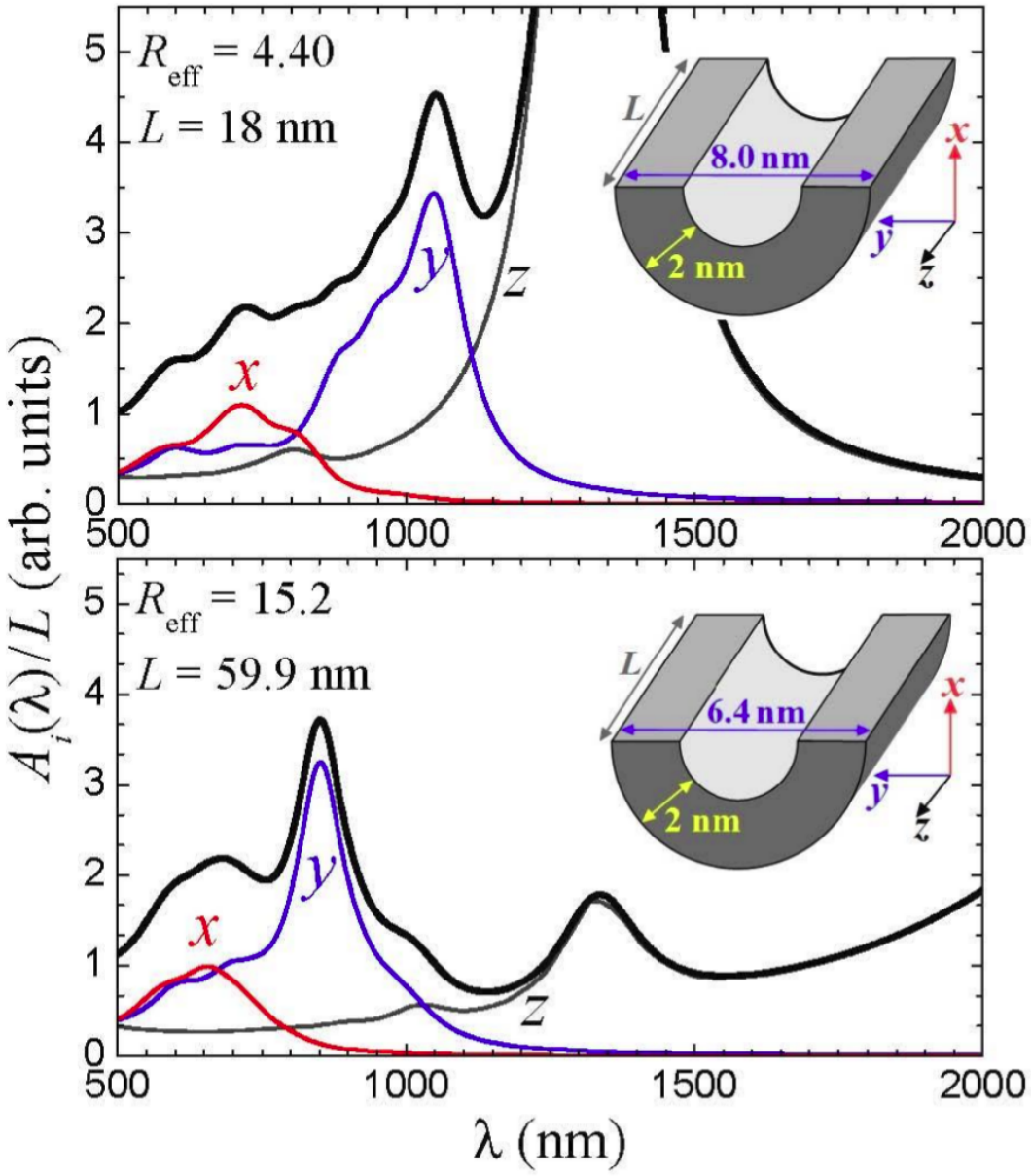

Figure 4.7: Decomposition of the DDA absorption (thick black line) for hemitubes with effective aspect ratio $R_{eff} = 4.4$ (top panel) and $R_eff = 15.2$ (bottom panel) in contributions corresponding to x-, y-, and z-polarized incident light (red, blue, and dark grey solid lines, respectively). The Drude-damping frequency in the Drude-Lorentz dielectric function is equal to 0.25 eV, which allow us to analyse in detail the fine structure of the response in the range $500 - 1500$ nm. The main axial resonance for the longest hemitube appears at $\lambda \simeq 3000$ nm and, therefore, the axial resonance at $\lambda \simeq 1300$ nm is a "multipolar" mode that can be excited due to the sharp termination of the hemitube.

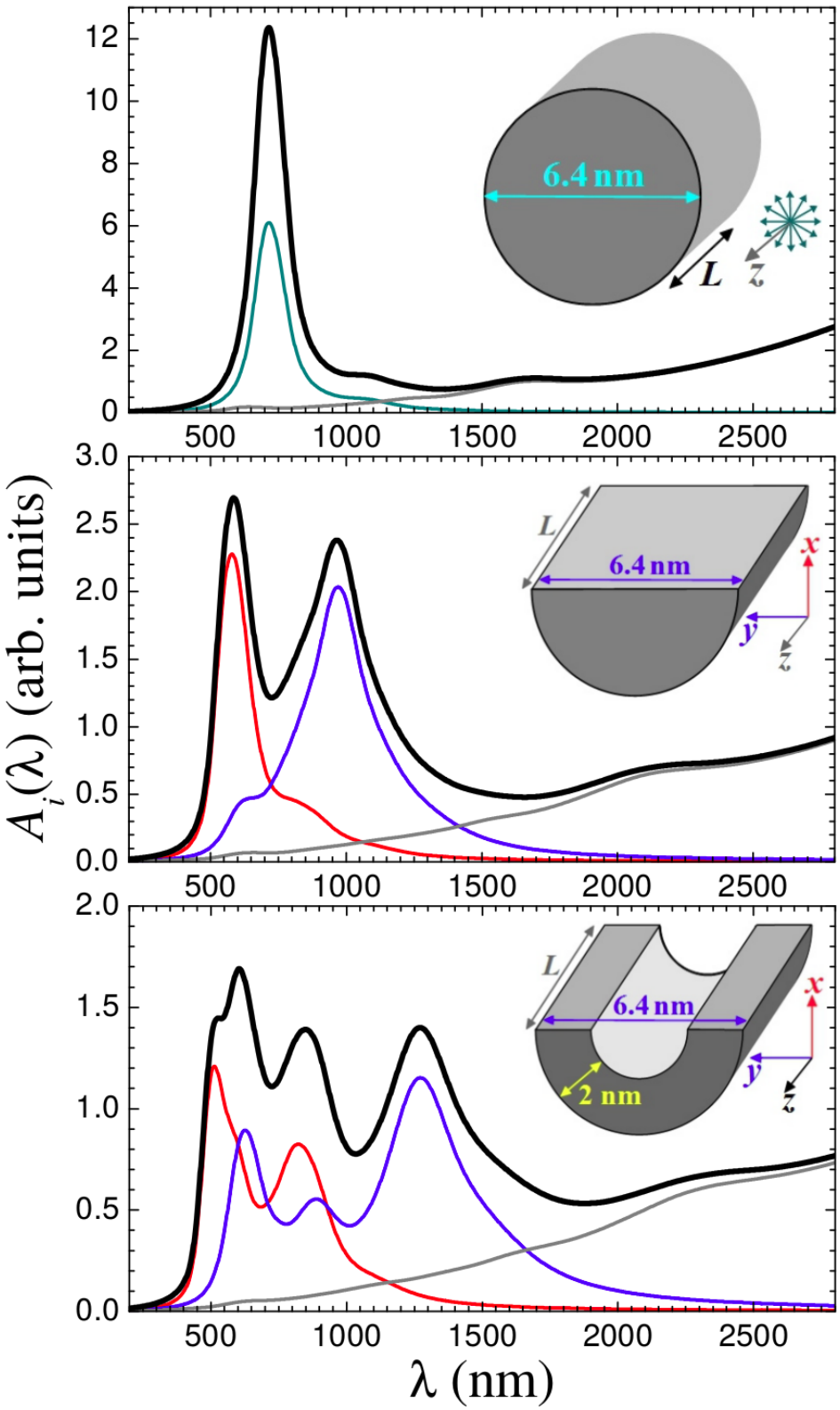

Figure 4.8: From top to bottom: decomposition of the DDA absorption (thick black line) for a cylinder of length $L = 59.9$ nm and diameter $c = 6.4$ nm, a hemicylinder, and a hemitube in contributions corresponding to x-, y-, and z-polarized incident light (red, blue, and dark grey solid lines, respectively). To allow for a comparison only based on the different geometries of the nanostructures, the dielectric function does not include contributions from interband transitions, and the corresponding Drude parameters are $\omega_P = 3.4$ eV, $\varepsilon_\infty = 1$, and $\gamma_D \simeq 0.2$ eV.

are closer to the interband transitions. In any case, up to different spectral weights and frequency shifts, the resolved structure of the perpendicular response without interband transitions is, as expected, rather similar than the response with interband transitions.

Finally, to show how the hemitubular shape is responsible of the fine structure of the plasmonic response, we represent in the first and second panels of Fig. 4.8 the absorption spectra for a cylinder and for a hemicylinder (length $L = 59.9$ nm, diameter $c = 6.4$ nm) using the same Drude-only dielectric function. In all the cases the main axial plasmonic mode is out of scale, and the axial mode that appears at $\lambda \simeq 1700$ nm in the cylinder and at $\lambda \sim 2300$ in the hemicylinder and the hemitube is the already discussed hybridized multipole axial resonance. Focusing on the perpendicular modes, whereas the absorption spectrum for a cylinder is dominated by a single peak at $\lambda \simeq 750$ nm, the hemicylinder absorption exhibits two well defined peaks that are above and below a much weaker spectral feature. That is, the spectrum resembles that of an ellipsoid with three different main axes plus an additional weaker hybridized perpendicular mode. Finally, when the hemicylinder is carved we can see how the plasmon resonance corresponding to the y-direction (x-direction) is redshifted (blushifted), and the emergence of new hybridized plasmon resonances which, in addition, have a better resolution than the hybridized mode of the hemicylinder.

4.4 Conclusions

The experimental optical absorption of synthesized $WO_{2.72}$ hemitubes can be well understood in terms of the classical Mie-Gans theory [3, 4]. The vis-IR optical spectra are dominated by a broad [full width at half maximum (FWHM) $\gamma \simeq 0.9$ eV/$\hbar$] but intense peak whose position depends very sensitively on geometry of the sample. A second and much weaker spectral feature, which only emerges as a discernible shoulder in the spectra for the longest hemitubes, appears around $\lambda \sim 700$ nm for all the samples. The lower-energy peak can be attributed to a localized surface plasmon (LSP) associated to collective oscillations of the conduction electrons along the hemitube axis (hereinafter labeled as

"axial mode"). On the contrary, the higher-energy feature corresponds to LSPs where the electrons mainly oscillate in the direction perpendicular to the hemitube axis. We denominate "perpendicular modes" to such collective excitations. Therefore, the maxima of the experimental absorption can be assigned (up to a small error) to the frequency of the axial mode.

Chapter 5

TDDFT study on femtosecond laser ablation on finite 2D/3D systems

5.1 Introduction

The rapid development, and the increasing availability of intense and ultrashort laser systems over the last years has opened up a wide range of new applications in industry, material science, medicine, and even in the arts. One important physical effect in light-matter interaction driven by these intense and ultrashort laser pulses, is the capacity to couple large amounts of energy into the target on a femtosecond time scale, leading to a growing interest in material removal or laser ablation induced by intense and ultrashort lasers pulses, which can be used for the deposition of thin films, the creation of new materials, for micromachining, and even for picture restoration and cleaning [93, 94].

Regarding the time scales, femtosecond laser ablation has the important advantage in such applications compared with standard ablation using nanosecond pulses because there is little or no secondary effects like mechanical or thermal damage on the target being ablated, i.e., neither collateral damage due to shock waves, nor heat conduction/difussion are produced in the material. [94–102].

Along with the great interest in the material removal induced by intense femtosecond lasers

pulses, several experimental and theoretical studies has been published on the topic, some of them including different analytical models wich fits reasonably well the experimental results of ultrashort laser ablation processes [103–107], and a thorough knowledge of the short-pulse laser interaction with the target material is being reached rapidly. However, many fundamental questions remain concerning the physical origin of the material removal process by femtosecond laser irradiation [108].

It is well known that for ultrashort laser ablation processes, there are two mechanisms of material removal, the so-called "gentle phase of ablation" or simply "gentle ablation" at the initial stages, and the consequently "strong-ablation". In this context, there is still a controversy on what is the physical mechanism of ion removal from a surface illuminated by a femtosecond laser pulse in the gentle ablation regime.

Reviwing the literature, some authors argue that the electrons that are removed from the material by the laser pulse, pull ions from the surface. That is called *e*lectrostatic ablation [104,105,109]. However there are even more studies stating that electrons quickly fly away, and the ions are pushed out of the material by the excessive leftover positive charge [110–119]. That is the Coulomb explosion (CE) mechanism. Even more, one method or the other are usually used to explain the mechanism of material removal in the gentle ablation regime, ignoring completelly to the other one [103, 104, 194]. Then, to the best of our knowledge, the apparently simple question of which of the two mechanisms is actually operative in laser ablation is still not answered [195]. One of the reasons is that it is very difficult to image the motion of ions, because they do not strongly interact with optical fields. Motivated by this, in this chapter we present some results based on simulations of laser ablation processes of quite simple structures, with the goal of sheed light on the controversy about the mechanism of ablation in the genle ablation regime.

All the simulations in this chapter were performed at an ab-initio level by using TDDFT coupled with standard Ehrenfest dynamics in the Octopus code [185, 186, 188].

All the calculations were performed by using real-space grids following the first-principle TDDFT formalism implemented in the Octopus code [185, 186, 188] coupled with stan-

dard Ehrenfest dynamics. The wave functions, densities, and potentials were discretized in a real-space grid. Norm-conserving Troullier-Martins' pseudopotentials [196] were employed to properly describe the interaction between the ionic core and the active electrons, and Perdew-Zunger's exchange-correlation functional [197] was used within the time-dependent local-density approximation (TD-LDA).

In order to obtain insights on which is the mechanism of ablation in the gentle-ablation regime, we proceed in a kind of botton-up way, performing simulations from a 0-dimensional system: a Li_4 cluster, to a 2-dimensional system: a graphene nanoribon.

5.2 Li_4 system

In order to start addressing 2D/3D cases, we simulated the laser ablation process of a Li_4 cluster. The frequency dependence of the electron dynamics during femtosecond laser resonant photoionization of this system has been already studied [38]. The ground-state lowest-energy geometry of the Li_4 cluster is a rhombic planar geometry (see Figure 5.1), and the calculated bond length along the rhombus side is 5.68 a.u. which is in good agreement with the experimental and previous calculation values [198–200].

Fig. 5.1 shows the Li_4 cluster placed at the center of a spherical box with a radious of 25 a.u. During the nonlinear laser-material interaction, a imaginary absorbing potential of 5 a.u. is added to the Kohn-Sham Hamiltonian at the box boundary to account for the emitted electrons during the simulation process (light-blue shaded region on Fig. 5.1). As is shown, the simulation box is far enough away of the electronic charge density of the system in their ground state.

In the case of the Li_4, a spatial three-dimensional uniform grid inside a sphere box with the radius of 30 Bohr was employed to describe the wave function (see Figure 5.1). The Li_4 cluster was placed at the center of the sphere box. The time step of $\Delta t = 0.02$ a.u. and grid spacing of $\Delta x = \Delta y = \Delta z = 0.3$ Bohr ensured a stable time evolution.

In order to control for the laser ablation process of the Li_4 cluster during the simulations,

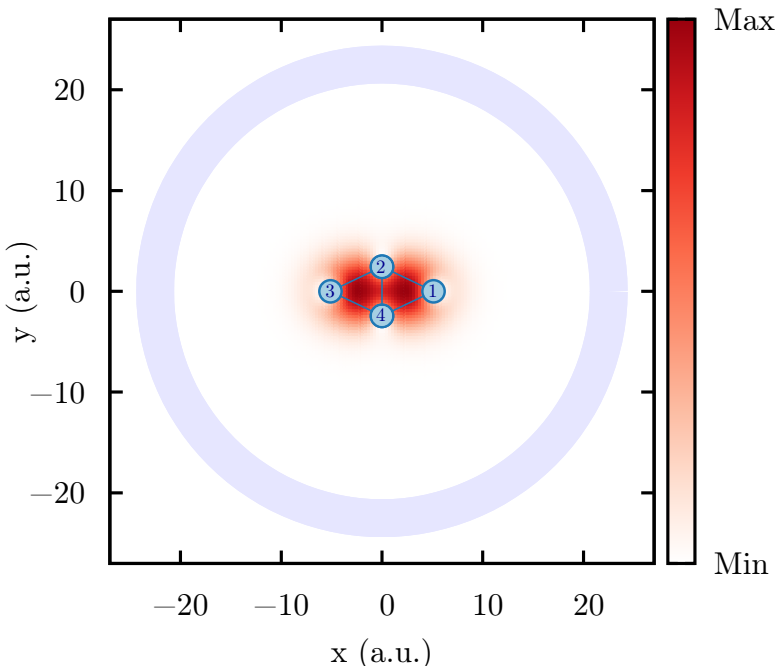

Figure 5.1: Representation of the spherical simulation box used in the calculation. The radius of the simulation box is 25 a.u., including an absorbing boundary condition of 5 a.u. The Li_4 cluster is placed at the center of the simulation box.

only the labeled atom ① was allowed to move freely (see Figure 5.1).

We consider the photoionization of Li4 cluster with a photon energy of 1.66 eV (closer to resonance, see Fig 5.2) and we represent the laser irradiation by subjecting our system to an external alternating electric field parallel to the x axis. laser pulses.

The applied laser pulse is a 45 fs Gaussian wave packet, and the total time of the simulation is 160 fs. Four different laser peak power density of the pulse are used, 1×10^{12} W/cm^2, 3×10^{12} W/cm^2, 5×10^{12} W/cm^2, and 1×10^{13} W/cm^2. Figure 5.3 shows the electric field of the different applied

Figure 5.4 shows the dipole responses along x axis during the simulations. It is quite clear how the dipole response start to increase around $t = 40$ fs for the three cases were the intensity of the laser pulse is higher.

In all the cases, the system starts to ionize rapidly, and the system start to emit electronic charge abruptly, as can be seen from the top panel of Figure 5.5. Once the laser pulse is switched off at $t = 45$ fs, the remaining electrons continue to perform collective oscillations

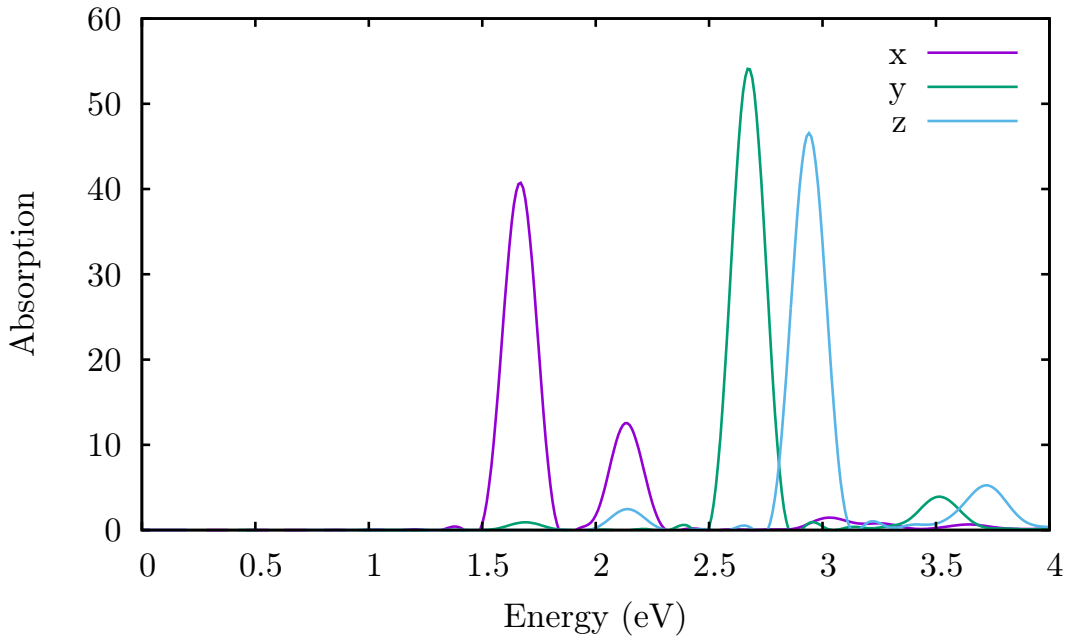

Figure 5.2: Calculated photoabsorption spectra of the Li_4 cluster

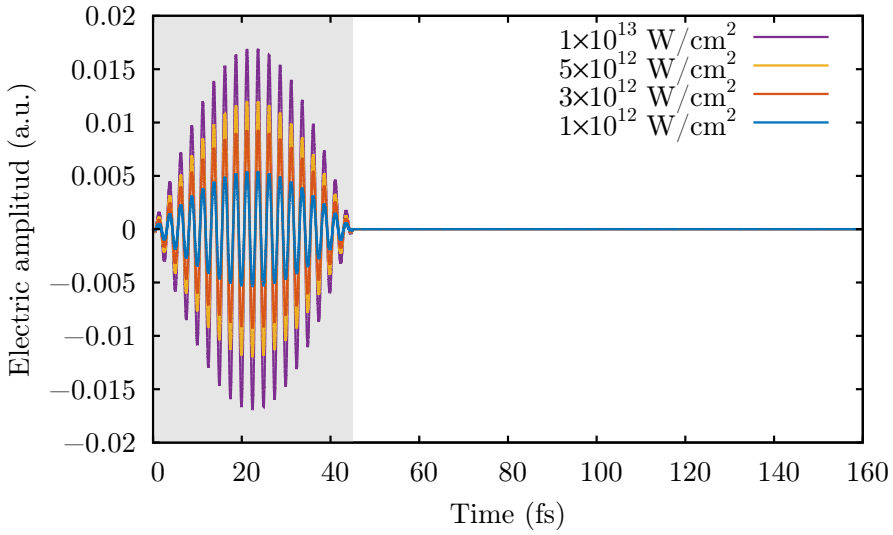

Figure 5.3: Time evolution of the different applied laser pulses.

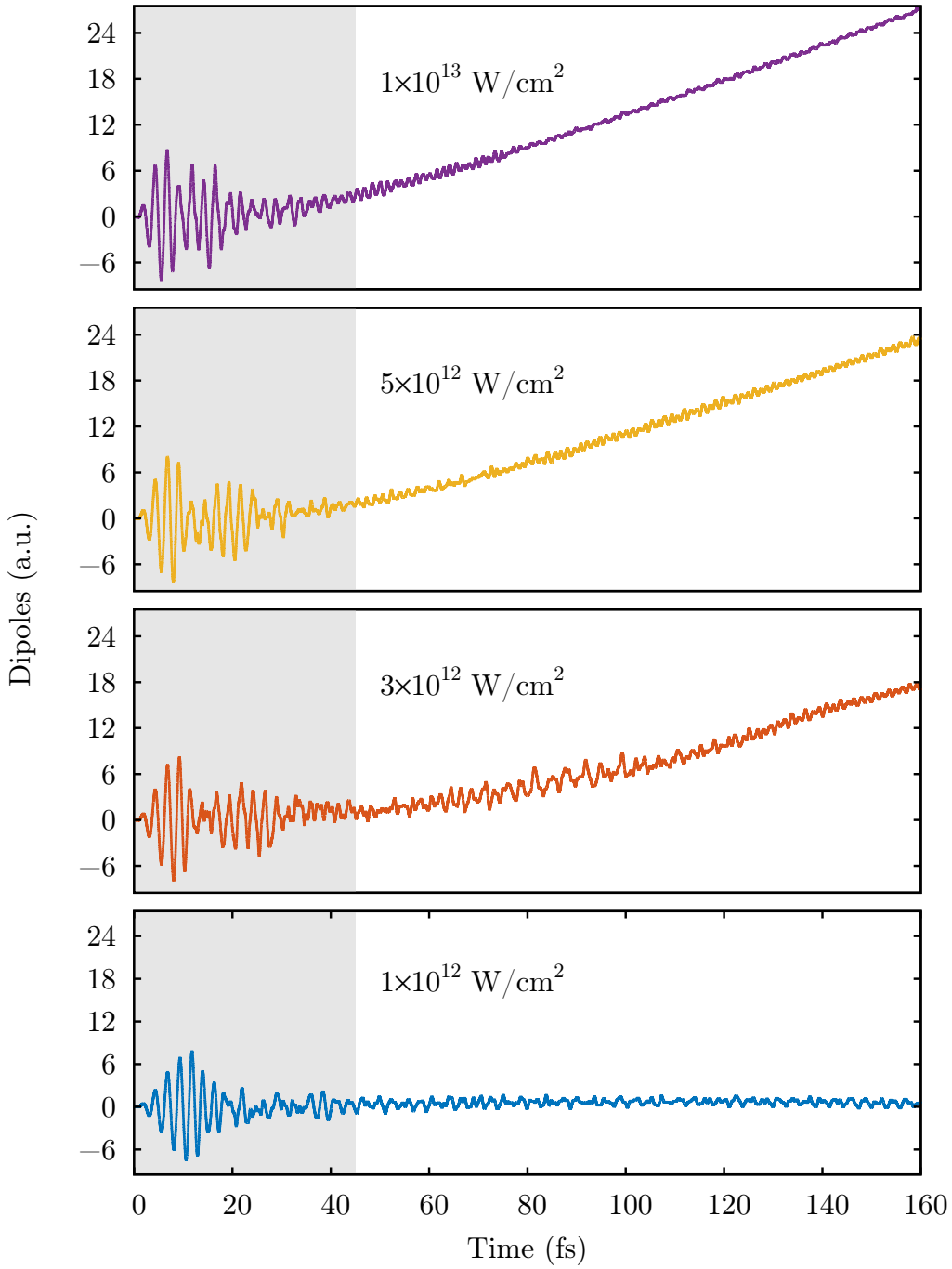

Figure 5.4: Time evolution of the dipoles along x-axis of Li4 cluster under different femtosecond laser irradiation.

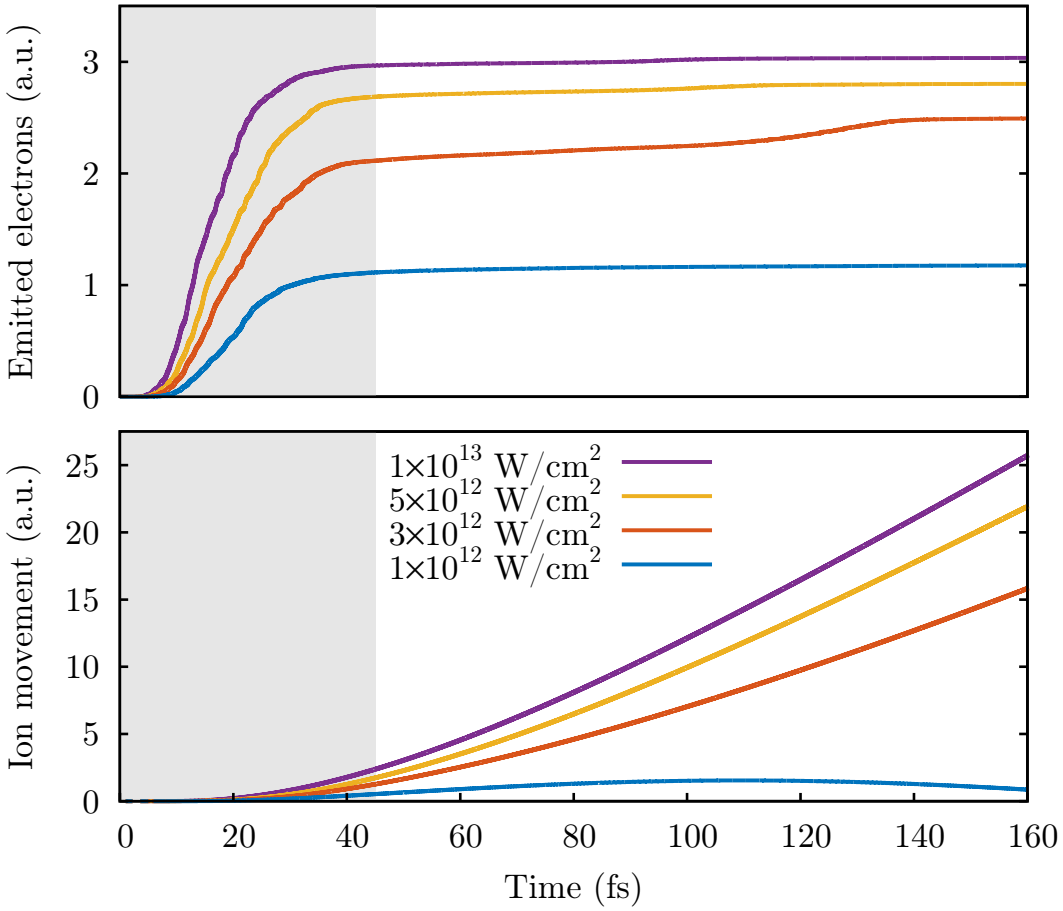

Figure 5.5: (Top panel) Time evolution of the x-displacement of the ① Li atom for the different applied laser pulses. (Bottom panel) Time evolution of the emitted electrons for the different applied laser pulses.

(see Figure 5.4), however bottom panel of Figure 5.5 shows how at around $t = 40$ fs, were the intensity of the laser has decreased considerably, the emission of electronic charge has reached a saturation regime, and during the rest of the simulation time there are almost no emission of electronic charge.

Bottom panel of Figure 5.5 shows the movement of the ① atom through the x axis. Comparing top and bottom panels of Figure 5.5, it is possible to see a correlation between the emission of the electrons and the movement of the ions. We found that in all the cases there was a delay (almost 10 fs) between the departure times for electrons and the ion, suggesting a possible electrostatic ablation case, however this delay is due to the emitted electronic charge is taken into account only once it reaches the absorbing boundary of the simulation box, and the movement of the ions are always taken into account. That is, the

ion starts its movement after the ionization process.

In all the cases the free atom starts to move at around $t = 20$ fs, however only under the most intensity fields (5×10^{12} W/cm^2, 3×10^{13} W/cm^2, and 1×10^{13} W/cm^2) the free ion really leaves the cluster. On the other hand, in the lower intensity case (1×10^{12} W/cm^2), the free atom starts to go back to its original position around $t = 110$ fs, indicating that in this case there were no ablation.

Through the entire evolution of the system, we computed total forces acting on the atom labeled as ① from all electrons and from the rest of the ions. In Figure 5.6, we show the time dependence of the total forces acting on the free ion from the rest of the ions, from all electrons, as well as the combined force from both the remaining ions and all electrons.

As stated above, with the exception of the weaker field (1×10^{12} W/cm^2) where there were no ablation, in all the cases the ionic forces dominates over the electric ones, a concomitant consequence of the previous ionization process. Being this another indication that Coulomb Explosion is the mechanism of ablation of this system.

In order to check the total forces we have performed numerical differentiation of the data of the position of the free ion. Figure 5.7 shows the velocity of the free atom in all the cases.

Figure 5.8 shows the derivated forces of the free atom for the three studied cases. Comparing with the total forces shown on Figure 5.6 there is a noticeable match between them.

In order to try to figure out from where is being emitted the electronic charge, we plot, for the case ① the electron density over the surface of the simulation sphere from $t = 70$ fs to $t = 73.5$ fs.

From the analysis of the electronic density in the simulation sphere we note that spite the electronic charge density is leaving the simulation sphere from all the directions, it mainly does oscillating through the x axis, as could be inferred from the dipole moment (see Figure 5.4). That is, the emision of electrons always keeps the aproximated spherical

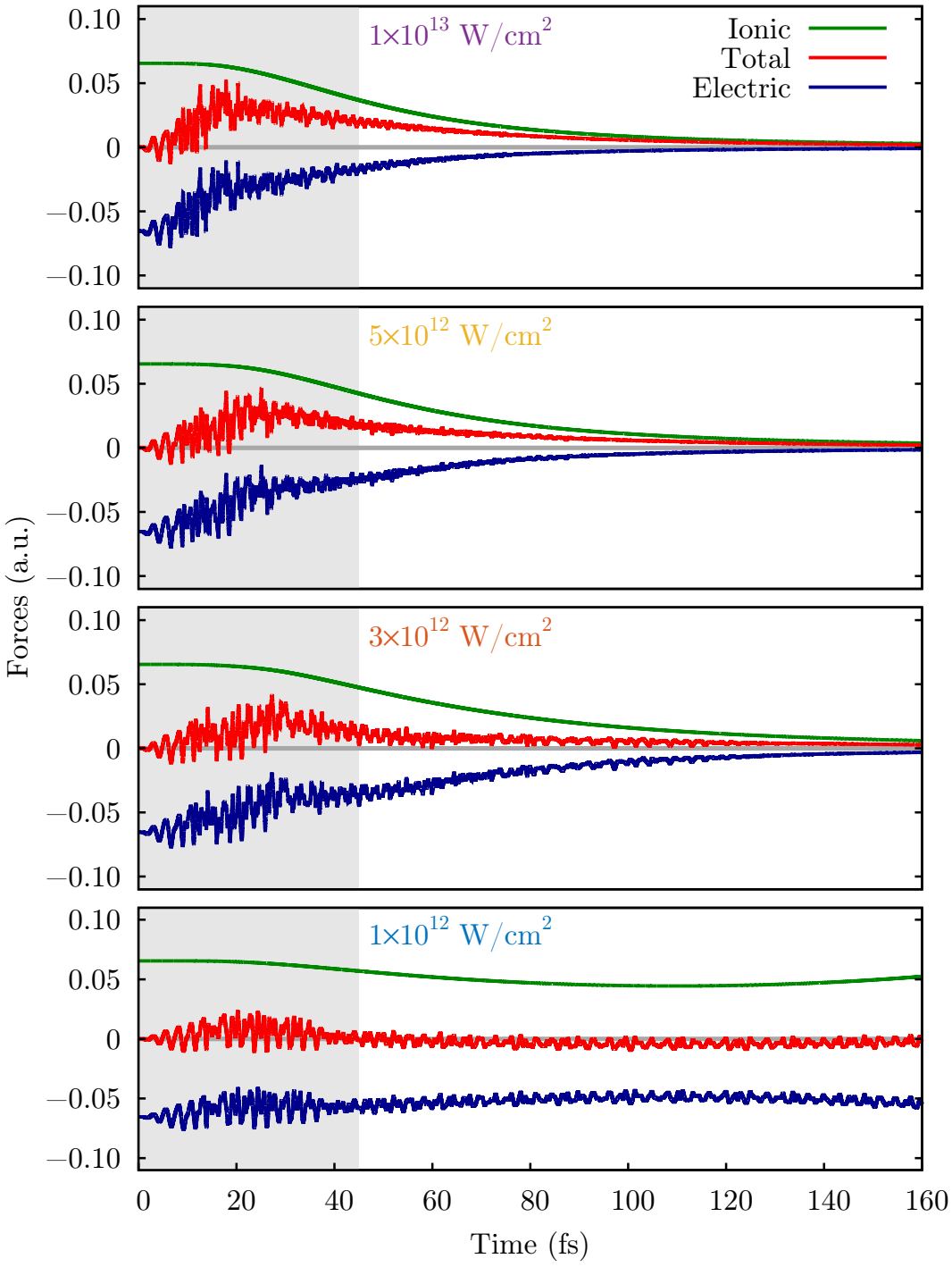

Figure 5.6: Time dependence of the total forces acting on the atom labeled as ① from the rest of the ions, from all electrons, as well as the combined force from both the remaining ions and all electrons for the different laser pulses.

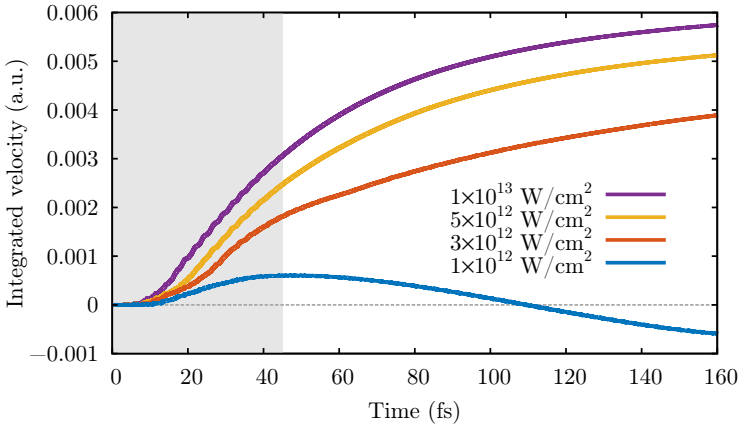

Figure 5.7: Time evolution of the velocity for the free atom in all the cases.

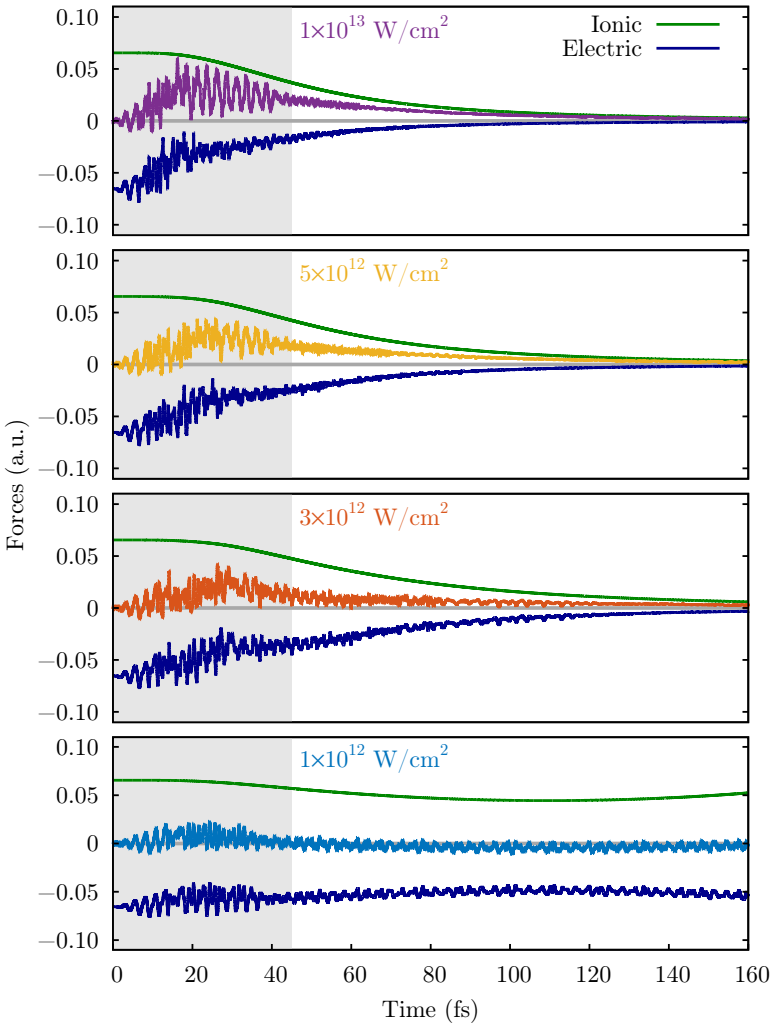

Figure 5.8: Numerical calculation of the forces over the free atom obtained from the positions.

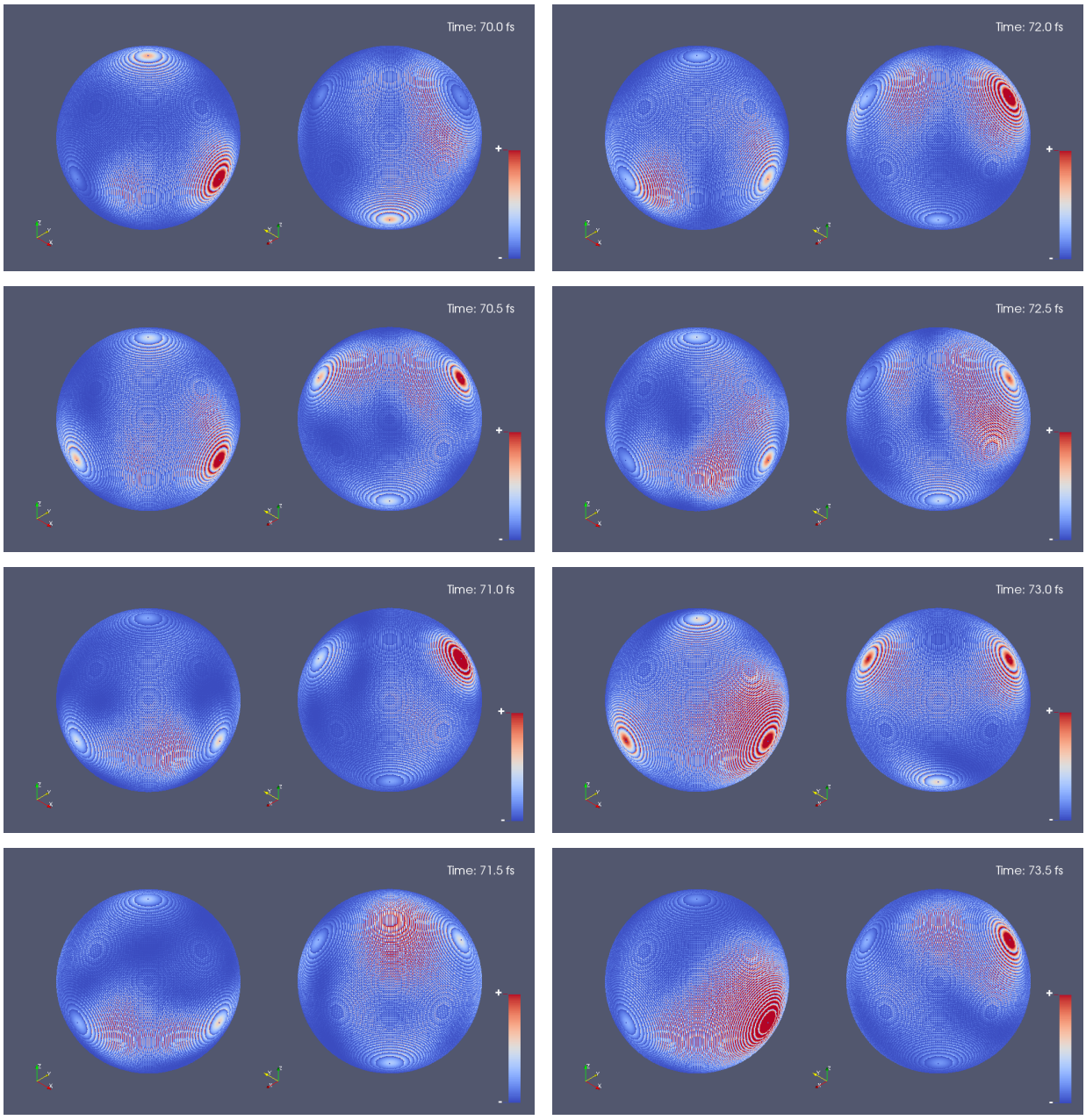

Figure 5.9: Electron density over the surface of the simulation sphere at different times.

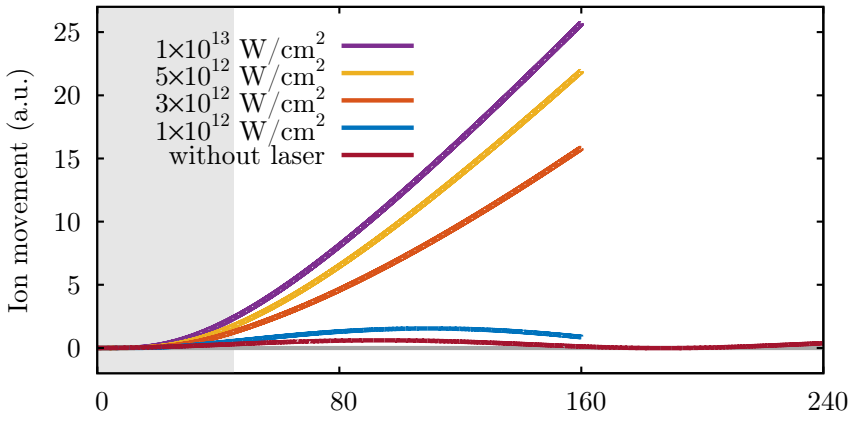

Figure 5.10: Time evolution of the x-displacement of the ① atom applying no laser over the ground state of the four-electron system, but removing artificially the charge density of one electron.

symetry despite the fact that the ionic structures does not. This can be seen as a further confirmation of the abscence of an electrostatic ablation process.

In order to get more insight on the nature of the ablation mechanism we perform an additional simulation, in this case we apply no laser over the ground state of the four-electron system, but we artificially remove one electron, and let the ① atom free to move. This should mimic the extreme case of Coulomb explosion mechanism. Figure 5.10 shows the movement of the ① atom through the x axis.
As can be seen from Figure 5.10, the "free" atom start to move slowly away from its equilibrium position at the beginning of the simulation, but at $t \simeq 95$ fs the free atom starts to go back and it keeps oscillating. The movement of the ① atom with the different laser pulses are also plotted as a reference.

That is quantitatively speaking, the movement of the ion is similar than the one corresponding to the laser-induced ionization.

5.3 Graphene nanoribbon

The previous (Li_4) simulation addres the "0-dimensional" case, while your analysis addressed the "1-dimensional" one. Lets now proceed with a study of the laser ablation of

a 2-dimensional system. To do so, we simulated the laser ablation process of an armchair graphene nanoribbon terminated by hydrogen atoms in three of the four edges. In their ground state, lowest-energy geometry of this system, the atoms are densely packed in a regular hexagonal pattern (see Fig. 5.11).

During the nonlinear laser-material interaction, a imaginary absorbing potential of 2.8 a.u. is added to the Kohn-Sham Hamiltonian at the box boundary to account for the emitted electrons during the simulation process (light-blue shaded region on Fig. 5.11). As is shown, the simulation box is far enough away of the electronic charge density of the system in their ground state.

In the case of the graphene nanoribbon, a spatial three-dimensional uniform grid inside a parallelepiped box ($29.75 \times 39.90 \times 19.95$ Bohr) was employed to describe the wave function (see Figure 5.11). The time step of $\Delta t = 0.06$ a.u. and grid spacing of $\Delta x = \Delta y = \Delta z = 0.35$ Bohr ensured a stable time evolution.

In order to control for the laser ablation process of the graphene nanoribbon during the simulations, only carbon atoms inside the black rectangle (purple-carbon atoms) were allowed to move freely (see Figure 5.11).

We consider the photoionization of small graphene nanoribbon with a photon energy of 6.63 eV (closer to the frequency of the π-plasmon, see Fig. 5.12) and we represent the laser irradiation by subjecting the graphene nanoribbon to an external alternating electric field parallel to the x axis.

The applied laser pulse is a 20 fs Gaussian wave packet, and the total time of the simulation is 100 fs. We have tested several laser peak power densities of the laser pulses, ranging from 5×10^{13} W/cm^2 to 5×10^{14} W/cm^2. As in the case of the Li_4 cluster, the graphene nanoribbon starts to ionize rapidly, and the system start to emit electronic charge abruptly, as can be seen from the top and middle panel of Figure 5.13.

With the exception of the most intense laser pulse cases (1×10^{14} W/cm^2, and 5×10^{14} W/cm^2), top panel of Figure 5.13 shows how at around $t = 20$ fs, were the intensity

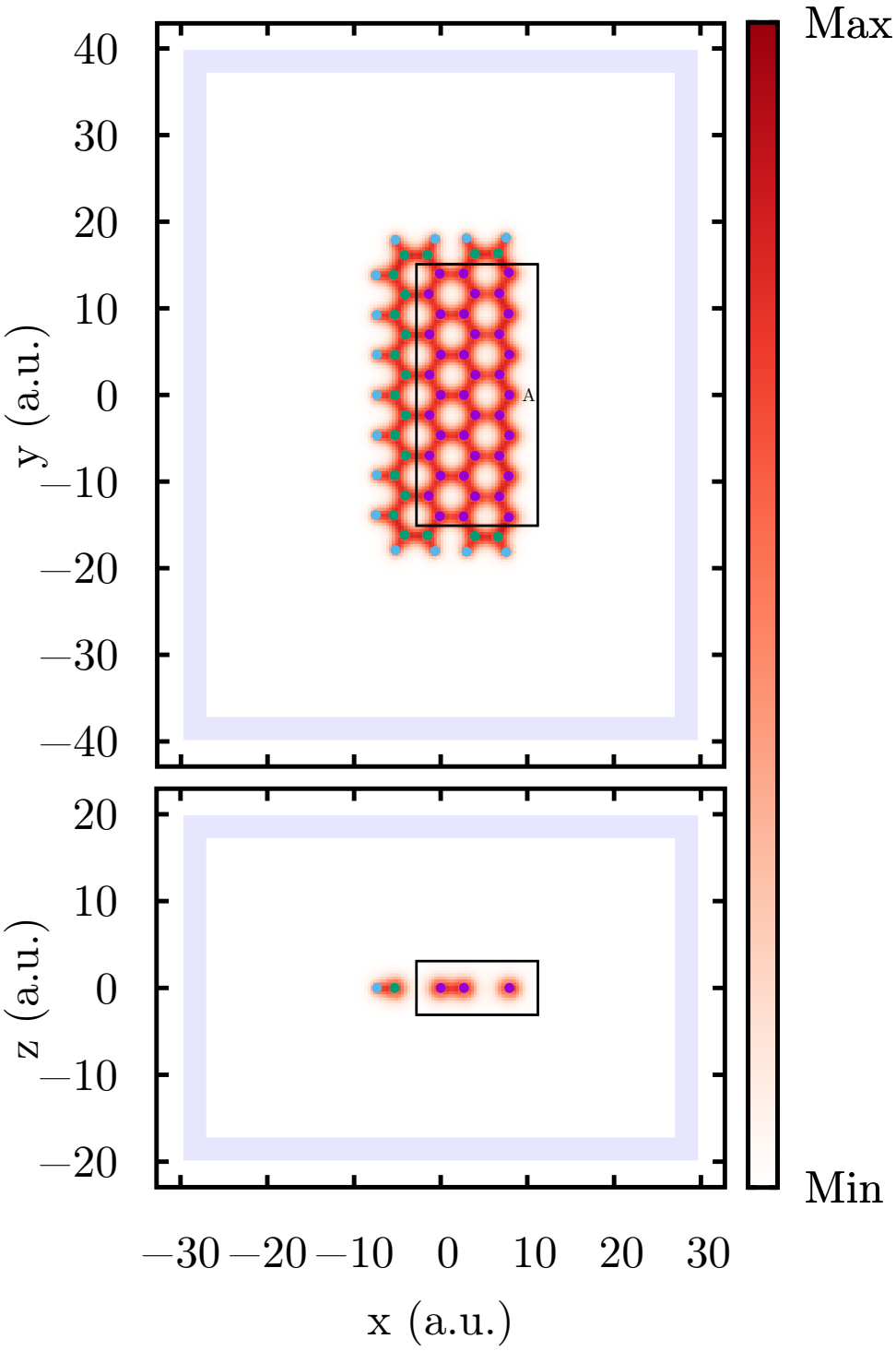

Figure 5.11: Representation of the parallelepiped simulation box used in the calculation. The width of the absorbing boundary is 2.8 a.u. The graphene nanoribon is placed at the center of the simulation box. Only the C atoms inside the black rectangle were allowed to move freely.

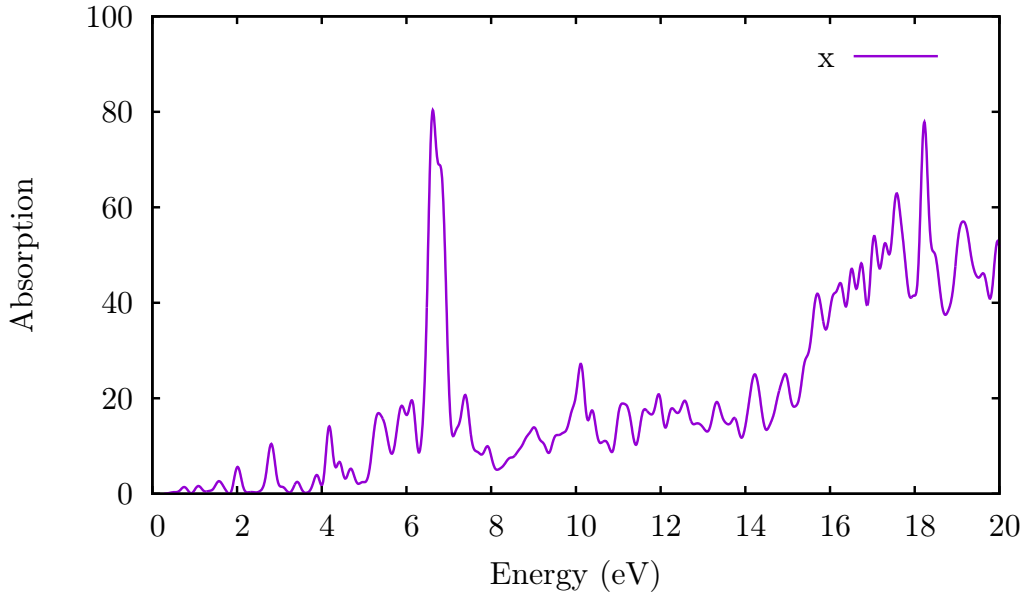

Figure 5.12: Calculated photoabsorption spectra of the graphene nanoribon.

of the laser has vanished, the emission of electronic charge has reached a saturation regime, and during the rest of the simulation time there are almost no emission of electronic charge, however under the most intensity fields (1×10^{14} W/cm^2, and 5×10^{14} W/cm^2) some of the free atoms have reached the boundary of the simulation box early on, provocating an abrupt emission of charge which we do not plot in order to avoid confusion.

Fig. 5.14 shows the dipole response of the system along x axis during the simulation (the gray region represent the duration of the 20 fs laser pulse). It is worth to note how after the pulse is switched off at $t = 20$ fs, the remaining electrons continue performing collective oscillations, and the system continue emitting electronic charge (see top panel of Figure 5.13).

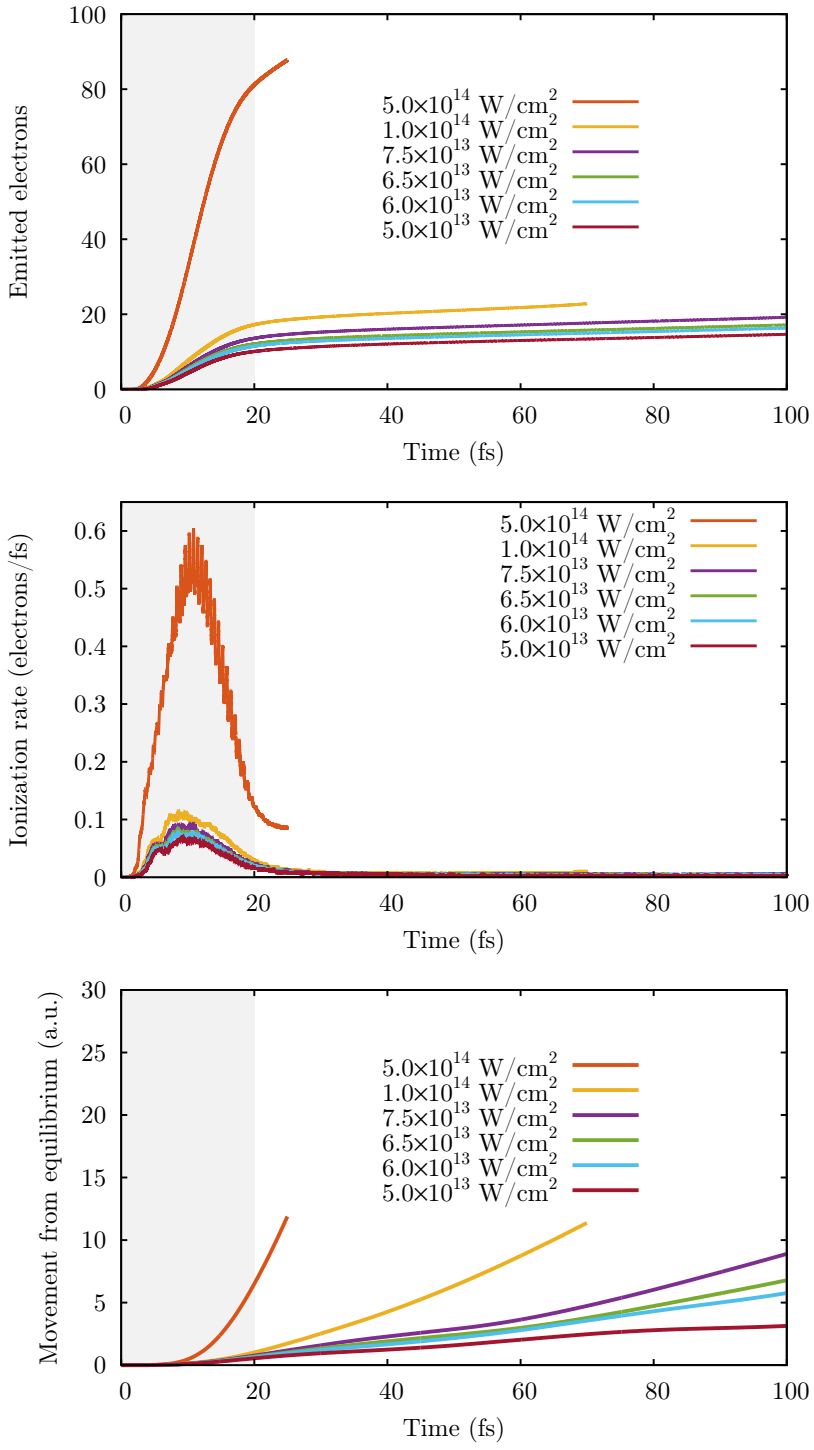

Figure 5.13: (Top panel) Time evolution of the emitted electrons for the different applied laser pulses. (Middle panel) Ionization rate as a function of the time. (Bottom panel) Time evolution of the x-displacement of the "A" atom for the different applied laser pulses.

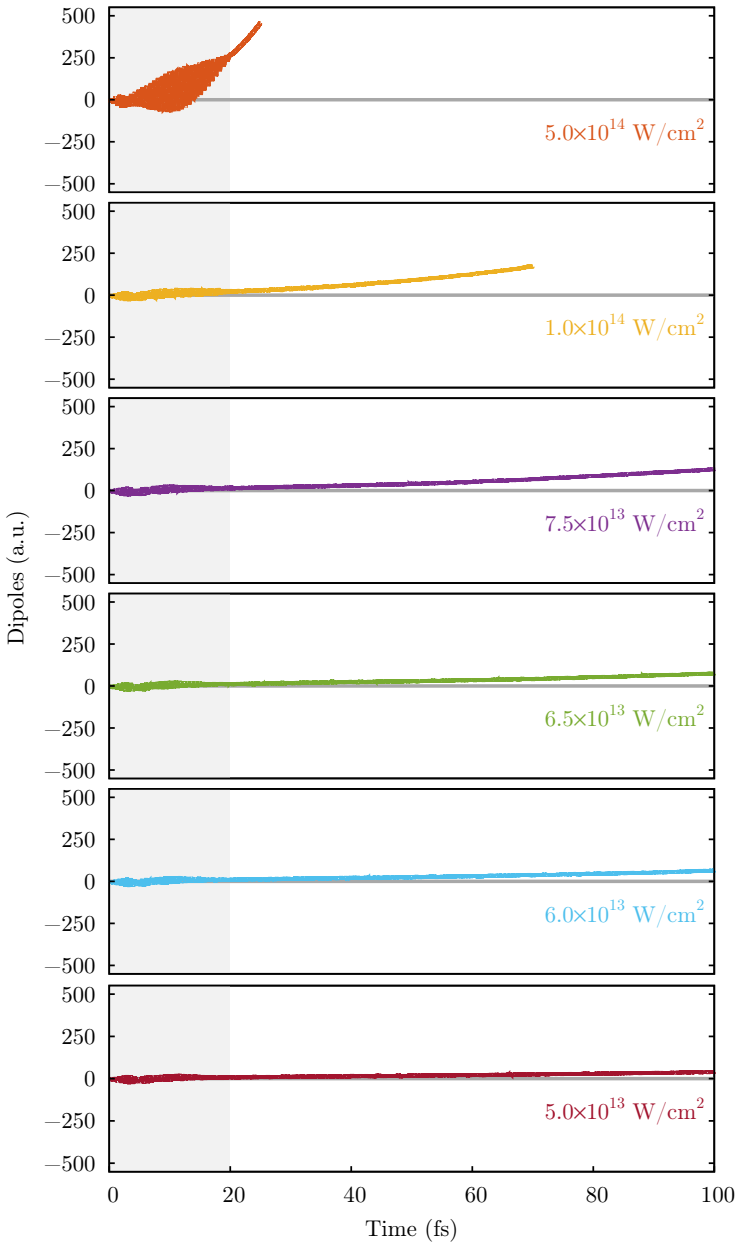

Figure 5.14: Time evolution of the dipoles along x-axis of the graphene nanoribon under different femtosecond laser irradiation.

So, as we stated above, during the simulation, only the purple-carbon atoms inside the black rectangle of Fig. 5.11 were allowed to move. In particular, in the bottom panel of Fig. 5.13 we plot the movement of the A-labeled atom through the x axis with respect to their equilibrium position in the ground state of the graphene nanoribbon. In our system this A-labeled atom should represent the most similar conditions to any atom in a periodic (or very large) graphene nanoribbon. It is worth noting here that when the system is perturbed by the weaker field (1×10^{12} W/cm^2) there is no ablation (See movies

online).

So through the entire evolution of the system, we computed the total forces acting on this atom from all the electrons, from the rest of the ions, as well as the total combined force from both the remaining ions and all electrons.

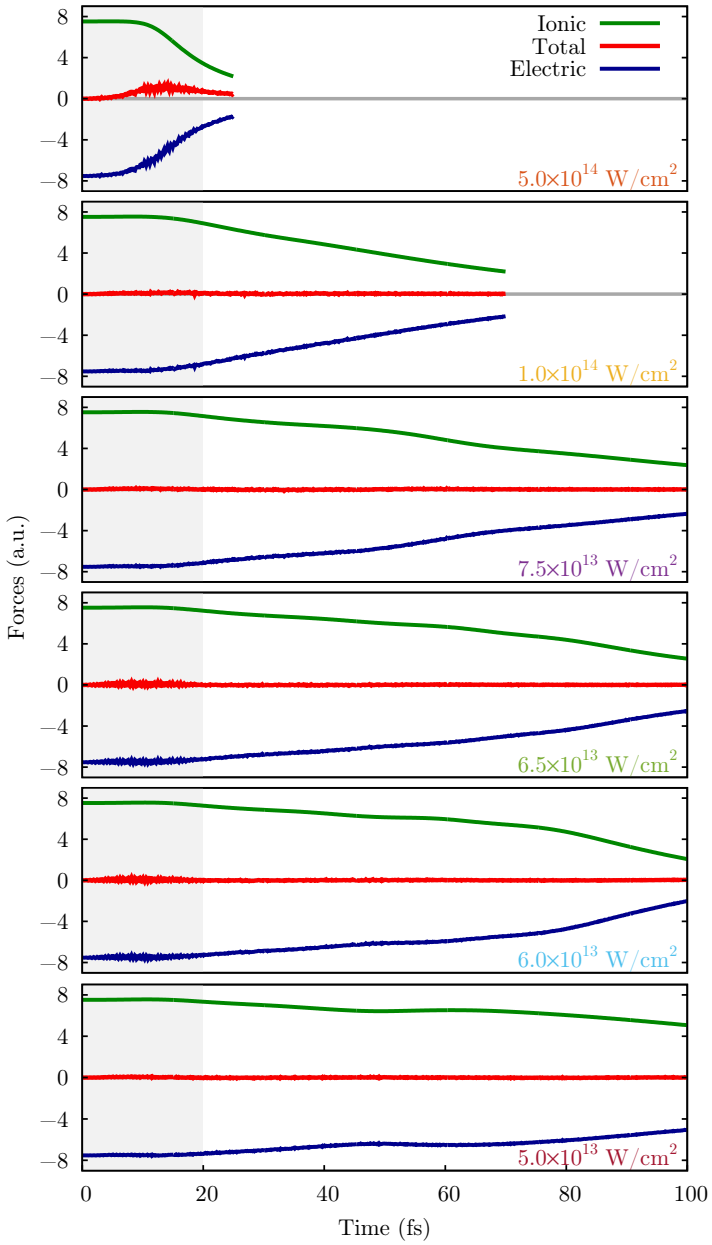

Figure 5.15: Time dependence of the total forces acting on the "A" atom from the rest of the ions, from all electrons, as well as the combined force from both the remaining ions and all electrons for the different laser pulses.

Figure 5.15 shows how in all the cases the ionic forces dominates over the electric ones. Being this a signal which indicates that if the A-labeled atom is removed from the sample,

then it is removed by a Coulomb Explosion mechanism. Furthermore, from the top and middle panel of Figure 5.13 it is possible to observe how during the first 10 fs of the simulation, the system have reached a maximum on the ionization rate (regardless of the intensity of the laser pulse), and during this time interval, being the system positively charged, the A-labeled atom almost has not moved from its equilibrium position, but it does from 10 fs onwards, confirming the Coulomb Explosion again. This can be observed on the online movies also.

Chapter 6

Anisotropy Effects on the Plasmonic Response of Nanoparticle Dimers[1]

6.1 Introduction

The resonant interaction of light with metallic nanostructures is at the heart of the developing field of nanoplasmonics. Recent advances in the fabrication and characterization of nanodevices have opened the possibility of tailoring plasmonic modes and, as a consequence, the response of nanosystems to external radiation [47–49]. From these advancements, a number of applications have been realized and/or proposed over the last few years, including optoelectronic hybrid devices [50, 51], optical nanoantennas [52], optical traps [53], nano-sensors [54–56], and broad-band light harvesting devices [57], among others.

Many properties of these nanodevices can be understood perfectly in terms of classical optics [4]. However, if one of the characteristic lengths of the system reaches the sub-nanometric scale, genuine quantum effects emerge in the optical response [48, 58], as has been observed over the last few years in a series of breakthrough experiments [59–63]. In this regime, the theoretical treatment of the electromagnetic response must include the

[1] This chapter is based on Ref. [233].

inhomogeneities of valence-electron densities and of photoinduced currents between the constituents of the device. Although there are some recent theoretical attempts aimed at incorporating such effects into the realm of classical optics [64, 65], in principle, the quantum behavior of both ground- state and light-induced densities should be explicitly treated to obtain reliable theoretical predictions.

A prototypical case is a system made up of two metallic nanoparticles with subnanometric separation. In this metallic nanodimer, the establishment of a photoinduced electric current between the particles dramatically changes the plasmonic modes of the system [66–68]. The main trends [69, 70] can be explained by describing the nanoparticles with the spherical jellium model in which the atomic structure is neglected, and by evaluating the optical response using the quantum mechanical time-dependent density functional theory (TDDFT) [71–74]. The latter provides the necessary accuracy when describing both the inhomogeneity of the electron density and the inherent nonlocality of the electromagnetic response. Thus, the combination of the jellium model and the TDDFT-based quantum treatment of light-matter interactions defines what is now considered to be state of the art in theoretical nanoplasmonics. Consequently, this approach has been applied to analyze the tunable response properties of nanorods [75], plasmonic cavities formed by nanowires [76–79], nanomatryushkas [80], and more recently, the optical properties of doped semiconductor nanocrystals [81]. Furthermore, the predictions of the jellium/TDDFT method can also be used to assess [76, 78] the capabilities of sophisticated refinements of classical optics [64, 65, 82–90], whose range of applicabilities is certainly broader because the numerical implementation of fully quantum methods is limited to systems containing up to thousands of atoms.

The widespread use of the jellium model when analyzing simple sp systems can be easily justified on the basis of the collective character of the plasmonic response. Moreover, the dynamical screening due to d electrons in noble-metal nanostructures can be mimicked by a dielectric background with an appropriate dielectric function [91]. Then, the atomic structure can be safely neglected in nanostructures made up of weakly interacting compact elements. However, this is not a valid approximation in systems like hybrid

nanoclusters [92], where the chemical composition of the nanoparticle is essential to understanding its optical properties. For strongly coupled nanostructures, we have recently shown that surface corrugation due to the atomic structure leads to induced near fields with spatial distributions and intensities that are fairly different than the ones obtained from the jellium model [234]. As mentioned previously, the electromagnetic response of a nanodimer is greatly affected by the induced current between the particles. Therefore, it is expected that the relative orientation of the nanoparticles, which leads to different atomic arrangements around the dimer junction, will have to be taken into account. Thus, a careful analysis is needed to quantify the actual role played by the anisotropy of the atomic structure in the establishment of induced photocurrents and to determine those regimes in which its description is relevant. These are the main objectives of this study.

6.2 Nanoparticle dimers

To achieve this goal, we analyzed the optical response of a prototype sodium nanocluster dimer. Each cluster is made up of 297 atoms in an icosahedral arrangement, which is the most stable configuration for isolated Na nanoparticles of this size [235](The relaxed atomic structure of the Na297 cluster is taken from the Cambridge Cluster Database, http://www-wales.ch.cam.ac.uk/ CCD.html.). As can be seen in Figure 6.1, the Na_{297} cluster is almost spherical with $2R \simeq 2.61$ nm being its effective diameter. This value corresponds to an average atomic density that is slighty larger than the one corresponding to bulk Na. The distance between the clusters is defined as $d = b - 2R$, where b is the distance between the central atoms of each cluster. Therefore, this definition does not depend on any atomic rearrangement in the gap region.

Once the distance d is fixed, there are two main features to consider: the relative orientation of the clusters and the atomic relaxation due to the mutual interaction. Concerning the relative orientation, in the present work, we treat the two cases depicted in Figure 6.1. The first leads to a spatial gap that is limited by two 12-atom faces (F2F orientation), whereas the second corresponds to a spatial gap between two 3-atom edges (E2E ori-

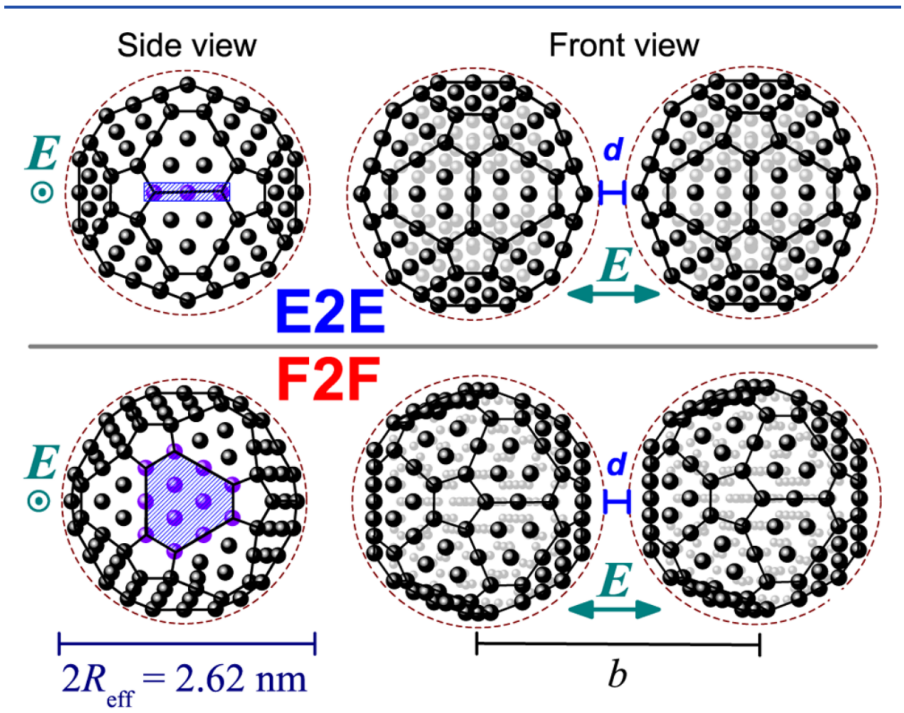

Figure 6.1: Representation of the two different geometrical arrangements of icosahedral Na_{297} dimers considered in the present study. In the edge-to-edge (E2E) relative orientation (upper panel), two 3-atom edges are faced. In the face-to-face (F2F) relative orientation (lower panel), the spacial gap is between two 12-atom faces. The applied electric field is orientated along the dimer axis.

entation). Thus, in the F2F geometry, we maximize the width of the dimer junction whereas the E2E configuration corresponds to a smaller separation between atoms. That is, there are two distinct effects (the distance between the nearest-neighbor atoms and the contact width) that tend to cancel out. Thus, we performed energy-optimized relaxation of the atomic positions in the E2E geometry, which is required due to the smaller distance between atoms. Such a relaxation obviously has to be restricted to the region around the spacial gap because the dimer itself is metastable: full relaxation would lead to coalescence of the two clusters.

Both energy optimization and ground-state calculations are performed under a real-space prescription of the density functional theory (DFT) Kohn-Sham equations [160] using the OCTOPUS package [185–188]. The explicit treatment of the 3s conduction electrons using norm-conserving pseudopotentials [196] suffices for the purposes of the present work. The relaxation is performed using the FIRE algorithm [192] recently implemented in OCTOPUS [188] under a semilocal approximation to the exchange-correlation (XC) functional.

Once the equilibrium geometries were obtained, ground-state electron densities, $n_0(r)$, were evaluated using the same prescription.

The TDDFT optical response was also calculated with OCTOPUS following the Yabana-Bertsch time-propagation recipe [184], which is very efficient in systems containing hundreds of atoms. At $t = 0$, the electron system was perturbed by a delta-kick electric field $E(r,t) = (\hbar\|_{,}/e)\delta(t)e_x$, where e is the absolute value of the electron charge, e_x is the direction of the dimer axis (i.e., the external field is oriented along the dimer junction), and $\|_0 = 0.005$ a.u. Then, all of the E1 selection-rule transitions were excited, and the induced density of a transition of frequency ω was directly related to the time-dependent density of the system after the kick, $n(r,t)$, though a Fourier transform

$$\delta n(r,t) = \int_0^{\infty} \delta n(r,t) e^{(i\omega-\gamma)t} \, , \tag{6.1}$$

$$\simeq \int_0^{T_{max}} \delta n(r,t) e^{(i\omega-\gamma)t} dt \, , \tag{6.2}$$

where $\delta n(r,t) = n(r,t) - n_0(r)$. Here, $\gamma = 0.1$ eV$/\hbar$ is a damping frequency that accounts for absorption spectra broadening due to nonelectronic losses, and T_{max} is the actual propagation time in the calculations. The absortion cross-section is then given by $\sigma_{abs}(\omega) = (\omega/c\epsilon_0) Im\alpha(\omega)$, where the dynamical polarizability $\alpha(\omega)$ is

$$\alpha(\omega) = -\frac{e^2}{\hbar k_0} \int x \delta n(r,\omega) dr \tag{6.3}$$

In practice, $\alpha(\omega)$ is evaluated from the Fourier transform of the kick-induced time-dependent dipole moment. Well-converged results are achieved using $T_{max} = 20$ fs, a propagation-time step of $\Delta t = 10^{-4} T_{max}$, and grid spacing of 0.026 nm.

6.3 Optical absorption

The dipole optical absorption of Na_{297} dimers in the $0 \leq d \leq 0.6$ nm range of separations is presented in Figure 6.2 for unrelaxed F2F and relaxed E2E geometries. For completeness,

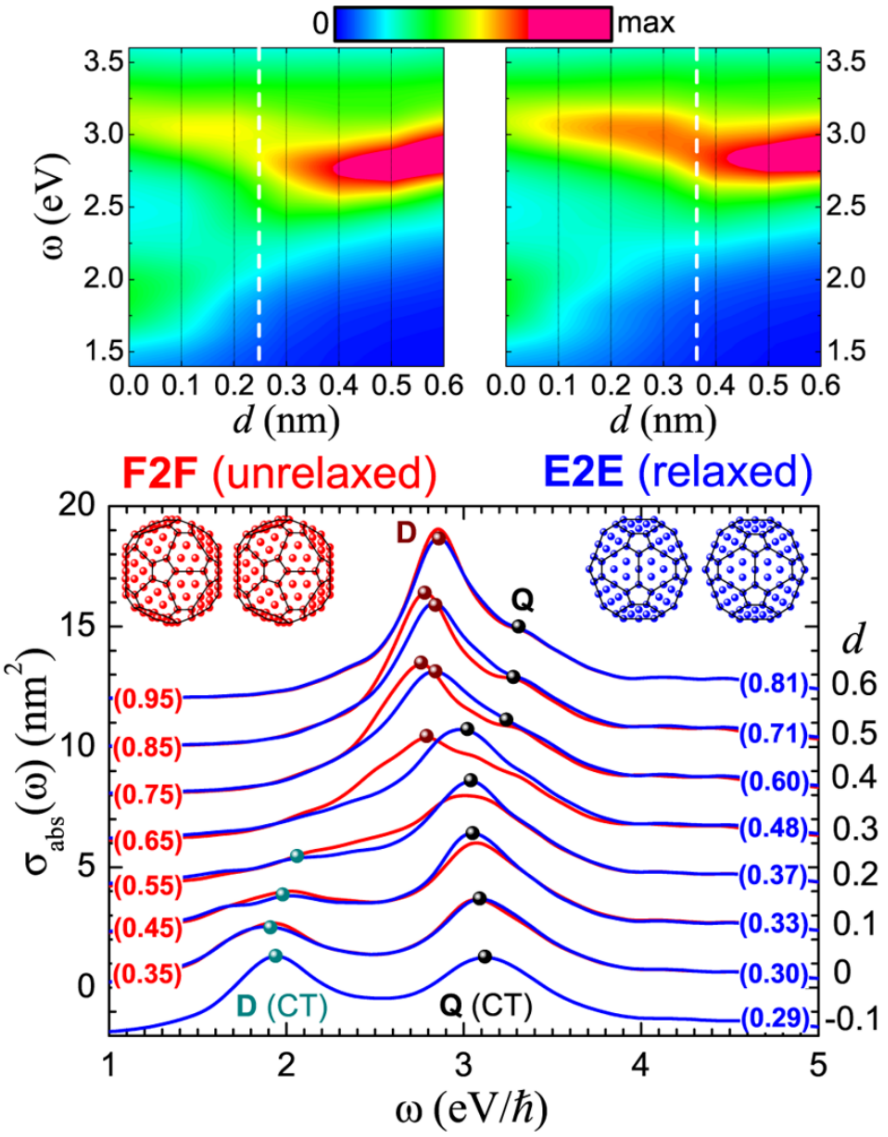

Figure 6.2: Optical absorption of Na_{297} dimers as a function of the distance d as defined in the text. Upper panels: contour plots of the photo-absorption cross sections, $\sigma_{abs}(\omega)$. The vertical dashed line indicates the approximate distance of where the hybridized Q mode becomes the main spectral feature in the spectrum. Lower panel: waterfall plot of the absorption cross sections. The red [blue] lines correspond to the F2F [relaxed E2E] relative orientations. For each distance, the separation in nm between faces [edges] is indicated in parentheses. The spectral peaks corresponding to coupled D, charge-transfer D and Q, and hybridized Q modes are indicated as well.

we have also included the optical absorption for the E2E overlapping clusters ($d = -0.1$ nm), where a major reconstruction of the junction occurs. We can define three distinct regimes: (a) $d \geq 0.6$ nm, where the interaction between clusters is mainly electromagnetic and the photoinduced charge transfer (CT) is very small; (b) $d \leq 0.1$ nm, where there is a direct overlap of the ground-state densities of each cluster because the Fermi level of the system is above the potential barrier in the dimer junction; and (c) 0.1 nm $< d <$ 0.6 nm, where tunnelling CT between the clusters appears as a result of a photoinduced voltage bias between the clusters.

As seen in Figure 6.2, there are marginal differences between the E2E and F2F optical spectra for the (a) and (b) separation regimes. The irrelevance of the relative orientation of the clusters in regime (a) is not at all a surprise because there are minor differences between the F2F absorption and the spherical jellium model even when $d = 0.5$ nm [234]. Furthermore, this is the regime in which the optical absorption can be explained well in classical terms, and it is also possible to have a quantitative agreement with the quantum predictions as long as the nonlocality of the electromagnetic response and the inhomogeneity associated with the electron-density spill-out in each nanoparticle are properly addressed. As is well known [66, 84, 178, 236, 237], the optical absorption in this regime is dominated by coupling between the Mie dipole-localized surface plasmon resonances (LSPRs) of the individual clusters. This coupled mode, in what follows labeled as D, is red-shifted with respect to the value $\omega_M = 3.13$ eV/$\hbar$ of the main Mie resonance of the isolated Na_{297} cluster [234]. In addition, a weak but discernible spectral feature appears at higher frequency. This is the signature of hybridized plasmon resonance (Q) due to excitation of the quadrupole LSPR of each cluster by the induced near field of the other.

As mentioned above, regime (b) corresponds to direct overlap of ground-state densities. In this limit, the two clusters cannot be consider as individual entities anymore and the system is actually a single "peanut-like" nanoparticle. The atomic arrangements in the junction and at the surfaces are very different in the F2F and E2E geometries, but such differences are blurred in the valence-electron density. As a consequence, the classically predicted sensitivity of the propagation of surface modes with respect to the surface

inhomogeneities [238] is no longer relevant. In this case, the spectrum is dominated by two LSPRs, labeled as D(CT) and Q(CT). In both resonances, there is a capacitive charge transfer between the two clusters (actually, between the two lobes of the peanut-shaped nanoparticle). In turn, these modes can also be characterized using classical optics if the actual ground-state density of the system is properly modeled [237, 239].

On the contrary, the importance of the relative orientation between the nanoparticles is manifested in regime (c), where the optical absorption of the dimer is the result of a delicate interplay of the electromagnetic interaction mediated by near fields and the appearance of a tunneling CT between the clusters. When $d \geq 0.4$ nm, the splitting of the D and Q modes in the F2F geometry is clearly visible. Furthermore, the frequency of the D mode decreases when approaching the clusters. Thus, the behavior of the F2F response can be described by classical electromagnetism despite the fact that there is charge transfer between the clusters as we will show below. For the E2E geometry, the value of the frequency of the D mode is already locked in this range of separations, and the transfer of spectral weight from the D mode to the hybridized Q mode is clearly reflected in the spectrum. Interestingly, the intensity of the tunneling current, ICT, when the D mode is excited is very similar in the F2F and E2E configurations. However, because the junction in the E2E orientation is substantially narrower than in the F2F one, the CT current density across the spatial gap is greater in the E2E case. As a consequence, propagation of the plasmonic density waves over the surface of the clusters is slightly altered by the tunneling CT in the F2F geometry, and the hybridization process follows the classically predicted trends. In fact, the quantum effects are only discernible in the F2F spectrum when the distance d is less than 0.4 nm. However, the E2E optical response is more sensitive to the establishment of an induced current, and we can say that the onset of quantum behavior due to tunneling is above $d = 0.5$ nm.

Within regime (c), the differences are more dramatic at smaller separations. In the F2F orientation at $d = 0.3$ nm, the D mode still dominates the spectrum, but the corresponding mode in the E2E geometry has already been quenched, and the main spectral feature comes from the hybridized Q mode. Nevertheless, this interpretation cannot be taken

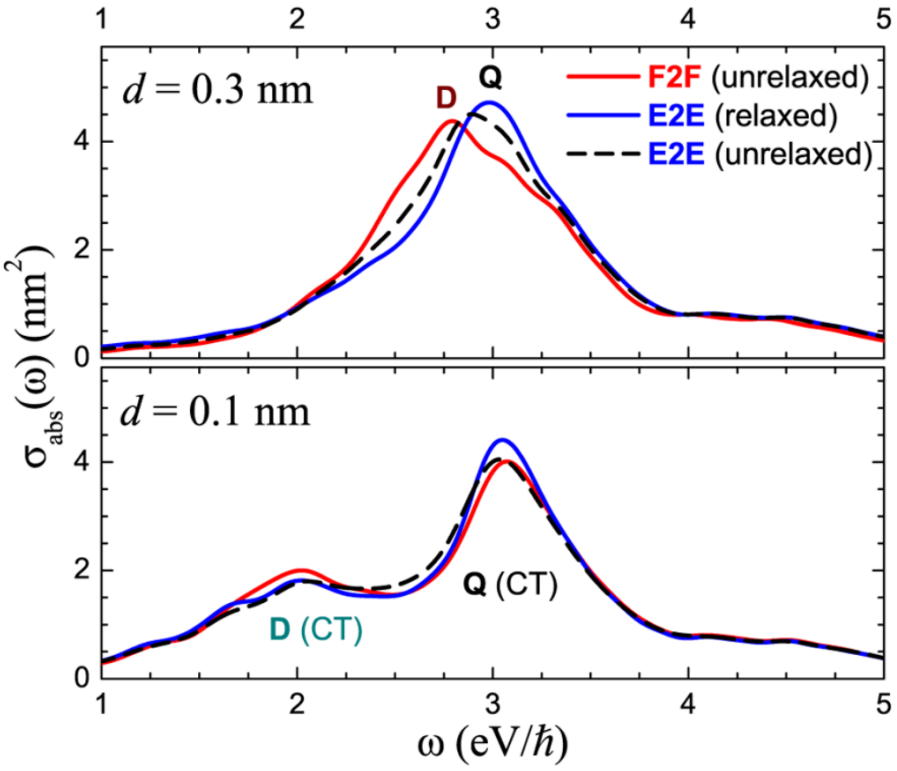

Figure 6.3: Impact of the atomic relaxation on the absorption cross sections for E2E Na_{297} dimers at separations of $d = 0.1$ and 0.3 nm. Optical absorption for relaxed geometries are the solid blue lines, and absorption for unrelaxed geometries are the dashed lines. For the sake of comparsion, the corresponding F2F spectra are also depicted (red solid lines).

literally because, unlike the well-defined classical plasmon modes, quantum collective excitations are the result of a coherent superposition of multiple electron-hole transitions, which cannot be isolated from other surrounding electron-hole pairs. In fact, the broad absorption range that characterizes both spectra at $d = 0.3$ nm is an admixture of the quantum collective excitations corresponding to the classical D and Q modes, electron-hole transitions, and likely other many-body collective excitations [240]. In any case, at $d = 0.3$ nm, the two spectra are qualitatively different, and such a difference will be even more evident when analyzing the driven-induced densities and currents. The spectral feature corresponding to the D mode in the F2F orientation finally vanishes when the separation is smaller than 0.3 nm, and the maximum absorption at $d = 0.2$ nm corresponds to the excitation of a Q mode for both geometries. Note that there is still reminiscence of the D mode excitation in the F2F spectrum around $\omega = 2.3$ eV/$\hbar$.

6.3.1 Impact of the atomic relaxation

We will now analyze the impact of atomic relaxation in the optical absorption. The corresponding reconstruction in the junction is negligible if the distance between nearest-neighbor atoms is > 0.6 nm and hardly noticeable in the range $0.5 - 0.6$ nm, which means that relaxation effects are expected to be significant if d ≤ 0.4 nm for the E2E geometry and ≤ 0.25 nm for the F2F configuration. For shorter distances, when the atomic densities of both clusters overlap, the atomic reconstruction itself will be noticeable. However, we have seen that, in this regime, the specific atomic arrangement is not a fundamental issue. Therefore, the atomic relaxation will play a role only in the range of critical distances in which there is a transition from a dominant D mode to a Q mode. To confirm and quantify this prediction, we compared the relaxed-E2E optical absorption considered so far with that of unrelaxed-E2E at $d = 0.1$ and 0.3 nm. This comparison is depicted in Figure 6.3 where, as expected, we see that atomic relaxation has a marginal impact on the optical response when $d = 0.1$ nm. At the critical distance $d = 0.3$ nm, the separation between the atoms is slightly greater in the unrelaxed configuration than in the relaxed one (0.51 and 0.48 nm, respectively). This small rearrangement does affect the absorption spectrum, because the intensity of the tunneling CT is weaker in the unrelaxed configuration. In any case, the changes are merely quantitative and less important than those related to the relative orientation, albeit they illustrate the sensitivity of the plasmonic response to the CT current intensity.

To gain further insights concerning the optical properties of the nanocluster dimers, we analyzed the electron dynamics at different resonant frequencies. Specifically, we looked at the induced densities, the current intensities between the clusters, and the total electric field (external plus induced) at the middle of the junction, $r = 0$. To carry out this study, we applied a weak uniform quasi-monochromatic laser pulse of mean frequency ω_{ext} over the system with duration $\tau = 20\pi/\omega_{ext}$ given by

$$E(t) = -E_0 \sin(\pi t/\tau) \cos(\omega_{ext} t) e_x \ , \tag{6.4}$$

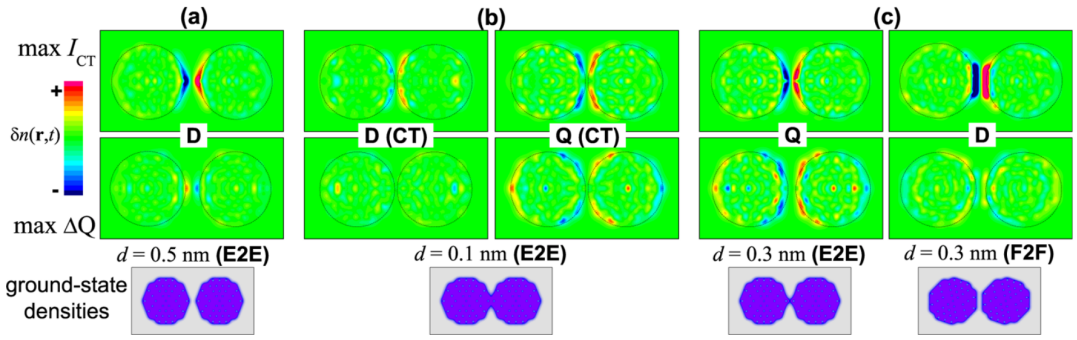

Figure 6.4: Snapshots of the induced electron densities at different resonant frequencies, as indicated in each panel. The top panels depict the induced densities when the current between the clusters reaches a maximum, whereas the second line corresponds to induced densities when the charge difference between clusters is maximum (zero intensity). The scale range is $-\rho \leq \delta n \leq \rho$, where $\rho = 0.5 \times 10^{-6}$ a.u. for $d = 0.1$ and 0.3 nm, whereas $\rho = 10^{-6}$ a.u. for $d = 0.5$ nm. A sketch of the corresponding ground-state electron densities is also shown to illustrate the different contact regimes.

where $E_0 = 10^{-6}$ a.u. $\simeq 0.51 \times 106$ Vm^{-1} is the maximum amplitude of the incident electric field. The maximum intensity of the laser pulse is 34.5 kW cm^{-2}, which is well below the onset of nonlinear effects.

In Figure 6.4, we depicted snapshots of the photoinduced densities in a plane containing the dimer axis for the following selected cases: (a) D mode at d = 0.5 nm (E2E, $\omega_{ext} = 2.83$ eV/$\hbar$), (b) D and Q modes at $d = 0.1$ nm (E2E, $\omega_{ext} = 2.01$ eV/$\hbar$ and $\omega_{ext} = 3.05$ eV/$\hbar$, respectively), (c) D mode (F2F, $\omega_{ext} = 2.79$ eV/$\hbar$) and Q mode (E2E, $\omega_{ext} = 3.00$ eV/$\hbar$)at $d = 0.3$ nm. In all of these cases, the relaxed atomic geometries were used for the E2E relative orientation. The snapshots were collected at times where the induced current is maximum (i.e., when the two clusters have the same charge) and where the induced current is close to a minimum (i.e., when the net charge of each cluster reaches its maximum absolute value).

Case (a) is representative of a coupled D mode (albeit very slightly altered by the appearance of a tunneling CT). The coupling between the dipole resonances of each cluster is reflected by a high concentration of oscillating-induced charges of opposite sign in the sides of the junction. As has been extensively analyzed using classical and quantum prescriptions, this distribution of charge is the primary reason for the high electric field enhancements that appear in this plasmonic cavity.

In case (b), we show direct CT modes. Although the overall shape of the driven densities

are partially obscured by the atomic corrugation, the different nature of the D and Q modes is evident. Also note that the induced densities are practically zero in the junction, which is in fair correspondence with the single-nanoparticle character of the system at this separation.

Finally, case (c) illustrates the sensitivity of the dynamical response to the atomic configuration in the critical regime in which the optical absorption is affected by photoinduced electron tunneling. The most relevant aspect is the difference between the E2E and F2F driven densities. The first can be assigned to a Q mode (compare with the corresponding Q mode at 0.1 nm), whereas the second has a shape closer to a D mode. Also note the different distributions of the induced densities around the spacial gap between the clusters.

6.4 Induced currents and electric field enhancement

In Figure 6.5, we display the time-evolution of the induced current, ICT, and the total electric field at the middle of the junction ($r = 0$) for the three cases discussed above. We have also included the induced current and field for the F2F configuration at $d = 0.5$ nm (D mode, $\omega_{ext} = 2.78$ eV/$\hbar$). It is worth emphasizing the overall delay in the response with respect to the applied field and the persistence of the induced currents and fields even when the external field has vanished, which are obvious signatures of resonant coupling. Non- electronic losses are not included in this calculation and, therefore, the decay of the driven modes can only occur via Landau fragmentation (i.e, though the formation of electron-hole pairs) [240–242]. Also note that the generation of hot electrons mediated by plasmon resonances is a very efficient mechanism that has important implications in heterogeneous catalysis, for instance [16]. In any case, the excitation of electron-hole pairs is the main damping mechanism of plasmons in nanoparticles of this size.

The electric fields at $r = 0$ for the two coupled D modes at $d = 0.5$ nm considered here (EFE and F2F) are very similar, although the field corresponding to the E2E geometry

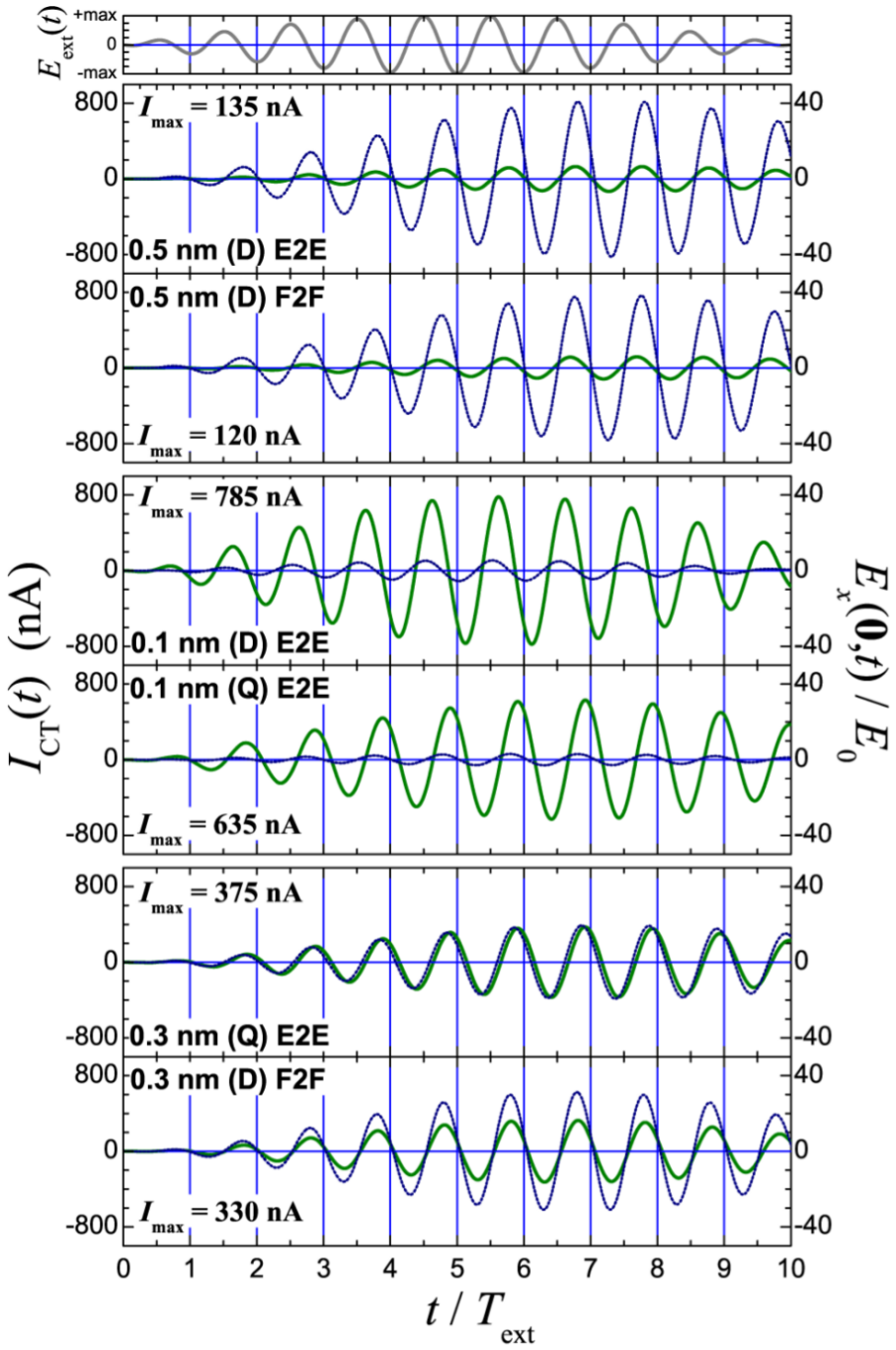

Figure 6.5: Time evolution of induced currents (solid green lines) and total electric fields (dotted blue lines) at the middle of the dimer junction ($r = 0$) due to the resonant coupling of selected modes of the nanoparticle dimer with an applied external field (depicted in the upper panel) of frequency ω_{ext}. In each panel, we indicate the maximum value of the induced intensity, ICT, corresponding to an incident electric field with maximum amplitude $E_0 = 10^{-6}$ a.u.

is slightly more intense. We can attribute this effect to the shorter atom-atom distance and also to the more angular profile of the induced density in the E2E configuration. On the other hand, fields and intensities practically oscillate in phase, correspond- ing to a resistive character of the junction. This behavior agrees with that obtained for the jellium nanocluster [70] and nanowire dimers [78]. Note the weak charge-transfer intensity (on the order of 100 nA) for the incident laser pulse given in Eq. 6.4.

Focusing on the direct CT regime, $d = 0.1$ nm, we must first note the different phase shifts of the oscillations of both the Q and D modes with respect to the applied field. Moreover, for both resonances, there is a relative phase between the induced current and the electric field in the center of the dimer with the intensity being delayed with respect to the total electric field. Again, this capacitive character of the resonance is in full agreement with previous findings for jellium systems [70, 78]. Although the optical absorption at the D mode is weaker than at the Q resonance (see Figure 6.1), the E field intensity is stronger in the D mode. Nevertheless, once the applied field fades out, the amplitudes of the D mode oscillations are quickly damped as expected from the wider corresponding peak in the absorption spectrum. Finally, in this regime, the charge-transfer intensity is approximately one order of magnitude larger than in the tunneling regime previously described (at touching distance, $d = 0$, the maximum charge-transfer intensity is 1600 nA).

In line with the previous discussion, there are quantitative differences between the E2E and F2F orientations in the intermediate distance regime $d = 0.3$ nm. The intensities of the driven currents are rather similar up to a small relative phase. However, the electric field in the E2E geometry is weaker than in the F2F orientation. This is not surprising because the dominant mode in the E2E geometry is the Q resonance. Remarkably, the intensity and the total E field oscillate in phase in the F2F dimer, thus indicating that the charge flows across a resistive junction. On the contrary, the E field and the current do not oscillate completely in phase in the E2E geometry. This is consistent with a weak capacitive behavior, which again can be traced back to the different atomic configurations in the junction.

6.5 Conclusions

In summary, we have presented a detailed study of the impact of the atomic configuration on the electromagnetic modes of prototypical metallic nanodimers when a charge transfer is established between the constituent clusters. Effect like atomic relaxation and different relative orientations, to date unexplored in quantum implementations of ab initio nanoplasmonics, have been explicitly addressed. Our findings confirm the accuracy of the jellium model, either in combination with quantum mechanical calculations or classical theories, except in the subnanometric separation regime in which the photoinduced tunnel current leads to changes in the optical properties of the system. This is precisely the regime where the most complicated processes occur. Thus, we have shown that accounting for the atomic structure of the junction (mainly the relative orientations between the faces) for very close nanoparticles is necessary to obtain theoretical results with enough predicitive power.

Although quantum TDDFT simulations can be applied to systems containing thousands of atoms, this is still too small for the sizes of many nanoparticles of technological interest. In these cases, the theoretical analyses aimed at helping in the design and characterization of novel nanodevices must necessarily be performed using either advanced prescriptions of the well-established classical electromagnetic theory [64, 65] or simplified TDDFT methods [146,243]. However, even in simple systems like the one analyzed in this work, there is a subtle interplay between induced near fields (which can be perfectly described classically using nonlocal optics) and induced tunnel charge transfers (which can be approximately accounted for using effective dielectric media [65]). Therefore, the present work provides a stringent playfield for the assessment of future refinements of semiclassical theories which, as we have noted, are much more amenable for the analysis of very complex structures than quantum ab initio methods. From a different perspective, the conclusions raised in this study pave the way for further explorations concerning fieldlike optoelectronics, nanosensing, and photoinduced catalysis in which the complexity of the light-matter interactions at the nano scale opens the possibility of a panoply of applications.

Chapter 7

Single atom induced effects on the plasmonic response of nanoparticle dimers

7.1 Introduction

The resonant interaction of light with metallic nanostructure has been attracting significant attention in the field of nanoplasmonics during the last years. One of the sources of this attention is the possibility of tailoring plasmonic modes and, as a consequence, the response of nanosystems to external radiation [47, 48]. In particular, tunnel junctions offers unique possibilities to tune these plasmonic modes due to the establisment of a photoinduced current through the nanogap. [66–68].

Among the possible tunnel junctions, single and multiple molecular junctions have received much recent interest due to the possibility to realize molecular-scale electronic components [51, 62, 244, 245]. On the other hand *vacuum* nanogaps have received its part of the attention due possibility of modify the tunneling conductance by changing the width of the gap [60, 61, 133].

The ultimate limit between *vacuum* nanogaps and molecular junctions, are nanogaps

bridged by single atoms. In the electronic research and industry, these nanogaps have received lot of consideration due the promise of high-speed, low power consumption and high density devices [246]. More recently, experimental-photonic research on these nanogaps have also received its part of attention, due to the posibility of control the interaction between photons and matter at the atomic scale [247–251], bringing with a bigger promise, the possibility of new opto-electronic devices for quantum information processing.

Even so, the theoretical photonic-research literature on nanogaps bridged by one single atoms is by far not as abundant as for their counterparts. Recently a few quantum-mechanical studies of plasmon excitation and plasmon-induced charge transport in an atomic tunnel junction consisting of single atoms sandwiched between two metal nanoparticles in a dimer configuration has been reported based on jellium models and time dependent density functional theory (TDDFT) [142, 252, 253]. On the other hand, the effects the atomic structure on the plasmonic response of metal nanoparticle dimers has been recently reported [142, 233, 234, 254, 255]. However, as far as our knowledge, there is no report on the optical response of a prototype sodium nanocluster dimer, considering the atomic details of the structure, bridged with a different sigle atoms.

7.2 Influence of the one-atom bridge

We analyzed the optical response of a sodium nanocluster dimer with different single atoms in between. Each cluster is made up of 297 atoms in an icosahedral arrangement, which is the most stable configuration for isolated Na nanoparticles of this size [235]. As can be seen in Figure 7.1, the Na_{297} cluster is almost spherical with $2R = 2.6$ nm being its effective diameter. This value corresponds to an average atomic density that is slighty larger than the one corresponding to bulk Na.

Ground-state calculations as well as optical response were performed under a real-space prescription of the density functional theory (DFT) Kohn–Sham equations [160] using the OCTOPUS code [185, 186, 188]. The explicit treatment of the conduction electrons

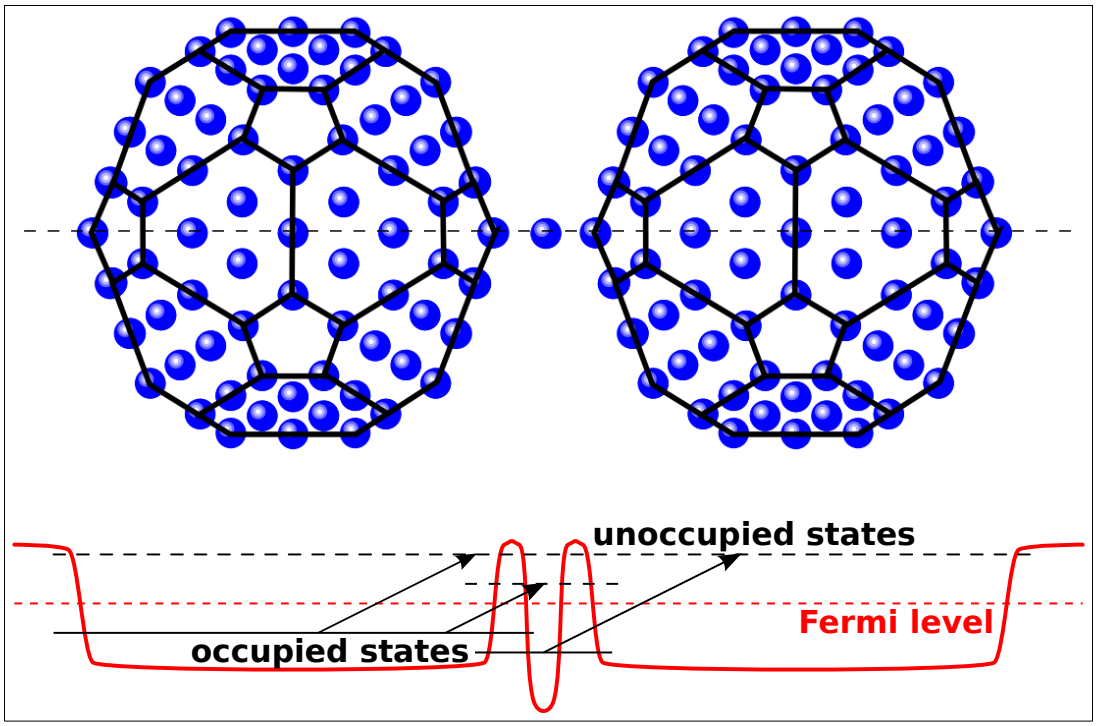

Figure 7.1: Representation of the geometrical arrengement of the icosahedral Na_{297} dimer bridged by one single atom.

using norm-conserving pseudopotentials [196] and under a semilocal approximation to the exchange-correlation functional, suffices for the purposes of the present work.

The dipole optical-absorption of each sysstem was obtained from a single time propagation following the Yabana-Bertsch recipe [184]. At $t = 0$ the system is perturbed by a small delta kick electric field $E(r, t) = (\hbar/ke)\delta(t)$ along the direction of the dimer axis, where e is the electron charge, and k is 0.005 a.u. Well-converged results are achieved using $T_{max} = 20$ fs, a propagation-time step of $\Delta t = 10^4$ T_{max}, and grid spacing of 0.026 nm.

As can be seen in Figure 7.2, the absorption spectrum in the 2–4 eV/$\hbar$ frequency range of the metal nanoparticle dimer, is affected by the inclusion of different single atoms between the two clusters. It is well known that in metallic nanoparticle dimers with subnanometric separations, the establishment of a photoinduced electric current between the particles, changes the plasmonic modes of the system [66–68], which has been more recently confirmed by fully TDDFT calculations, taking into account the details of the atomic structure [81, 233]. It is quite remarkable how similar are the spectra in the case of no atom bridging the two nanparticles, with the case were a Cl atom is in the middle

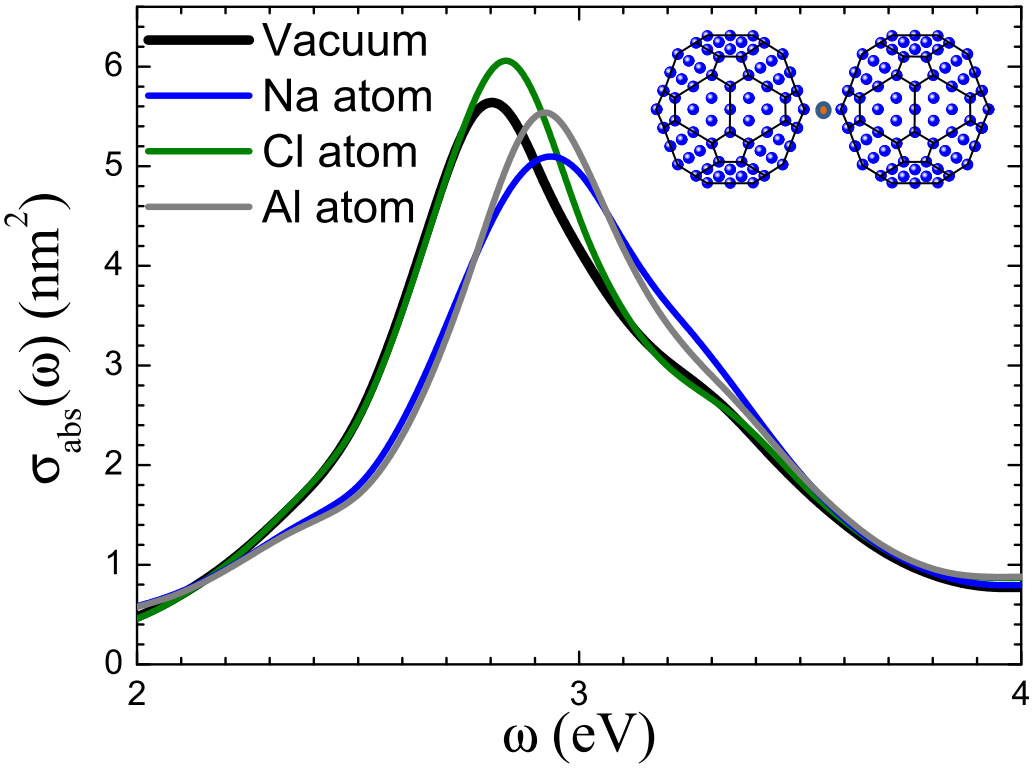

Figure 7.2: Absorption spectra of the metal nanoparticle dimer bridged with different single atoms in the 2–4 eV/$\hbar$ frequency range.

of the junction, slightly blueshifting the plasmon resonance peak in the later case with respect to the former one. The same kind of similarity is found in the case of the Na and Al atom bridging the nanparticles. This can be qualitatively understood in terms of the nature of the specific atom in the middle of the junction. When the Cl atom is bridging the two clusters, the photoinduced current is *blocked* be the central atom which try to *attract* electronic charge in order to close its shell. However when the Na or Al atom is the central one, the electronic charge of valence electrons tends to be *moved* through the nanoparticles by effect of the collective oscillations of the electronic charge in the system.

In the low frecuency range of the spectra (up to 2 eV/$\hbar$), as shown in Fig 7.3, depending on the added atom bridging the gap between the two clusters, the differences between the spectrum increase. If a Na or Al atom is in the middle of the junction, it is possible to identify a set of peaks emerging in this region. These resonances have been also observed in previous works analyzing the response of a nanoparticle dimer bridged with a sodium atom using jellium-TDDFT presciptions [252, 253], where these charge transfer modes are

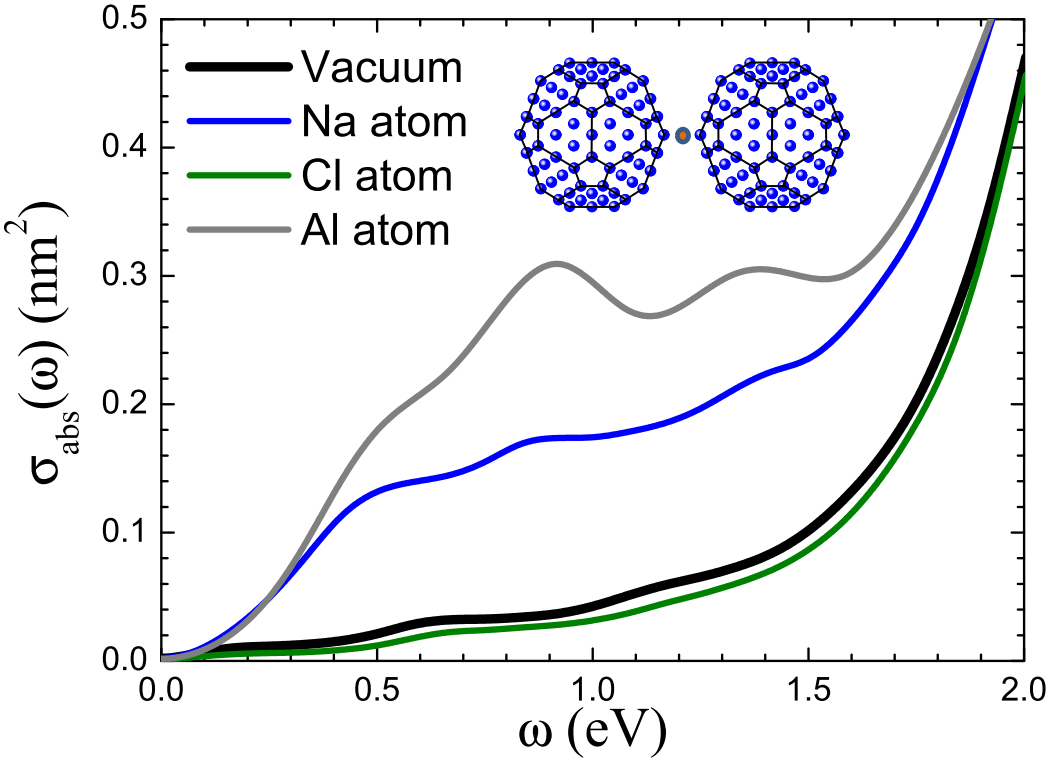

Figure 7.3: Absorption spectra of the metal nanoparticle dimer bridged with different single atoms in the 0–2 eV/$\hbar$ frequency range.

atributed to the resonance of one of the energy levels of the single atom with the Fermi level of the nanoparticles. However, this is the first time that these resonances have been observed by fully ab-initio calculations taking into account the atomic structure. On the other hand, when the Cl atom is bridging the junction, or when there is no atom in between the clusters, it is quite difficult to recognize this resonance modes in the absoption spectra, being both spectrum strikingly similar between them. This similarity match remarkably well with the explanation stated above, due there is no resonance between the energy levels of the Cl atom with the Fermy energy of the nanoparticle dimer in this frequency range.

As expected, this resonances are reflected on the intensity across the plane that separates the two clusters, perpendicular to the dimer axis, as shown in Figure 7.4. Again, as in the case of the absorption spectra, our results of the photoinduced current in the junction with and without the Na atom agree cualitatively well with the jellium/TDDFT the results reported by Song *et al.* [252].

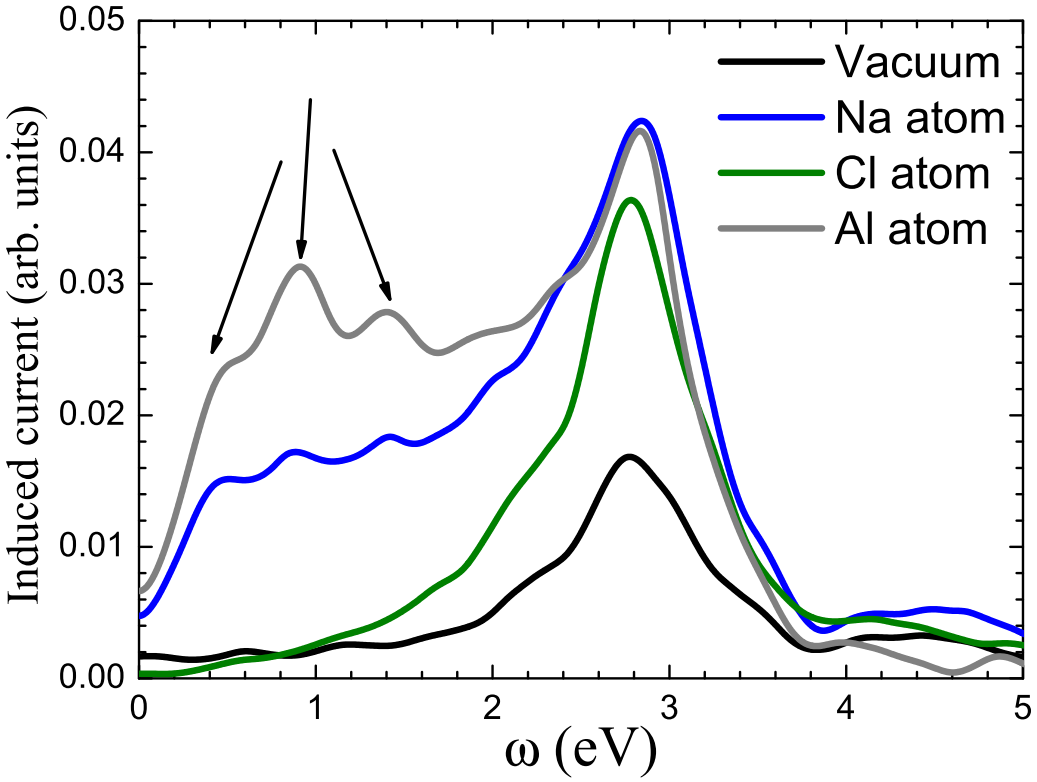

Figure 7.4: Intensity of the photoinduced current in the junction of the metal nanoparticle dimer bridged with different single atoms in the 0–4 eV/$\hbar$ frequency range.

Figure 7.5 show the calculated energy different cluster dimers. As an example, the electronic density of of some of the electronic states are also plotted in the case of a Fe-atom bridging the two clusters. The hybridization of some electronic states of the clusters with electronic states of the central atom are responsible for the charge transfer plasmons, and hence for the transmission between the two clusters.

7.3 Conclusions

In conclusion, we have presented a fully ab-initio TDDFT study on the plasmonic response of Na nanoparticle dimers bridged by different single atoms, considering the atomic structure of the system. Our finding confirm qualitatively the accuracy of jellium/TDDFT models in the case where a Na atom is bridging the clusters as well as in the case where there is no atom in the junction. However we provide new details of the resonances depending on the single atom bridging the junction. We have show how the changes in the

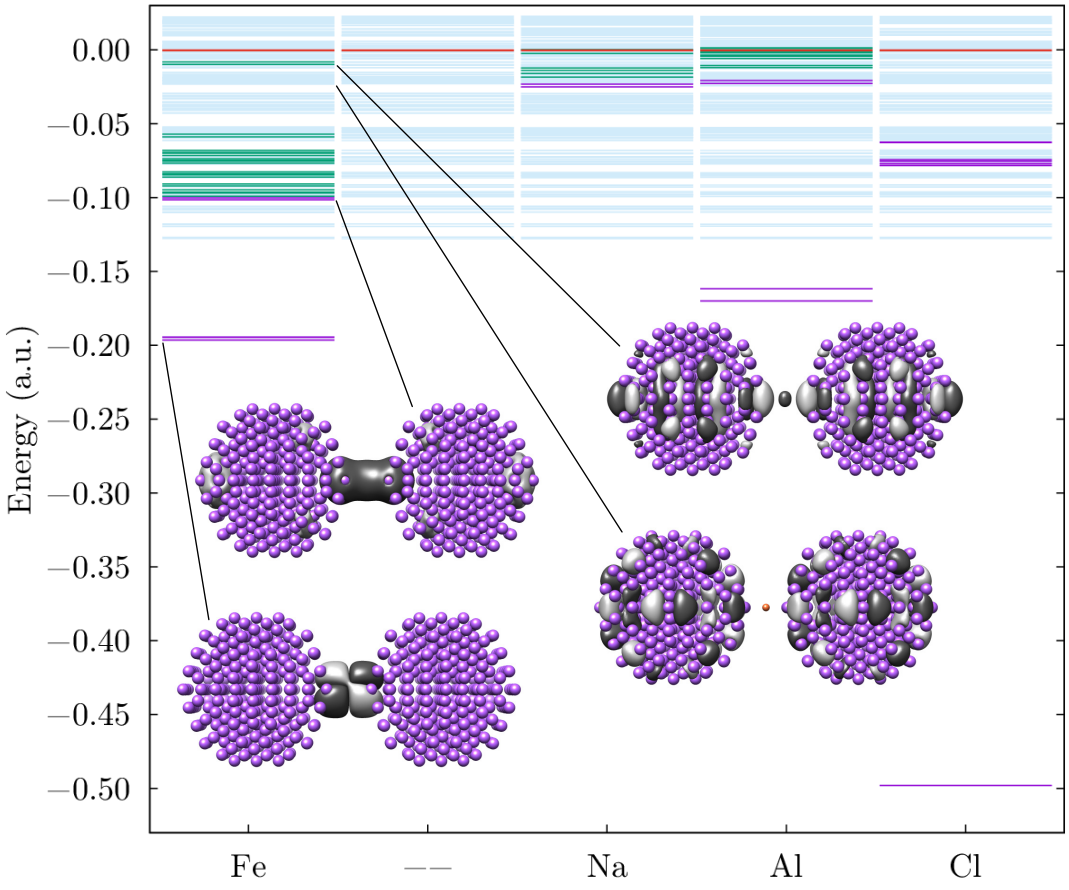

Figure 7.5: Energy levels of the different cluster-atom-cluster systems.

optical properties of the system depend strongly on the single atom junction, which is able to either hinder or facilitate the photoinduced current between the clusters, specially in the low-energy regime. This low energy mode would be active in coupling to molecular vibrations and may have promising application in plasmon enhanced catalytic reactions. The control of various parameters, such as dimer radius, separation, type of molecules, and dielectric environment would offer us unique ways to tune the photoinduced conduction and plasmon-electron coupling in molecular junctions and other plasmonic structures.

Chapter 8

Conclusions

In this thesis, we have addressed the modeling of different linear and non-linear interaction processes between electromagnetic radiation and low-dimensional nanostructures to simulate particular physical phenomena based on nanoplasmonics. Depending on the length scale of the system to be modeled, we have used different techniques, ranging from classical to atomistic ab-initio methods.

In chapter 3 we performed classical simulations in the framework of the discrete dipole approximation model to fit the experimental NIR absorption spectra of non-stoichiometric mixed-phase $Cu2-xS$ nanocrystals disolved in $CHCl_3$, recently synthesized by a collaborative research group. The experimental data was fitted through a multi-dimensional scan of the Drude-Lorentz parameters for the dielectric function, considering all the phases/samples simultaneously. As recent works has been highlighted that the modeling of the bulk dielectric function for nonstoichiometric $Cu_{2-x}S$ phases on the basis of the Drude model, may not be the most suitable, as the carriers supporting the plasmon resonance can experience a certain degree of localization, we proceed to overcome this limitation by modeling the dielectric function under the Drude-Lorentz prescription, adding a Lorentzian terms to the Drude dielectric function to take into account localized carriers or interband transitions. However, in our calculations, the best agreement between the DDA-calculated and the experimental spectra was found in the Drude-only model for all

the mixed-phase samples.

Through the analisys of our calculations, we were able to obtain the plasma frequency of each mixed-phase nanocrystal and from there to obtain theoretically their carrier densities, confirming the previously reported metallic-like character of the covellite, as well as the one of digenite, and and even low-chalcocite, which is in between the frontier of metallic and heavily doped semiconductor.

Regarding the decomposition of the optical response in LSPRs excited by in-plane and out-of-plane polarized incident light, all contributions can be hardly discriminated in the averaged spectrum, which is dominated by in-plane dipolar LSPRs. As a conclusion, despite the rather small aspect ratio of the mixed-phase samples, a careful theoretical analysis of the absorption spectra clearly demonstrates the shape-dependence of the LSPRs in the plasmonic covellite, digenite, and low chalcocite phases.

In chapter 4 we performed classical and semiclassical calculations, within the frame of the DDA, Mie-Gans Theory, and finite element method with the aim of sheed light on the unique structural-optical properties of recently synthesized (by a collaborative research group) nonstoichiometric $WO3 - \delta$ nanostructures of hemitubular morphology, which experimentally show tunable NIR to mid-IR plasmon resonances, essentially dependent on their aspect ratio.

The comparison between experimental and numerical DDA results for different samples show a very good overall agreement between experiment and theory. From our analysis we conclude thet the vis-IR optical spectra are dominated by a broad but intense peak whose position depends very sensitively on geometry of the sample. A second and much weaker spectral feature, which only emerges as a discernible shoulder in the spectra for the longest hemitubes, appears around $\lambda \sim 700$ nm for all the samples. The lower-energy peak can be attributed to a localized surface plasmon (LSP) associated to collective oscillations of the conduction electrons along the hemitube axis. On the contrary, the higher-energy feature corresponds to LSPs where the electrons mainly oscillate in the direction perpendicular to the hemitube axis (perpendicular modes) to such collective excitations. Therefore,

the maxima of the experimental absorption can be assigned (up to a small error) to the frequency of the axial mode. Furthermore, the existence of different length scales (length, width, wall thickness) of the hemitubes is reflected on the calculated near-field enhancement patterns.

In chapter 5, and motivated by a collaboration with an experimental research group (different from the one of the chapters 3 and 4), we have modeled the laser ablation processes in low-dimensional nanostructures, driven by intense and ultrashort laser pulses (in the plasmon resonance regime). Through these simulations, we have analyzed if Coulomb Explosion or electrostatic ablation is the mechanism of material removal in the early stage of the gentle ablation regime. All the simulations in this chapter were performed at an ab-initio level by using TDDFT coupled with standard Ehrenfest dynamics in the Octopus code. In order to obtain insights on which is the mechanism of ablation in the gentle-ablation regime, we proceed in a kind of botton-up way, performing simulations from a 0-dimensional system: a Li_4 cluster, to a 2-dimensional system: a graphene nanoribon. In both cases, different laser pulses (intensities) at frequencies close to the resonance of each system were applied, and in order to control for the laser ablation process during the simulations some atoms were allowed to move freely while others were clamped. Through the entire evolution of the simulations, we computed total forces acting on the free atoms from all the electrons and from the rest of the ions. From the analissys of these calculations we observe how in all the cases the ionic forces dominates over the electric ones. Being this a signal which indicates that if the free atom is removed from the sample, then it is removed by a Coulomb Explosion mechanism.

In chapter 6 we have performed fully atomistic ab-initio simulations on metal cluster dimers to study the anisotropy effects of the plasmonic response of this nanostructures. All the simulations in this chapter were performed at an ab-initio level by using TDDFT in the Octopus code. Specifically, effects like atomic relaxation and different relative orientations, to date unexplored in quantum implementations of ab initio nanoplasmonics, have been explicitly addressed, including the electric field enhancement and the photoinduced current. We have shown that accounting for the atomic structure of the junction

(mainly the relative orientations between the faces) for very close nanoparticles is necessary to obtain theoretical results with enough predicitive power, providing a stringent playfield for the assessment of future refinements of semiclassical theories. From a different perspective, this work, pave the way for further explorations concerning fieldlike optoelectronics, nanosensing, and photoinduced catalysis in which the complexity of the light-matter interactions at the nano scale opens the possibility of a panoply of applications.

In this context, and finally, in chapter 4 we studied how the influence of a one-atom junction between the two atomic conformations affect the electromagnetic modes of prototypical metallic nanodimers when a charge transfer is established between the constituent clusters. From the theoretical analisys of our simulations it is possible to infer that the charge transfer plasmons, and hence the transmission observed in the absorption spectrum of the system is driven by a resonant excitation between a hybridized atomic state and an atomic state of the clusters.

Bibliography

[1] Hornyak, G. L., Tibbals, H., Dutta, J. & Moore, J. J. *Introduction to Nanoscience and Nanotechnology* (CRC Press, 2008).

[2] Haus, J. W. *Fundamentals and applications of nanophotonics* (2016). URL `http://www.sciencedirect.com/science/book/9781782424642`.

[3] Bohren, C. F. & Huffman, D. R. *Absorption and Scattering of Light by Small Particles* (Wiley-VCH, 1983).

[4] Maier, S. A. *Plasmonics: Fundamentals and Applications* (Springer US, 2007). URL `http://dx.doi.org/10.1007/0-387-37825-1`.

[5] Wokaun, A. Surface enhancement of optical fields. *Molecular Physics* **56**, 1–33 (1985). URL `http://dx.doi.org/10.1080/00268978500102131`.

[6] de Aberasturi, D. J., Serrano-Montes, A. B. & Liz-MarzÃ¡n, L. M. Modern applications of plasmonic nanoparticles: From energy to health. *Advanced Optical Materials* **3**, 602–617 (2015). URL `http://dx.doi.org/10.1002/adom.201500053`.

[7] Jain, P. K., El-Sayed, I. H. & El-Sayed, M. A. Au nanoparticles target cancer. *Nano Today* **2**, 18–29 (2007). URL `http://www.sciencedirect.com/science/article/pii/S1748013207700166`.

[8] Jain, P. K., Huang, X., El-Sayed, I. H. & El-Sayed, M. A. Noble metals on the nanoscale: Optical and photothermal properties and some applications in imaging, sensing, biology, and medicine. *Accounts of Chemical Research* **41**, 1578–1586 (2008). URL `http://dx.doi.org/10.1021/ar7002804`.

[9] Webb, J. A. & Bardhan, R. Emerging advances in nanomedicine with engineered gold nanostructures. *Nanoscale* **6**, 2502–2530 (2014). URL http://dx.doi.org/10.1039/C3NR05112A.

[10] Jain, P. K., Huang, X., El-Sayed, I. H. & El-Sayed, M. A. Review of some interesting surface plasmon resonance-enhanced properties of noble metal nanoparticles and their applications to biosystems. *Plasmonics* **2**, 107–118 (2007). URL http://dx.doi.org/10.1007/s11468-007-9031-1.

[11] Anker, J. N. *et al.* Biosensing with plasmonic nanosensors. *Nat Mater* **7**, 442–453 (2008). URL http://dx.doi.org/10.1038/nmat2162.

[12] Zijlstra, P., Paulo, P. M. R. & Orrit, M. Optical detection of single non-absorbing molecules using the surface plasmon resonance of a gold nanorod. *Nat Nano* **7**, 379–382 (2012). URL http://dx.doi.org/10.1038/nnano.2012.51.

[13] Atwater, H. A. & Polman, A. Plasmonics for improved photovoltaic devices. *Nat Mater* **9**, 865–865 (2010). URL http://dx.doi.org/10.1038/nmat2866.

[14] Kim, I. *et al.* Metal nanoparticle plasmon-enhanced light-harvesting in a photosystem i thin film. *Nano Letters* **11**, 3091–3098 (2011). URL http://dx.doi.org/10.1021/nl2010109.

[15] Ye, W., Long, R., Huang, H. & Xiong, Y. Plasmonic nanostructures in solar energy conversion. *J. Mater. Chem. C* **5**, 1008–1021 (2017). URL http://dx.doi.org/10.1039/C6TC04847A.

[16] Mukherjee, S. *et al.* Hot electrons do the impossible: Plasmon-induced dissociation of h2 on au. *Nano Letters* **13**, 240–247 (2013). URL http://dx.doi.org/10.1021/nl303940z.

[17] Baba, K. & Miyagi, M. Optical polarizer using anisotropic metallic island films with a large aperture and a high extinction ratio. *Opt. Lett.* **16**, 964–966 (1991). URL http://ol.osa.org/abstract.cfm?URI=ol-16-12-964.

[18] Grupp, D. E., Lezec, H. J., Ebbesen, T. W., Pellerin, K. M. & Thio, T. Crucial role of metal surface in enhanced transmission through subwavelength apertures. *Applied Physics Letters* **77**, 1569–1571 (2000). URL http://dx.doi.org/10.1063/1.1308530.

[19] Barnes, W. L., Dereux, A. & Ebbesen, T. W. Surface plasmon subwavelength optics. *Nature* **424**, 824–830 (2003). URL http://dx.doi.org/10.1038/nature01937.

[20] Kreibig, U. *Optical Properties of Metal Clusters* (Springer-Verlag Berlin Heidelberg, 1995). URL http://dx.doi.org/978-3-662-09109-8.

[21] Lakowicz, J. R. Radiative decay engineering: Biophysical and biomedical applications. *Analytical Biochemistry* **298**, 1–24 (2001). URL http://www.sciencedirect.com/science/article/pii/S0003269701953771.

[22] Lakowicz, J. R. *et al.* Radiative decay engineering. *Analytical Biochemistry* **301**, 261–277 (2002). URL http://www.sciencedirect.com/science/article/pii/S0003269701955034.

[23] Gao, H., Henzie, J. & Odom, T. W. Direct evidence for surface plasmon-mediated enhanced light transmission through metallic nanohole arrays. *Nano Letters* **6**, 2104–2108 (2006). URL http://dx.doi.org/10.1021/nl061670r. PMID: 16968034.

[24] Zijlstra, P., Chon, J. W. M. & Gu, M. Five-dimensional optical recording mediated by surface plasmons in gold nanorods. *Nature* **459**, 410–413 (2009). URL http://dx.doi.org/10.1038/nature08053.

[25] Hutter, E. & Fendler, J. Exploitation of localized surface plasmon resonance. *Advanced Materials* **16**, 1685–1706 (2004). URL http://dx.doi.org/10.1002/adma.200400271.

[26] Pastoriza-Santos, I., SÃ¡nchez-Iglesias, A., RodrÃguez-GonzÃ¡lez, B. & Liz-MarzÃ¡n, L. M. Aerobic synthesis of cu nanoplates with intense plasmon resonances. *Small* **5**, 440–443 (2009). URL http://dx.doi.org/10.1002/smll.200801088.

[27] Knight, M. W. *et al.* Aluminum for plasmonics. *ACS Nano* **8**, 834–840 (2014). URL http://dx.doi.org/10.1021/nn405495q. PMID: 24274662.

[28] Scotognella, F. *et al.* Plasmonics in heavily-doped semiconductor nanocrystals. *The European Physical Journal B* **86**, 154 (2013). URL http://dx.doi.org/10.1140/epjb/e2013-40039-x.

[29] Zhao, Y. *et al.* Plasmonic $cu_{2-x}s$ nanocrystals: Optical and structural properties of copper-deficient copper(i) sulfides. *Journal of the American Chemical Society* **131**, 4253–4261 (2009). URL http://dx.doi.org/10.1021/ja805655b.

[30] Luther, J. M., Jain, P. K., Ewers, T. & Alivisatos, A. P. Localized surface plasmon resonances arising from free carriers in doped quantum dots. *Nature materials* **10**, 361–6 (2011). URL http://dx.doi.org/10.1038/nmat3004.

[31] Kanehara, M., Koike, H., Yoshinaga, T. & Teranishi, T. Indium tin oxide nanoparticles with compositionally tunable surface plasmon resonance frequencies in the near-ir region. *Journal of the American Chemical Society* **131**, 17736–17737 (2009). URL http://dx.doi.org/10.1021/ja9064415.

[32] Liu, X. & Swihart, M. T. Heavily-doped colloidal semiconductor and metal oxide nanocrystals: an emerging new class of plasmonic nanomaterials. *Chem. Soc. Rev.* **43**, 3908–3920 (2014). URL http://dx.doi.org/10.1039/C3CS60417A.

[33] Comin, A. & Manna, L. New materials for tunable plasmonic colloidal nanocrystals. *Chem. Soc. Rev.* **43**, 3957–3975 (2014). URL http://dx.doi.org/10.1039/C3CS60265F.

[34] García de Abajo, F. J. Graphene plasmonics: Challenges and opportunities. *ACS Photonics* **1**, 135–152 (2014). URL http://dx.doi.org/10.1021/ph400147y.

[35] Boltasseva, A. & Atwater, H. A. Low-loss plasmonic metamaterials. *Science* **331**, 290–291 (2011). URL http://science.sciencemag.org/content/331/6015/290. http://science.sciencemag.org/content/331/6015/290.full.pdf.

[36] Manthiram, K. & Alivisatos, A. P. Tunable localized surface plasmon resonances in tungsten oxide nanocrystals. *Journal of the American Chemical Society* **134**, 3995–3998 (2012). URL http://dx.doi.org/10.1021/ja211363w.

[37] Xie, Y. *et al.* Metallic-like stoichiometric copper sulfide nanocrystals: Phase- and shape-selective synthesis, near-infrared surface plasmon resonance properties, and their modeling. *ACS Nano* **7**, 7352–7369 (2013). URL http://pubs.acs.org/doi/abs/10.1021/nn403035s.

[38] Wang, Y. *et al.* One-pot synthesis and optical property of copper(i) sulfide nanodisks. *Inorganic Chemistry* **49**, 6601–6608 (2010). URL http://dx.doi.org/10.1021/ic100473e. PMID: 20575563, http://dx.doi.org/10.1021/ic100473e.

[39] Hsu, S.-W., Bryks, W. & Tao, A. R. Effects of carrier density and shape on the localized surface plasmon resonances of $cu_{2-x}s$ nanodisks. *Chemistry of Materials* **24**, 3765–3771 (2012). URL http://pubs.acs.org/doi/abs/10.1021/cm302363x. http://pubs.acs.org/doi/pdf/10.1021/cm302363x.

[40] Dorfs, D. *et al.* Reversible tunability of the near-infrared valence band plasmon resonance in $cu_{2-x}se$ nanocrystals. *Journal of the American Chemical Society* **133**, 11175–11180 (2011). URL http://dx.doi.org/10.1021/ja2016284. PMID: 21728384.

[41] Kriegel, I. *et al.* Shedding light on vacancy-doped copper chalcogenides: Shape-controlled synthesis, optical properties, and modeling of copper telluride nanocrystals with near-infrared plasmon resonances. *ACS Nano* **7**, 4367–4377 (2013). URL http://pubs.acs.org/doi/abs/10.1021/nn400894d.

[42] Hsu, S.-W., On, K. & Tao, A. R. Localized surface plasmon resonances of anisotropic semiconductor nanocrystals. *Journal of the American Chemical Society* **133**, 19072–19075 (2011). URL http://pubs.acs.org/doi/abs/10.1021/ja2089876. http://pubs.acs.org/doi/pdf/10.1021/ja2089876.

[43] Goodenough, J. B. Metallic oxides. *Progress in solid state chemistry* **5**, 145–399 (1971).

[44] Shi, S. *et al.* Low-temperature synthesis and electrical transport properties of $w_{18}o_{49}$ nanowires. *Journal of Crystal Growth* **310**, 462–466 (2008). URL http://www.sciencedirect.com/science/article/pii/S0022024807008858.

[45] Su, C.-Y. & Lin, H.-C. Direct route to tungsten oxide nanorod bundles: Microstructures and electro-optical properties. *The Journal of Physical Chemistry C* **113**, 4042–4046 (2009). URL http://dx.doi.org/10.1021/jp809458j.

[46] RemÅ¡kar, M. *et al.* W5o14 nanowires. *Advanced Functional Materials* **17**, 1974–1978 (2007). URL http://dx.doi.org/10.1002/adfm.200601150.

[47] Schuller, J. A. *et al.* Plasmonic for extreme light cocentration and manipulation. *Nature Materials* **9**, 193–204 (2010). URL http://dx.doi.org/10.1038/nmat2630.

[48] Halas, N. J., Lal, S., Chang, W.-S., Link, S. & Nordlander, P. Plasmons in strongly coupled metallic nanostructures. *Chemical Reviews* **111**, 3913–3961 (2011). URL http://dx.doi.org/10.1021/cr200061k.

[49] Gray, S. K. Theory and modeling of plasmonic structures. *The Journal of Physical Chemistry C* **117**, 1983–1994 (2013). URL http://dx.doi.org/10.1021/jp309664c. http://dx.doi.org/10.1021/jp309664c.

[50] Ward, D. R., Huser, F., Pauly, F., Cuevas, J. C. & Natelson, D. Optical rectification and field enhancement in a plasmonic nanogap. *Nat Nano* **5**, 732–736 (2010). URL http://dx.doi.org/10.1038/nnano.2010.176.

[51] Galperin, M. & Nitzan, A. Molecular optoelectronics: the interaction of molecular conduction junctions with light. *Physical chemistry chemical physics : PCCP* **14**, 9421–38 (2012). URL http://pubs.rsc.org/en/content/articlehtml/2012/cp/c2cp40636e.

[52] Mühlschlegel, P., Eisler, H.-J., Martin, O. J. F., Hecht, B. & Pohl, D. W. Resonant optical antennas. *Science* **308**, 1607–1609 (2005). URL http://science.

sciencemag.org/content/308/5728/1607. http://science.sciencemag.org/content/308/5728/1607.full.pdf.

[53] Tsuboi, Y. *et al.* Optical trapping of quantum dots based on gap-mode-excitation of localized surface plasmon. *The Journal of Physical Chemistry Letters* **1**, 2327–2333 (2010). URL http://dx.doi.org/10.1021/jz100659x.

[54] Xu, H., Bjerneld, E. J., Käll, M. & Börjesson, L. Spectroscopy of single hemoglobin molecules by surface enhanced raman scattering. *Phys. Rev. Lett.* **83**, 4357–4360 (1999). URL http://link.aps.org/doi/10.1103/PhysRevLett.83.4357.

[55] Stewart, M. E. *et al.* Nanostructured plasmonic sensors. *Chemical Reviews* **108**, 494–521 (2008). URL http://dx.doi.org/10.1021/cr068126n.

[56] Vo-Dinh, T. *et al.* Plasmonic nanoparticles and nanowires: Design, fabrication and application in sensing. *The Journal of Physical Chemistry C* **114**, 7480–7488 (2010). URL http://dx.doi.org/10.1021/jp911355q. http://dx.doi.org/10.1021/jp911355q.

[57] Aubry, A. *et al.* Plasmonic light-harvesting devices over the whole visible spectrum. *Nano Letters* **10**, 2574–2579 (2010). URL http://dx.doi.org/10.1021/nl101235d. http://dx.doi.org/10.1021/nl101235d.

[58] Tame, K. R., M. S. abd McEnery, Ozdemir, S. K., Lee, J., Maier, S. A. & Kim, M. S. Quantum plasmonics. *Nature* **9**, 329–340 (2013). URL http://dx.doi.org/10.1038/nphys2615.

[59] Arielly, R., Ofarim, A., Noy, G. & Selzer, Y. Accurate determination of plasmonic fields in molecular junctions by current rectification at optical frequencies. *Nano Letters* **11**, 2968–2972 (2011). URL http://dx.doi.org/10.1021/nl201517k.

[60] Savage, K. J. *et al.* Revealing the quantum regime in tunnelling plasmonics. *Nature* **491**, 574–577 (2012). URL http://dx.doi.org/10.1038/nature11653.

[61] Scholl, J. A., García-Etxarri, A., Koh, A. L. & Dionne, J. A. Observation of quantum tunneling between two plasmonic nanoparticles. *Nano Letters* **13**, 564–569 (2013).

URL http://dx.doi.org/10.1021/nl304078v.

[62] Tan, S. F. *et al.* Quantum plasmon resonances controlled by molecular tunnel junctions. *Science* **343**, 1496–1499 (2014). URL http://science.sciencemag.org/content/343/6178/1496. http://science.sciencemag.org/content/343/6178/1496.full.pdf.

[63] Zhu, W. & Crozier, K. B. Quantum mechanical limit to plasmonic enhancement as observed by surface-enhanced raman scattering. *Nature Communications* **5** (2014). URL http://dx.doi.org/10.1038/ncomms6228.

[64] Toscano, G. *et al.* Resonance shifts and spill-out effects in self-consistent hydrodynamic nanoplasmonics. *Nature Communications* **6** (2015). URL http://dx.doi.org/10.1038/ncomms8132.

[65] Esteban, R., Borisov, A. G., Nordlander, P. & Aizpurua, J. Bridging quantum and classical plasmonics with a quantum-corrected model. *Nature Communications* **3** (2012). URL http://dx.doi.org/10.1038/ncomms1806.

[66] Atay, T., Song, J.-H. & Nurmikko, A. V. Strongly Interacting Plasmon Nanoparticle Pairs: From Dipole-Dipole Interaction to Conductively Coupled Regime. *Nano Letters* **4**, 1627–1631 (2004). URL http://dx.doi.org/10.1021/nl049215n.

[67] Marhaba, S. *et al.* Surface plasmon resonance of single gold nanodimers near the conductive contact limit. *The Journal of Physical Chemistry C* **113**, 4349–4356 (2009). URL http://dx.doi.org/10.1021/jp810405y.

[68] Pérez-González, O. *et al.* Optical spectroscopy of conductive junctions in plasmonic cavities. *Nano letters* **10**, 3090–3095 (2010). URL http://dx.doi.org/10.1021/nl1017173.

[69] Zuloaga, J., Prodan, E. & Nordlander, P. Quantum description of the plasmon resonances of a nanoparticle dimer. *Nano Letters* **9**, 887–891 (2009). URL http://dx.doi.org/10.1021/nl803811g.

[70] Marinica, D., Kazansky, A., Nordlander, P., Aizpurua, J. & Borisov, A. G. Quantum plasmonics: Nonlinear effects in the field enhancement of a plasmonic nanoparticle dimer. *Nano Letters* **12**, 1333–1339 (2012). URL http://dx.doi.org/10.1021/nl300269c.

[71] Runge, E. & Gross, E. K. U. Density-functional theory for time-dependent systems. *Phys. Rev. Lett.* **52**, 997–1000 (1984). URL http://link.aps.org/doi/10.1103/PhysRevLett.52.997.

[72] Onida, G., Reining, L. & Rubio, A. Electronic excitations: density-functional versus many-body green's-function approaches. *Rev. Mod. Phys.* **74**, 601–659 (2002). URL http://link.aps.org/doi/10.1103/RevModPhys.74.601.

[73] Pitarke, J. M., Silkin, V. M., Chulkov, E. V. & Echenique, P. M. Theory of surface plasmons and surface-plasmon polaritons. *Reports on Progress in Physics* **70**, 1 (2007). URL http://stacks.iop.org/0034-4885/70/i=1/a=R01.

[74] Marques, M. A., Maitra, N. T., Nogueira, F. & (Ed.), A. R. *Fundamentals of Time-Dependent Density Functional Theory* (Springer-Verlag Berlin Heidelberg, 2012).

[75] Zuloaga, J., Prodan, E. & Nordlander, P. Quantum plasmonics: Optical properties and tunability of metallic nanorods. *ACS Nano* **4**, 5269–5276 (2010). URL http://dx.doi.org/10.1021/nn101589n.

[76] Stella, L., Zhang, P., García-Vidal, F. J., Rubio, A. & García-González, P. Performance of nonlocal optics when applied to plasmonic nanostructures. *The Journal of Physical Chemistry C* **117**, 8941–8949 (2013). URL http://dx.doi.org/10.1021/jp401887y.

[77] Teperik, T. V., Nordlander, P., Aizpurua, J. & Borisov, A. G. Robust subnanometric plasmon ruler by rescaling of the nonlocal optical response. *Phys. Rev. Lett.* **110**, 263901 (2013). URL http://link.aps.org/doi/10.1103/PhysRevLett.110.263901.

[78] Teperik, T. V., Nordlander, P., Aizpurua, J. & Borisov, A. G. Quantum effects and nonlocality in strongly coupled plasmonic nanowire dimers. *Opt. Express* **21**, 27306–27325 (2013). URL http://www.opticsexpress.org/abstract.cfm?URI=oe-21-22-27306.

[79] Andersen, K., Jensen, K. L., Mortensen, N. A. & Thygesen, K. S. Visualizing hybridized quantum plasmons in coupled nanowires: From classical to tunneling regime. *Phys. Rev. B* **87**, 235433 (2013). URL https://link.aps.org/doi/10.1103/PhysRevB.87.235433.

[80] Kulkarni, V., Prodan, E. & Nordlander, P. Quantum plasmonics: Optical properties of a nanomatryushka. *Nano Letters* **13**, 5873–5879 (2013). URL http://dx.doi.org/10.1021/nl402662e.

[81] Zhang, H., Kulkarni, V., Prodan, E., Nordlander, P. & Govorov, A. O. Theory of quantum plasmon resonances in doped semiconductor nanocrystals. *The Journal of Physical Chemistry C* **118**, 16035–16042 (2014). URL http://dx.doi.org/10.1021/jp5046035.

[82] McMahon, J. M., Gray, S. K. & Schatz, G. C. Nonlocal optical response of metal nanostructures with arbitrary shape. *Phys. Rev. Lett.* **103**, 097403 (2009). URL https://link.aps.org/doi/10.1103/PhysRevLett.103.097403.

[83] McMahon, J. M., Gray, S. K. & Schatz, G. C. Optical properties of nanowire dimers with a spatially nonlocal dielectric function. *Nano Letters* **10**, 3473–3481 (2010). URL http://dx.doi.org/10.1021/nl101606j. PMID: 20715807.

[84] David, C. & GarcÃa de Abajo, F. J. Spatial nonlocality in the optical response of metal nanoparticles. *The Journal of Physical Chemistry C* **115**, 19470–19475 (2011). URL http://dx.doi.org/10.1021/jp204261u. http://dx.doi.org/10.1021/jp204261u.

[85] Raza, S., Toscano, G., Jauho, A.-P., Wubs, M. & Mortensen, N. A. Unusual resonances in nanoplasmonic structures due to nonlocal response. *Phys. Rev. B* **84**,

121412 (2011). URL http://link.aps.org/doi/10.1103/PhysRevB.84.121412.

[86] Toscano, G., Raza, S., Jauho, A.-P., Mortensen, N. A. & Wubs, M. Modified field enhancement and extinction by plasmonic nanowire dimers due to nonlocal response. *Opt. Express* **20**, 4176–4188 (2012). URL http://www.opticsexpress.org/abstract.cfm?URI=oe-20-4-4176.

[87] Fernández-Domínguez, A. I., Wiener, A., García-Vidal, F. J., Maier, S. A. & Pendry, J. B. Transformation-optics description of nonlocal effects in plasmonic nanostructures. *Phys. Rev. Lett.* **108**, 106802 (2012). URL https://link.aps.org/doi/10.1103/PhysRevLett.108.106802.

[88] Fernández-Domínguez, A. I. *et al.* Transformation-optics insight into nonlocal effects in separated nanowires. *Phys. Rev. B* **86**, 241110 (2012). URL https://link.aps.org/doi/10.1103/PhysRevB.86.241110.

[89] Dong, T., Ma, X. & Mittra, R. Optical response in subnanometer gaps due to nonlocal response and quantum tunneling. *Applied Physics Letters* **101**, 233111 (2012). URL http://dx.doi.org/10.1063/1.4769348.

[90] Christensen, T. *et al.* Nonlocal response of metallic nanospheres probed by light, electrons, and atoms. *ACS Nano* **8**, 1745–1758 (2014). URL http://dx.doi.org/10.1021/nn406153k.

[91] Liebsch, A. Surface-plasmon dispersion and size dependence of mie resonance: Silver versus simple metals. *Phys. Rev. B* **48**, 11317–11328 (1993). URL http://link.aps.org/doi/10.1103/PhysRevB.48.11317.

[92] Weissker, H. C. *et al.* Information on quantum states pervades the visible spectrum of the ubiquitous au144(sr)60 gold nanocluster. *Nature Communications* **5**, 3785 EP – (2014). URL http://dx.doi.org/10.1038/ncomms4785. Article.

[93] (Ed.), J. C. M. *Laser Ablation* (Springer Berlin Heidelberg, 1994).

[94] Bäuerle, D. W. *Laser Processing and Chemistry* (Springer-Verlag Berlin Heidelberg, 1996).

[95] Maine, P., Strickland, D., Bado, P., Pessot, M. & Mourou, G. Generation of ultrahigh peak power pulses by chirped pulse amplification. *IEEE Journal of Quantum Electronics* **24**, 398–403 (1988).

[96] Squier, J., Harter, D., Salin, F. & Mourou, G. 100-fs pulse generation and amplification in ti:al2o3. *Opt. Lett.* **16**, 324–326 (1991). URL `http://ol.osa.org/abstract.cfm?URI=ol-16-5-324`.

[97] Du, D., Liu, X., Korn, G., Squier, J. & Mourou, G. Laser-induced breakdown by impact ionization in sio2 with pulse widths from 7 ns to 150 fs. *Applied Physics Letters* **64**, 3071–3073 (1994). URL `http://dx.doi.org/10.1063/1.111350`.

[98] Stuart, B. C., Feit, M. D., Rubenchik, A. M., Shore, B. W. & Perry, M. D. Laser-induced damage in dielectrics with nanosecond to subpicosecond pulses. *Phys. Rev. Lett.* **74**, 2248–2251 (1995). URL `https://link.aps.org/doi/10.1103/PhysRevLett.74.2248`.

[99] Perry, M. D. *et al.* Ultrashort-pulse laser machining of dielectric materials. *Journal of Applied Physics* **85**, 6803–6810 (1999). URL `http://dx.doi.org/10.1063/1.370197`.

[100] Aumayr, F., Burgdorfer, J., Varga, P. & Winter, H. Sputtering of insulator surfaces by slow highly charged ions: Coulomb explosion or defect-mediated desorption? *Comments on Atomic and Molecular Physics* **34**, 201–220 (1999).

[101] Gamaly, E. G., Rode, A. V. & Luther-Davies, B. Ultrafast ablation with high-pulse-rate lasers. part i: Theoretical considerations. *Journal of Applied Physics* **85**, 4213–4221 (1999). URL `http://dx.doi.org/10.1063/1.370333`.

[102] Rode, A. V., Luther-Davies, B. & Gamaly, E. G. Ultrafast ablation with high-pulse-rate lasers. part ii: Experiments on laser deposition of amorphous carbon films. *Journal of Applied Physics* **85**, 4222–4230 (1999). URL `http://dx.doi.org/10.1063/1.370334`.

[103] Gamaly, E., Rode, A., Tikhonchuk, V. & Luther-Davies, B. Electrostatic mechanism of ablation by femtosecond lasers. *Applied Surface Science* **197-198**, 699 – 704 (2002). URL http://www.sciencedirect.com/science/article/pii/S0169433202003963.

[104] Gamaly, E. G., Rode, A. V., Luther-Davies, B. & Tikhonchuk, V. T. Ablation of solids by femtosecond lasers: Ablation mechanism and ablation thresholds for metals and dielectrics. *Physics of Plasmas* **9**, 949–957 (2002). URL http://dx.doi.org/10.1063/1.1447555.

[105] Choi, T. Y. & Grigoropoulos, C. P. Plasma and ablation dynamics in ultrafast laser processing of crystalline silicon. *Journal of Applied Physics* **92**, 4918–4925 (2002). URL http://dx.doi.org/10.1063/1.1510565.

[106] Fang, R., Vorobyev, A. & Guo, C. Direct visualization of the complete evolution of femtosecond laser-induced surface structural dynamics of metals. *Light: Science & Applications* **6** (2016). URL http://www.nature.com/doifinder/10.1038/lsa.2016.256.

[107] Rethfeld, B., Ivanov, D. S., Garcia, M. E. & Anisimov, S. I. Modelling ultrafast laser ablation. *Journal of Physics D: Applied Physics* **50**, 193001 (2017). URL http://stacks.iop.org/0022-3727/50/i=19/a=193001.

[108] Sokolowski-Tinten, K. *et al.* Transient states of matter during short pulse laser ablation. *Phys. Rev. Lett.* **81**, 224–227 (1998). URL https://link.aps.org/doi/10.1103/PhysRevLett.81.224.

[109] Itina, T., Vidal, F., Delaporte, P. & Sentis, M. Numerical study of ultra-short laser ablation of metals and of laser plume dynamics. *Applied Physics A* **79**, 1089–1092 (2004). URL http://dx.doi.org/10.1007/s00339-004-2647-5.

[110] Köller, L. *et al.* Plasmon-enhanced multi-ionization of small metal clusters in strong femtosecond laser fields. *Physical Review Letters* **82**, 3783–3786 (1999). URL https://link.aps.org/doi/10.1103/PhysRevLett.82.3783.

[111] Stoian, R., Ashkenasi, D., Rosenfeld, A. & Campbell, E. E. B. Coulomb explosion in ultrashort pulsed laser ablation of al_2o_3. *Phys. Rev. B* **62**, 13167–13173 (2000). URL https://link.aps.org/doi/10.1103/PhysRevB.62.13167.

[112] Bulgakova, N., Stoian, R., Rosenfeld, A., Campbell, E. & Hertel, I. Model description of surface charging during ultra-fast pulsed laser ablation of materials. *Applied Physics A* **79** (2004). URL http://link.springer.com/10.1007/s00339-004-2692-0.

[113] Dachraoui, H., Husinsky, W. & Betz, G. Ultra-short laser ablation of metals and semiconductors: evidence of ultra-fast coulomb explosion. *Applied Physics A* **83**, 333–336 (2006). URL http://dx.doi.org/10.1007/s00339-006-3499-y.

[114] Kawashita, Y., Nakatsukasa, T. & Yabana, K. Time-dependent density-functional theory simulation for electron-ion dynamics in molecules under intense laser pulses. *Journal of Physics: Condensed Matter* **21**, 064222 (2009). URL http://stacks.iop.org/0953-8984/21/i=6/a=064222.

[115] Taguchi, K., Haruyama, J. & Watanabe, K. Laser-driven molecular dissociation: Time-dependent density functional theory and molecular dynamics simulations. *Journal of the Physical Society of Japan* **78**, 094707 (2009). URL http://journals.jps.jp/doi/10.1143/JPSJ.78.094707.

[116] Bubin, S. & Varga, K. Electron and ion dynamics in graphene and graphane fragments subjected to high-intensity laser pulses. *Physical Review B* **85**, 205441 (2012). URL http://journals.aps.org/prb/abstract/10.1103/PhysRevB.85.205441.

[117] Bubin, S. & Varga, K. Electron-ion dynamics in laser-assisted desorption of hydrogen atoms from h-si(111) surface. *Journal of Applied Physics* **110**, 064905 (2011). URL http://scitation.aip.org/content/aip/journal/jap/110/6/10.1063/1.3638064.

[118] Bubin, S., Russakoff, A. G. & Varga, K. Interaction of electromagnetic fields and atomic clusters. *Journal of Physics: Conference Series* **436**, 012084 (2013). URL

http://iopscience.iop.org/article/10.1088/1742-6596/436/1/012084.

[119] Debnarova, A., Techert, S. & Schmatz, S. Contribution of coulomb explosion to form factors and mosaicity spread in single particle x-ray scattering. *Phys. Chem. Chem. Phys.* **16**, 792–798 (2014). URL http://dx.doi.org/10.1039/C3CP54011A.

[120] Pelton, M., Aizpurua, J. & Bryant, G. Metal-nanoparticle plasmonics. *Laser & Photonics Reviews* **2**, 136–159 (2008). URL http://dx.doi.org/10.1002/lpor.200810003.

[121] Pelton Matthew, B. G. W. *Introduction to Metal-Nanoparticle Plasmonics* (Wiley, 2013).

[122] Moskovits, M. Surface-enhanced spectroscopy. *Rev. Mod. Phys.* **57**, 783–826 (1985). URL http://link.aps.org/doi/10.1103/RevModPhys.57.783.

[123] Yang, W.-H., Schatz, G. C. & Duyne, R. P. V. Discrete dipole approximation for calculating extinction and raman intensities for small particles with arbitrary shapes. *The Journal of Chemical Physics* **103**, 869–875 (1995). URL http://dx.doi.org/10.1063/1.469787.

[124] Taflove, A. & Hagness, S. C. *Computational Electrodynamics: The Finite-Difference Time-Domain Method* (Artech House, Incorporated, 2005).

[125] García de Abajo, F. J. Nonlocal effects in the plasmons of strongly interacting nanoparticles, dimers, and waveguides. *The Journal of Physical Chemistry C* **112**, 17983–17987 (2008). URL http://dx.doi.org/10.1021/jp807345h.

[126] Fernández-Domínguez, A. I., Wiener, A., García-Vidal, F. J., Maier, S. A. & Pendry, J. B. Transformation-optics description of nonlocal effects in plasmonic nanostructures. *Phys. Rev. Lett.* **108**, 106802 (2012). URL http://link.aps.org/doi/10.1103/PhysRevLett.108.106802.

[127] Wiener, A., Fernández-Domínguez, A. I., Horsfield, A. P., Pendry, J. B. & Maier, S. A. Nonlocal effects in the nanofocusing performance of plasmonic tips. *Nano Letters* **12**, 3308–3314 (2012). URL http://dx.doi.org/10.1021/nl301478n.

[128] Boardman, A. D. *Electromagnetic Surface Modes* (John Wiley & Sons Ltd, 1982).

[129] Raza, S., Bozhevolnyi, S. I., Wubs, M. & Mortensen, N. A. Nonlocal optical response in metallic nanostructures. *Journal of Physics: Condensed Matter* **27**, 183204 (2015). URL http://stacks.iop.org/0953-8984/27/i=18/a=183204.

[130] Luo, Y., Fernández-Domínguez, A. I., Wiener, A., Maier, S. A. & Pendry, J. B. Surface plasmons and nonlocality: A simple model. *Phys. Rev. Lett.* **111**, 093901 (2013). URL http://link.aps.org/doi/10.1103/PhysRevLett.111.093901.

[131] Cha, H., Yoon, J. H. & Yoon, S. Probing quantum plasmon coupling using gold nanoparticle dimers with tunable interparticle distances down to the subnanometer range. *ACS Nano* **8**, 8554–8563 (2014). URL http://dx.doi.org/10.1021/nn5032438.

[132] Kravtsov, V., Berweger, S., Atkin, J. M. & Raschke, M. B. Control of plasmon emission and dynamics at the transition from classical to quantum coupling. *Nano Letters* **14**, 5270–5275 (2014). URL http://dx.doi.org/10.1021/nl502297t.

[133] Hajisalem, G., Nezami, M. S. & Gordon, R. Probing the quantum tunneling limit of plasmonic enhancement by third harmonic generation. *Nano Letters* **14**, 6651–6654 (2014). URL http://dx.doi.org/10.1021/nl503324g.

[134] Tonks, L. & Langmuir, I. Oscillations in ionized gases. *Phys. Rev.* **33**, 195–210 (1929). URL http://link.aps.org/doi/10.1103/PhysRev.33.195.

[135] Jackson, J. D. *Classical Electrodynamics* (John Wiley & Sons Ltd., 1999).

[136] Noguez, C. Surface plasmons on metal nanoparticles: The influence of shape and physical environment. *The Journal of Physical Chemistry C* **111**, 3806–3819 (2007). URL http://dx.doi.org/10.1021/jp066539m.

[137] López-Lozano, X., Barron, H., Mottet, C. & Weissker, H.-C. Aspect-ratio- and size-dependent emergence of the surface-plasmon resonance in gold nanorods - an ab initio tddft study. *Phys. Chem. Chem. Phys.* **16**, 1820–1823 (2014). URL http://dx.doi.org/10.1039/C3CP53702A.

[138] Purcell, E. M. & Pennypacker, C. R. Scattering and absorption of light by non-spherical dielectric grains. *The Astrophysical Journal* **186**, 705–714 (1973).

[139] Draine, B. T. The discrete-dipole approximation and its application to interstellar graphite grains. *The Astrophysical Journal* **333**, 848 (1988).

[140] Singham, S. B. & Salzman, G. C. Evaluation of the scattering matrix of an arbitrary particle using the coupled dipole approximation. *The Journal of Chemical Physics* **84**, 2658–2667 (1986). URL http://dx.doi.org/10.1063/1.450338.

[141] Singham, S. B. & Bohren, C. F. Light scattering by an arbitrary particle: a physical reformulation of the coupled dipole method. *Opt. Lett.* **12**, 10–12 (1987). URL http://ol.osa.org/abstract.cfm?URI=ol-12-1-10.

[142] Varas, A., García-González, P., Feist, J., García-Vidal, F. & Rubio, A. Quantum plasmonics: from jellium models to ab initio calculations. *Nanophotonics* **5**, 409–426 (2016). URL http://www.degruyter.com/view/j/nanoph.2016.5.issue-3/nanoph-2015-0141/nanoph-2015-0141.xml.

[143] Lundqvist, S. & (Ed.), N. H. M. *Theory of the Inhomogeneous Electron Gas* (Springer US, 1983). URL http://dx.doi.org/10.1007/978-1-4899-0415-7.

[144] Eguiluz, A. & Quinn, J. Influence of the electron density profile on surface plasmons: Retardation effects. *Physics Letters A* **53**, 151–153 (1975). URL http://www.sciencedirect.com/science/article/pii/0375960175905083.

[145] Domps, A., Reinhard, P.-G. & Suraud, E. Time-dependent thomas-fermi approach for electron dynamics in metal clusters. *Phys. Rev. Lett.* **80**, 5520–5523 (1998). URL http://link.aps.org/doi/10.1103/PhysRevLett.80.5520.

[146] Banerjee, A. & Harbola, M. K. Hydrodynamic approach to time-dependent density functional theory; response properties of metal clusters. *The Journal of Chemical Physics* **113**, 5614–5623 (2000). URL http://dx.doi.org/10.1063/1.1290610. http://dx.doi.org/10.1063/1.1290610.

[147] Zaremba, E. & Tso, H. C. Thomas-fermi-dirac-von weizsäcker hydrodynamics in parabolic wells. *Phys. Rev. B* **49**, 8147–8162 (1994). URL http://link.aps.org/doi/10.1103/PhysRevB.49.8147.

[148] Crouseilles, N., Hervieux, P.-A. & Manfredi, G. Quantum hydrodynamic model for the nonlinear electron dynamics in thin metal films. *Phys. Rev. B* **78**, 155412 (2008). URL http://link.aps.org/doi/10.1103/PhysRevB.78.155412.

[149] Pines, D. *Elementary Excitations In Solids: Lectures On Phonons, Electrons, And Plasmons* (Westview Press, 1999).

[150] Liebsch, A. *Electronic Excitations at Metal Surfaces* (Springer US, 1997).

[151] Bernadotte, S., Evers, F. & Jacob, C. R. Plasmons in molecules. *The Journal of Physical Chemistry C* **117**, 1863–1878 (2013). URL http://dx.doi.org/10.1021/jp3113073. http://dx.doi.org/10.1021/jp3113073.

[152] Townsend, E. & Bryant, G. W. Which resonances in small metallic nanoparticles are plasmonic? *Journal of Optics* **16**, 114022 (2014). URL http://stacks.iop.org/2040-8986/16/i=11/a=114022.

[153] Krauter, C. M., Schirmer, J., Jacob, C. R., Pernpointner, M. & Dreuw, A. Plasmons in molecules: Microscopic characterization based on orbital transitions and momentum conservation. *The Journal of Chemical Physics* **141**, 104101 (2014). URL http://dx.doi.org/10.1063/1.4894266. http://dx.doi.org/10.1063/1.4894266.

[154] Guidez, E. B. & Aikens, C. M. Plasmon resonance analysis with configuration interaction. *Phys. Chem. Chem. Phys.* **16**, 15501–15509 (2014). URL http://dx.doi.org/10.1039/C4CP01365D.

[155] Jain, P. K. Plasmon-in-a-box: On the physical nature of few-carrier plasmon resonances. *The Journal of Physical Chemistry Letters* **5**, 3112–3119 (2014). URL http://dx.doi.org/10.1021/jz501456t.

[156] Fiolhais, C., Nogueira, F. & (Ed.), M. A. L. M. *A Primer in Density Functional Theory* (Springer-Verlag Berlin Heidelberg, 2003).

[157] Marques, M. A. *et al. Time-Dependent Density Functional Theory* (Springer-Verlag Berlin Heidelberg, 2006).

[158] Ullrich, C. A. *Time-Dependent Density-Functional Theory: Concepts and Applications* (Oxford Graduate Texts, 2011).

[159] Hohenberg, P. & Kohn, W. Inhomogeneous electron gas. *Phys. Rev.* **136**, B864–B871 (1964). URL http://link.aps.org/doi/10.1103/PhysRev.136.B864.

[160] Kohn, W. & Sham, L. J. Self-consistent equations including exchange and correlation effects. *Phys. Rev.* **140**, A1133–A1138 (1965). URL http://link.aps.org/doi/10.1103/PhysRev.140.A1133.

[161] Fetter, A. L. & Walecka, J. D. *Quantum Theory of Many-Particle Systems* (McGraw Hill, 1971).

[162] Petersilka, M., Gossmann, U. J. & Gross, E. K. U. Excitation energies from time-dependent density-functional theory. *Phys. Rev. Lett.* **76**, 1212–1215 (1996). URL http://link.aps.org/doi/10.1103/PhysRevLett.76.1212.

[163] Casida, M. E. *Time-Dependent Density Functional Response Theory for Molecules* (1995).

[164] Grabo, T., Petersilka, M. & Gross, E. K. U. Molecular excitation energies from time-dependent density functional theory. *Journal of Molecular Structure: {THEOCHEM}* **501-502**, 353–367 (2000). URL http://www.sciencedirect.com/science/article/pii/S0166128099004455.

[165] Zangwill, A. & Soven, P. Density-functional approach to local-field effects in finite systems: Photoabsorption in the rare gases. *Phys. Rev. A* **21**, 1561–1572 (1980). URL http://link.aps.org/doi/10.1103/PhysRevA.21.1561.

[166] Ekardt, W. Dynamical polarizability of small metal particles: Self-consistent spherical jellium background model. *Phys. Rev. Lett.* **52**, 1925–1928 (1984). URL http://link.aps.org/doi/10.1103/PhysRevLett.52.1925.

[167] Puska, M. J., Nieminen, R. M. & Manninen, M. Electronic polarizability of small metal spheres. *Phys. Rev. B* **31**, 3486–3495 (1985). URL http://link.aps.org/doi/10.1103/PhysRevB.31.3486.

[168] Ekardt, W. Size-dependent photoabsorption and photoemission of small metal particles. *Phys. Rev. B* **31**, 6360–6370 (1985). URL http://link.aps.org/doi/10.1103/PhysRevB.31.6360.

[169] Ekardt, W. Collective multipole excitations in small metal particles: Critical angular momentum l^{cr} for the existence of collective surface modes. *Phys. Rev. B* **32**, 1961–1970 (1985). URL http://link.aps.org/doi/10.1103/PhysRevB.32.1961.

[170] Beck, D. E. Self-consistent calculation of the eigenfrequencies for the electronic excitations in small jellium spheres. *Phys. Rev. B* **35**, 7325–7333 (1987). URL http://link.aps.org/doi/10.1103/PhysRevB.35.7325.

[171] de Heer, W. A. The physics of simple metal clusters: experimental aspects and simple models. *Rev. Mod. Phys.* **65**, 611–676 (1993). URL http://link.aps.org/doi/10.1103/RevModPhys.65.611.

[172] Brack, M. The physics of simple metal clusters: self-consistent jellium model and semiclassical approaches. *Rev. Mod. Phys.* **65**, 677–732 (1993). URL http://link.aps.org/doi/10.1103/RevModPhys.65.677.

[173] Tiggesbäumker, J., Köller, L., Meiwes-Broer, K.-H. & Liebsch, A. Blue shift of the mie plasma frequency in ag clusters and particles. *Phys. Rev. A* **48**, R1749–R1752 (1993). URL http://link.aps.org/doi/10.1103/PhysRevA.48.R1749.

[174] Serra, L. m. c. & Rubio, A. Core polarization in the optical response of metal clusters: Generalized time-dependent density-functional theory. *Phys. Rev. Lett.* **78**, 1428–1431 (1997). URL http://link.aps.org/doi/10.1103/PhysRevLett.78.1428.

[175] Lermé, J. *et al.* Quenching of the size effects in free and matrix-embedded silver clusters. *Phys. Rev. Lett.* **80**, 5105–5108 (1998). URL http://link.aps.org/doi/

10.1103/PhysRevLett.80.5105.

[176] Zhang, H., Kulkarni, V., Prodan, E., Nordlander, P. & Govorov, A. O. Theory of quantum plasmon resonances in doped semiconductor nanocrystals. *The Journal of Physical Chemistry C* **118**, 16035–16042 (2014). URL http://dx.doi.org/10.1021/jp5046035.

[177] Prodan, E. & Nordlander, P. Electronic structure and polarizability of metallic nanoshells. *Chemical Physics Letters* **352**, 140–146 (2002). URL http://www.sciencedirect.com/science/article/pii/S0009261401014099.

[178] Prodan, E. & Nordlander, P. Structural tunability of the plasmon resonances in metallic nanoshells. *Nano Letters* **3**, 543–547 (2003). URL http://dx.doi.org/10.1021/nl034030m.

[179] Prodan, E., Nordlander, P. & Halas, N. J. Electronic structure and optical properties of gold nanoshells. *Nano Letters* **3**, 1411–1415 (2003). URL http://dx.doi.org/10.1021/nl034594q.

[180] Cottancin, E. *et al.* Optical properties of noble metal clusters as a function of the size: Comparison between experiments and a semi-quantal theory. *Theoretical Chemistry Accounts* **116**, 514–523 (2006). URL http://dx.doi.org/10.1007/s00214-006-0089-1.

[181] Lermé, J. *et al.* Size dependence of the surface plasmon resonance damping in metal nanospheres. *The Journal of Physical Chemistry Letters* **1**, 2922–2928 (2010). URL http://dx.doi.org/10.1021/jz1009136.

[182] Lermé, J. Size evolution of the surface plasmon resonance damping in silver nanoparticles: Confinement and dielectric effects. *The Journal of Physical Chemistry C* **115**, 14098–14110 (2011). URL http://dx.doi.org/10.1021/jp203481m.

[183] Andrade, X., Botti, S., Marques, M. A. L. & Rubio, A. Time-dependent density functional theory scheme for efficient calculations of dynamic (hyper)polarizabilities.

The Journal of Chemical Physics **126**, 184106 (2007). URL http://dx.doi.org/10.1063/1.2733666.

[184] Yabana, K. & Bertsch, G. F. Time-dependent local-density approximation in real time. *Phys. Rev. B* **54**, 4484–4487 (1996). URL http://link.aps.org/doi/10.1103/PhysRevB.54.4484.

[185] Marques, M. A. L., Castro, A., Bertsch, G. F. & Rubio, A. octopus: a first-principles tool for excited electron-ion dynamics. *Computer Physics Communications* **151**, 60–78 (2003). URL http://www.sciencedirect.com/science/article/pii/S0010465502006860.

[186] Castro, A. *et al.* octopus: a tool for the application of time-dependent density functional theory. *physica status solidi (b)* **243**, 2465–2488 (2006). URL http://dx.doi.org/10.1002/pssb.200642067.

[187] Andrade, X. *et al.* Time-dependent density-functional theory in massively parallel computer architectures: the octopus project. *Journal of physics. Condensed matter : an Institute of Physics journal* **24**, 233202 (2012). URL http://iopscience.iop.org/article/10.1088/0953-8984/24/23/233202.

[188] Andrade, X. *et al.* Real-space grids and the octopus code as tools for the development of new simulation approaches for electronic systems. *Phys. Chem. Chem. Phys.* **17**, 31371–31396 (2015). URL http://dx.doi.org/10.1039/C5CP00351B.

[189] Andrade, X. *Linear and non-linear response phenomena of molecular systems within time-dependent density functional theory.* Ph.D. thesis, University of the Basque Country - UPV/EHU (2010).

[190] Tafipolsky, M. & Schmid, R. A general and efficient pseudopotential fourier filtering scheme for real space methods using mask functions. *The Journal of Chemical Physics* **124**, 174102 (2006). URL http://dx.doi.org/10.1063/1.2193514.

[191] Hirose, K. *First-Principles Calculations in Real-Space Formalism* (2005).

[192] Bitzek, E., Koskinen, P., Gähler, F., Moseler, M. & Gumbsch, P. Structural relaxation made simple. *Phys. Rev. Lett.* **97**, 170201 (2006). URL http://link.aps.org/doi/10.1103/PhysRevLett.97.170201.

[193] Asenjo, D., Stevenson, J. D., Wales, D. J. & Frenkel, D. Visualizing basins of attraction for different minimization algorithms. *The Journal of Physical Chemistry B* **117**, 12717–12723 (2013). URL http://dx.doi.org/10.1021/jp312457a.

[194] Musazzi, S. & Perini, U. E. *Laser-Induced Breakdown Spectroscopy*, vol. 182 of *Springer Series in Optical Sciences* (Springer Berlin Heidelberg, Berlin, Heidelberg, 2014). URL http://link.springer.com/10.1007/978-3-642-45085-3.

[195] Jiang, L. & Tsai, H.-L. A plasma model combined with an improved two-temperature equation for ultrafast laser ablation of dielectrics. *Journal of Applied Physics* **104**, 093101 (2008). URL http://dx.doi.org/10.1063/1.3006129.

[196] Troullier, N. & Martins, J. L. Efficient pseudopotentials for plane-wave calculations. *Phys. Rev. B* **43**, 1993–2006 (1991). URL http://link.aps.org/doi/10.1103/PhysRevB.43.1993.

[197] Perdew, J. P. & Zunger, A. Self-interaction correction to density-functional approximations for many-electron systems. *Phys. Rev. B* **23**, 5048–5079 (1981). URL http://link.aps.org/doi/10.1103/PhysRevB.23.

[198] Beckmann, H.-O., Koutecký, J. & Bonačić-Koutecký, V. Electronic and geometric structure of Li_4 and Na_4 clusters. *The Journal of Chemical Physics* **73**, 5182–5190 (1980). URL http://scitation.aip.org/content/aip/journal/jcp/73/10/10.1063/1.439945.

[199] Monari, A., Pitarch-Ruiz, J., Bendazzoli, G. L., Evangelisti, S. & Sanchez-Marin, J. Full configuration-interaction study on the tetrahedral li4 cluster. *Journal of Chemical Theory and Computation* **4**, 404–413 (2008). URL http://dx.doi.org/10.1021/ct7003319.

[200] Castro, A., Isla, M., Martínez, J. I. & Alonso, J. A. Scattering of a proton with the li4 cluster: Non-adiabatic molecular dynamics description based on time-dependent density-functional theory. *Chemical Physics* **399**, 130–134 (2012). URL http://www.sciencedirect.com/science/article/pii/S0301010411002850.

[201] Draine, B. T. & Flatau, P. J. Discrete-dipole approximation for scattering calculations. *J. Opt. Soc. Am. A* **11**, 1491–1499 (1994). URL http://josaa.osa.org/abstract.cfm?URI=josaa-11-4-1491.

[202] Yurkin, M. A. & Hoekstra, A. G. The discrete-dipole-approximation code adda: Capabilities and known limitations. *Journal of Quantitative Spectroscopy and Radiative Transfer* **112**, 2234–2247 (2011). URL http://www.sciencedirect.com/science/article/pii/S0022407311000562. Polarimetric Detection, Characterization, and Remote Sensing.

[203] Jain, P. K. Plasmon-in-a-box: On the physical nature of few-carrier plasmon resonances. *The Journal of Physical Chemistry Letters* **5**, 3112–3119 (2014). URL http://dx.doi.org/10.1021/jz501456t.

[204] Scholl, J. A., Koh, A. L. & Dionne, J. A. Quantum plasmon resonances of individual metallic nanoparticles. *Nature* **483**, 421–427 (2012).

[205] Nozaki, H., Shibata, K. & Ohhash, N. Metallic hole conduction in cus. *Journal of Solid State Chemistry* **91**, 306–311 (1991). URL http://www.sciencedirect.com/science/article/pii/002245969190085V.

[206] Liang, W. & Whangbo, M.-H. Conductivity anisotropy and structural phase transition in covellite cus. *Solid State Communications* **85**, 405–408 (1993). URL http://www.sciencedirect.com/science/article/pii/003810989390689K.

[207] Pearce, C. I. Electrical and Magnetic Properties of Sulfides. *Reviews in Mineralogy and Geochemistry* **61**, 127–180 (2006). URL http://rimg.geoscienceworld.org/content/61/1/127.extract.

[208] Yuan, K. D. *et al.* Fabrication and microstructure of p-type transparent conducting cus thin film and its application in dye-sensitized solar cell. *Applied Physics Letters* **93**, 132106 (2008). URL http://dx.doi.org/10.1063/1.2991441.

[209] Adelifard, M., Eshghi, H. & Mohagheghi, M. M. B. An investigation on substrate temperature and copper to sulphur molar ratios on optical and electrical properties of nanostructural cus thin films prepared by spray pyrolysis method. *Applied Surface Science* **258**, 5733–5738 (2012). URL http://www.sciencedirect.com/science/article/pii/S0169433212003248.

[210] Mazin, I. I. Structural and electronic properties of the two-dimensional superconductor cus with $1\frac{1}{3}$-valent copper. *Phys. Rev. B* **85**, 115133 (2012). URL http://link.aps.org/doi/10.1103/PhysRevB.85.115133.

[211] Lounis, S. D., Runnerstrom, E. L., LlordÃ©s, A. & Milliron, D. J. Defect chemistry and plasmon physics of colloidal metal oxide nanocrystals. *The Journal of Physical Chemistry Letters* **5**, 1564–1574 (2014). URL http://dx.doi.org/10.1021/jz500440e. PMID: 26270097, http://dx.doi.org/10.1021/jz500440e.

[212] Kriegel, I. *et al.* Tuning the excitonic and plasmonic properties of copper chalcogenide nanocrystals. *Journal of the American Chemical Society* **134**, 1583–1590 (2012). URL http://dx.doi.org/10.1021/ja207798q. PMID: 22148506.

[213] Palomaki, P. K. B., Miller, E. M. & Neale, N. R. Control of plasmonic and interband transitions in colloidal indium nitride nanocrystals. *Journal of the American Chemical Society* **135**, 14142–14150 (2013). URL http://dx.doi.org/10.1021/ja404599g. PMID: 23972038, http://dx.doi.org/10.1021/ja404599g.

[214] Liu, M. *et al.* Room-temperature synthesis of covellite nanoplatelets with broadly tunable localized surface plasmon resonance. *Chemistry of Materials* **27**, 2584–2590 (2015). URL http://dx.doi.org/10.1021/acs.chemmater.5b00270. http://dx.doi.org/10.1021/acs.chemmater.5b00270.

[215] Agrawal, A., Kriegel, I. & Milliron, D. J. Shape-dependent field enhancement and

plasmon resonance of oxide nanocrystals. *The Journal of Physical Chemistry C* **119**, 6227–6238 (2015). URL http://dx.doi.org/10.1021/acs.jpcc.5b01648. http://dx.doi.org/10.1021/acs.jpcc.5b01648.

[216] Gordon, T. R. *et al.* Shape-dependent plasmonic response and directed self-assembly in a new semiconductor building block, indium-doped cadmium oxide (ico). *Nano Letters* **13**, 2857–2863 (2013). URL http://dx.doi.org/10.1021/nl4012003. PMID: 23701224, http://dx.doi.org/10.1021/nl4012003.

[217] Dietz, R. E., Campagna, M., Chazalviel, J. N. & Shanks, H. R. Inelastic electron scattering by intra- and interband plasmons in rhenium trioxide, tungsten trioxide, and some tungsten bronzes. *Phys. Rev. B* **17**, 3790–3800 (1978). URL https://link.aps.org/doi/10.1103/PhysRevB.17.3790.

[218] Bange, K. Colouration of tungsten oxide films: A model for optically active coatings. *Solar Energy Materials and Solar Cells* **58**, 1–131 (1999). URL http://www.sciencedirect.com/science/article/pii/S0927024898001962.

[219] Deb, S. K. Opportunities and challenges in science and technology of {WO3} for electrochromic and related applications. *Solar Energy Materials and Solar Cells* **92**, 245–258 (2008). URL http://www.sciencedirect.com/science/article/pii/S0927024807003303. Selected Papers from the Seventh International Meeting on Electrochromism (IME-7)Seventh International Meeting on Electrochromism.

[220] Ingham, B., Hendy, S. C., Chong, S. V. & Tallon, J. L. Density-functional studies of tungsten trioxide, tungsten bronzes, and related systems. *Phys. Rev. B* **72**, 075109 (2005). URL https://link.aps.org/doi/10.1103/PhysRevB.72.075109.

[221] Wang, F., Di Valentin, C. & Pacchioni, G. Electronic and structural properties of wo3: A systematic hybrid dft study. *The Journal of Physical Chemistry C* **115**, 8345–8353 (2011). URL http://dx.doi.org/10.1021/jp201057m. http://dx.doi.org/10.1021/jp201057m.

[222] Ping, Y., Rocca, D. & Galli, G. Optical properties of tungsten trioxide from first-

principles calculations. *Phys. Rev. B* **87**, 165203 (2013). URL https://link.aps.org/doi/10.1103/PhysRevB.87.165203.

[223] Granqvist, C. G. (ed.) *Handbook of Inorganic Electrochromic Materials* (Elsevier Science B.V., Amsterdam, 1995). URL http://www.sciencedirect.com/science/book/9780444899309.

[224] Gillet, M., Lemire, C., Gillet, E. & Aguir, K. The role of surface oxygen vacancies upon {WO3} conductivity. *Surface Science* **532-535**, 519 – 525 (2003). URL http://www.sciencedirect.com/science/article/pii/S0039602803004771. Proceedings of the 7th International Conference on Nanometer-Scale Science and Technology and the 21st European Conference on Surface Science.

[225] Migas, D. B., Shaposhnikov, V. L., Rodin, V. N. & Borisenko, V. E. Tungsten oxides. i. effects of oxygen vacancies and doping on electronic and optical properties of different phases of wo3. *Journal of Applied Physics* **108**, 093713 (2010). URL http://dx.doi.org/10.1063/1.3505688.

[226] Migas, D. B., Shaposhnikov, V. L. & Borisenko, V. E. Tungsten oxides. ii. the metallic nature of magnÃ©li phases. *Journal of Applied Physics* **108**, 093714 (2010). URL http://dx.doi.org/10.1063/1.3505689.

[227] Wang, F., Di Valentin, C. & Pacchioni, G. Semiconductor-to-metal transition in wo_{3-x}: Nature of the oxygen vacancy. *Phys. Rev. B* **84**, 073103 (2011). URL https://link.aps.org/doi/10.1103/PhysRevB.84.073103.

[228] Gerosa, M. *et al.* Defect calculations in semiconductors through a dielectric-dependent hybrid dft functional: The case of oxygen vacancies in metal oxides. *The Journal of Chemical Physics* **143**, 134702 (2015). URL http://aip.scitation.org/doi/abs/10.1063/1.4931805.

[229] Yan, J. *et al.* Tungsten oxide single crystal nanosheets for enhanced multichannel solar light harvesting. *Advanced Materials* **27**, 1580–1586 (2015). URL http://dx.doi.org/10.1002/adma.201404792.

[230] Kim, J., Agrawal, A., Krieg, F., Bergerud, A. & Milliron, D. J. The interplay of shape and crystalline anisotropies in plasmonic semiconductor nanocrystals. *Nano Letters* **16**, 3879–3884 (2016). URL http://dx.doi.org/10.1021/acs.nanolett.6b01390.

[231] Johns, R. W. *et al.* Direct observation of narrow mid-infrared plasmon linewidths of single metal oxide nanocrystals. *Nature Communications* **7**, 11583 (2016). URL http://dx.doi.org/10.1038/ncomms11583.

[232] Monreal, R. C., Antosiewicz, T. J. & Apell, S. P. Competition between surface screening and size quantization for surface plasmons in nanoparticles. *New Journal of Physics* **15**, 083044 (2013). URL http://stacks.iop.org/1367-2630/15/i=8/a=083044.

[233] Varas, A., García-González, P., García-Vidal, F. J. & Rubio, A. Anisotropy Effects on the Plasmonic Response of Nanoparticle Dimers. *The Journal of Physical Chemistry Letters* **6**, 1891–1898 (2015). URL http://dx.doi.org/10.1021/acs.jpclett.5b00573.

[234] Zhang, P., Feist, J., Rubio, A., García-González, P. & García-Vidal, F. J. Ab initio nanoplasmonics: The impact of atomic structure. *Physical Review B* **90**, 161407 (2014). URL http://link.aps.org/doi/10.1103/PhysRevB.90.161407.

[235] Noya, E. G., Doye, J. P., Wales, D. J. & Aguado, A. Geometric magic numbers of sodium clusters: Interpretation of the melting behaviour. *The European Physical Journal D* **43**, 57–60 (2007). URL http://www.springerlink.com/index/10.1140/epjd/e2007-00092-x.

[236] Nordlander, P., Oubre, C., Prodan, E., Li, K. & Stockman, M. I. Plasmon hybridization in nanoparticle dimers. *Nano Letters* **4**, 899–903 (2004). URL http://dx.doi.org/10.1021/nl049681c.

[237] Romero, I., Aizpurua, J., Bryant, G. W. & de Abajo, F. J. G. Plasmons in nearly touching metallic nanoparticles: singular response in the limit of touching

dimers. *Opt. Express* **14**, 9988–9999 (2006). URL http://www.opticsexpress.org/abstract.cfm?URI=oe-14-21-9988.

[238] Luo, Y., Lei, D. Y., Maier, S. A. & Pendry, J. B. Transformation-optics description of plasmonic nanostructures containing blunt edges/corners: From symmetric to asymmetric edge rounding. *ACS Nano* **6**, 6492–6506 (2012). URL http://dx.doi.org/10.1021/nn3022684.

[239] Lei, D. Y., Aubry, A., Luo, Y., Maier, S. A. & Pendry, J. B. Plasmonic interaction between overlapping nanowires. *ACS Nano* **5**, 597–607 (2011). URL http://dx.doi.org/10.1021/nn102819p.

[240] Townsend, E. & Bryant, G. W. Plasmonic properties of metallic nanoparticles: The effects of size quantization. *Nano Letters* **12**, 429–434 (2012). URL http://dx.doi.org/10.1021/nl2037613.

[241] Yannouleas, C., Vigezzi, E. & Broglia, R. A. Evolution of the optical properties of alkali-metal microclusters towards the bulk: The matrix random-phase-approximation description. *Phys. Rev. B* **47**, 9849–9861 (1993). URL http://link.aps.org/doi/10.1103/PhysRevB.47.9849.

[242] Li, J.-H., Hayashi, M. & Guo, G.-Y. Plasmonic excitations in quantum-sized sodium nanoparticles studied by time-dependent density functional calculations. *Phys. Rev. B* **88**, 155437 (2013). URL https://link.aps.org/doi/10.1103/PhysRevB.88.155437.

[243] Xiang, H., Zhang, X., Neuhauser, D. & Lu, G. Size-dependent plasmonic resonances from large-scale quantum simulations. *The Journal of Physical Chemistry Letters* **5**, 1163–1169 (2014). URL http://dx.doi.org/10.1021/jz500216t.

[244] Aradhya, S. V. & Venkataraman, L. Single-molecule junctions beyond electronic transport. *Nature nanotechnology* **8**, 399–410 (2013). URL http://www.nature.com/nnano/journal/v8/n6/full/nnano.2013.91.html?WT.ec{_}id=NNANO-201306.

[245] Benz, F. *et al.* Nanooptics of molecular-shunted plasmonic nanojunctions. *Nano letters* **15**, 669–674 (2015). URL http://dx.doi.org/10.1021/nl5041786.

[246] Moore, G. E. Cramming more components onto integrated circuits. *Electronics* **86**, 114–117 (1965).

[247] Thompson, R. J., Rempe, G. & Kimble, H. J. Observation of normal-mode splitting for an atom in an optical cavity. *Phys. Rev. Lett.* **68**, 1132–1135 (1992). URL http://link.aps.org/doi/10.1103/PhysRevLett.68.1132.

[248] Vahala, K. J. Optical microcavities. *Nature* **424**, 839–846 (2003). URL http://www.nature.com/doifinder/10.1038/nature01939.

[249] O'Shea, D., Junge, C., Volz, J. & Rauschenbeutel, A. Fiber-optical switch controlled by a single atom. *Phys. Rev. Lett.* **111**, 193601 (2013). URL http://link.aps.org/doi/10.1103/PhysRevLett.111.193601.

[250] Chen, W. *et al.* All-optical switch and transistor gated by one stored photon. *Science (New York, N.Y.)* **341**, 768–770 (2013). URL http://www.ncbi.nlm.nih.gov/pubmed/23828886.

[251] Emboras, A. *et al.* Atomic Scale Plasmonic Switch. *Nano Letters* **16**, 709–714 (2016). URL http://pubs.acs.org/doi/abs/10.1021/acs.nanolett.5b04537.

[252] Song, P., Nordlander, P. & Gao, S. Quantum mechanical study of the coupling of plasmon excitations to atomic-scale electron transport. *The Journal of chemical physics* **134**, 074701 (2011). URL http://scitation.aip.org/content/aip/journal/jcp/134/7/10.1063/1.3554420.

[253] Kulkarni, V. & Manjavacas, A. Quantum Effects in Charge Transfer Plasmons. *ACS Photonics* **2**, 987–992 (2015). URL http://dx.doi.org/10.1021/acsphotonics.5b00246.

[254] Barbry, M. *et al.* Atomistic Near-Field Nanoplasmonics: Reaching Atomic-Scale Resolution in Nanooptics. *Nano letters* (2015). URL http://dx.doi.org/10.1021/acs.nanolett.5b00759.

[255] Rossi, T. P., Zugarramurdi, A., Puska, M. J. & Nieminen, R. M. Quantized Evolution of the Plasmonic Response in a Stretched Nanorod. *Physical Review Letters* **115**, 236804 (2015). URL http://link.aps.org/doi/10.1103/PhysRevLett.115.236804.